

UNIVERSITÁ DEGLI STUDI DI PADOVA

ANNALISA TRESOLDI

CFD Modeling and Analysis of a Boundary Layer Ingesting S-shaped Intake

DIPARTIMENTO DI INGEGNERIA INDUSTRIALE

MSC IN AEROSPACE ENGINEERING

MSC THESIS

Academic Year: 2018-2019

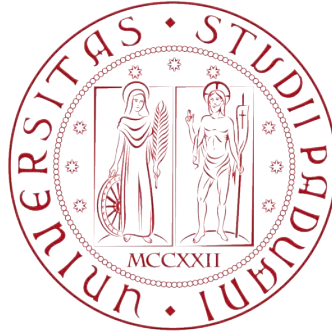
Supervisors:

Prof. Ernesto BENINI

Dr. Panagiotis LASKARIDIS

Dr. Drewan SANDERS

April 2020



MSC IN AEROSPACE ENGINEERING

MSC THESIS

Academic Year: 2018-2019

ANNALISA TRESOLDI

CFD Modeling and Analysis of a Boundary Layer Ingesting S-shaped Intake

Supervisors:

Prof. Ernesto BENINI

Dr. Panagiotis LASKARIDIS

Dr. Drewan SANDERS

April 2020

Abstract

Dipartimento di Ingegneria Industriale

MSc in Aerospace Engineering

CFD Modeling and Analysis of a Boundary Layer Ingesting S-shaped Intake

by Annalisa TRESOLDI

This thesis consists of a CFD analysis of the performance and the efficiency of a boundary layer ingesting intake.

The conducted study is focused on the assessment of the behaviour of the internal flow passing through the intake, the evaluation of the intake performance and the percentage of boundary layer ingested varying the mass flow ratio.

The pressure recovery was used as a performance descriptor and it was evaluated for different intake designs for the mass flow ratios accounted, while the analysis of Mach number at the Aerodynamic Interface with the fan duct has set structural limits in the design of the intake. Finally, a particular focus was given to the study of the power saving coefficient, the describing factor of the efficiency of a BLI system put in relationship with a system dealing with the free stream.

The whole investigation neglects the external flow and the back of the engine, namely the fan duct and the fan nozzle components as well as their losses counting, to focus on the lip and S-shaped duct design and explore the main internal flow features through it.

The very first considerations were formulated for a baseline case that aimed to represent a 2D clean fuselage without wings, tail and BLI engine in order to learn about the behaviour of the airflow and the development of the boundary layer over a conventional aircraft characterized with podded engines.

Later, a modelled engine was integrated into a new two-dimensional geometry simulating the embedded configuration to study the phenomenon of the flow capturing and, thus, of the boundary layer profile developed along the fuselage.

It mainly consists of a BLI engine installation all-around a tubular fuselage, positioned at the rear of the aircraft to ingest the thickest boundary layer possible. This kind of geometry was created for different shapes of the lip, throat heights and contraction ratio, while the structure of the S-shaped duct was built up to ensure a uniform flow at the AIP.

A parametric study was conducted with the aim of providing an understanding of the effect of design parameters on BLI intake. Both the baseline and embedded geometry were built using Matlab code, later the meshing generation was realized on ICEM in order to be able to run a Computational Fluid Dynamic (CFD) study on it using the Fluent solver. The $k-\omega$ SST turbulence model was selected, as it is considered to be a suitable model to study separated flows.

All the simulations were performed at the aero design point, meaning an altitude set at 11,000 m and a flying Mach number set at 0.78. Finally, when the convergence of the model was confirmed, flow behaviour was assessed, especially at the AIP. For all the cases taken into account, the parametric study conducted with CFD was performed after developing two turbulent boundary layer profiles investigated for different MFRs. One of the boundary layer profile was extracted from the clean fuselage, and the other was modelled using the embedded configuration and using the definition of 99% of the free stream velocity.

The amount of boundary layer ingested depended on the mass flow ratio which was evaluated respect to the outlet of the duct and a suitable interface point ahead of the intake along the fuselage where the difference in static pressure respect to the clean fuselage was relevant due to the presence of the nacelle.

The difference in pressure recovery was assessed within the different cases taking into account its trend in the upstream diffusion region and through the S-duct. The results from the simulations have shown a similar trend of the pressure recovery for all the designs accounted for, highlighting how the mass flow ratio, the throat height and CR had a significant impact on performance. Generally, the parametric study has shown an increase of the pressure recovery upstream of the intake for the highest mass flow ratios considered ($MFR \sim 1$), while the pressure losses related to the skin friction inside the duct resulted in being significant by increasing the inlet velocities. In this study, from the comparison between sharp, and elliptic lip intakes for a free-stream Mach number of 0.78, a better performance was provided by the thinner lip in terms of pressure recovery, although the high risk of lip flow separation characterizing a lower CR for $MFR < 1$.

UNIVERSITÁ DEGLI STUDI DI PADOVA

Sommario

Dipartimento di Ingegneria Industriale

MSc in Aerospace Engineering

CFD Modeling and Analysis of a Boundary Layer Ingesting S-shaped Intake

by Annalisa TRESOLDI

Il lavoro di tesi qui presentato consiste in un'analisi CFD delle prestazioni e dell'efficienza della presa dinamica di un motore a ingestione dello strato limite.

Lo studio condotto è incentrato sul valutare il comportamento del flusso interno alla presa, e quindi la percentuale di strato limite ingerito al variare del rapporto delle aree. Il recupero di pressione è stato considerato come indice di ottimalità di prestazione ed è stato valutato per diverse configurazioni della presa dinamica al variare dei rapporti delle aree considerati, mentre l'analisi dell'andamento del numero di Mach in prossimità dell'AIP ha posto dei limiti di progettualità della presa dinamica stessa.

Infine, una particolare attenzione è stata riposta sullo studio del power saving coefficient, parametro esplicativo dell'efficienza di un sistema a BLI posto in relazione a un sistema investito da solo flusso libero. In tutta la trattazione è stato trascurato il flusso che lambisce il profilo esternamente e la parte posteriore del motore a partire dal condotto del fan fino al suo ugello, per focalizzare l'attenzione sul design dei componenti principali della presa dinamica e sul comportamento del flusso al suo interno.

Il modello geometrico di riferimento iniziale rappresenta un modello di fusoliera 2D privo di motore a ingestione di strato limite al fine di poter studiare il comportamento del flusso che lambisce il profilo aerodinamico di un tradizionale aereo civile, e quindi valutare come il profilo di strato limite si sviluppa su di esso.

Successivamente, al modello base è stato integrato un motore a ingestione di strato limite per poter simulare il fenomeno di cattura del tubo di flusso e quindi dello strato limite che si sviluppa sulla fusoliera. Questo motore consiste principalmente in un'installazione circolare attorno a tutta la fusoliera e posizionato in coda al velivolo in modo da poter ingerire uno spessore di strato limite più elevato possibile. Molteplici prese dinamiche con diversi spessori del labbro, altezze di area di gola e diverso rapporto di contrazione sono state prese in considerazione in modo da valutare il comportamento del flusso per i diversi rapporti delle aree. Inoltre, per questa ricerca, è stata costruita una presa dinamica caratterizzata da un condotto a S in modo da migliorare le condizioni di uniformità del flusso all'interfaccia con il fan.

Tutte le geometrie a cui è stato fatto riferimento sono state create e parametrizzate con un codice Matlab, mentre il pacchetto Ansys ICEM e RANs solver Fluent è stato utilizzato per generare la mesh dei profili e condurre lo studio computazionale CFD. Il modello turbolento considerato è stato il $k-\omega$ SST dal momento che è stato valutato adatto e idoneo allo studio di flussi separati. Tutte le simulazioni sono state effettuate in condizioni di crociera caratterizzate da un'altitudine di 11,000 m e considerando un numero di Mach di volo di 0.78.

Infine, una volta raggiunta la condizione di convergenza del modello è stato valutato il comportamento del flusso attraverso la presa S-duct, e in particolare all'uscita della stessa, ossia all'ingresso del fan.

Per tutti i casi analizzati, lo studio parametrico è stato effettuato dopo aver sviluppato e ricavato un profilo di spessore di strato limite turbolento facendo riferimento alla definizione di spessore di strato limite pari al 99% della velocità del flusso libero. L'ammontare di strato limite ingerito dipenderà dai diversi rapporti delle aree ricavati dalle geometrie studiate.

I risultati ricavati dalle simulazioni hanno dimostrato come il rapporto delle aree, l'altezza dell'area di gola e il rapporto di contrazione abbiano avuto un impatto significativo sulle prestazioni. Il principale confronto condotto tra un profilo sottile e un profilo ellittico del labbro della presa ha permesso di valutare le perdite di pressione totale sia all'interno del condotto fino all'AIP, sia a partire da una zona di interfaccia sulla fusoliera, in cui è stato determinato uno spessore di strato limite significativo per l'analisi.

Complessivamente, lo studio parametrico ha evidenziato un incremento del recupero di pressione nella regione di pre-diffusione per più alti valori del rapporto delle aree ($MFR \sim 1$), mentre le perdite di pressione dovute all'attrito a parete sono risultate notevoli aumentando la velocità del flusso in ingresso alla presa. Prestazioni migliori sono state valutate per il profilo più sottile della presa che, con un basso $CR \sim 1.1$, è risultato più efficiente per il Mach di volo considerato, nonostante l'elevato rischio di separazione del flusso in prossimità del labbro della presa al diminuire del rapporto delle aree.

Acknowledgements

Firstly, my sincere gratitude goes to my supervisor Dr. Drewan Sanders who showed great understanding and provided immense encouragement. Thank you very much for being patient with my progress and for providing the necessary guidance.

I would like to show my appreciation to Dr. Panagiotis Laskaridis for introducing me to this topic and giving me the possibility to work on such an innovative subject. In a particular way, I am grateful to my professor and supervisor Dr. Ernesto Benini that gave me the opportunity to work with one of the best leading universities in the aerospace sector. Thank you for believing in me and for providing me with the best support.

A special thanks to all my friends and colleagues that have spent this time abroad besides me. You are all unique. I sincerely want to thank them, especially Mattia, Alberto, Andrea, Luca and Mudassir for their enthusiasm and for making this experience unforgettable. The memories and time spent with you all during this period are one of the treasures I will always cherish. I would also like to thank all my darling friends that from Italy have always believed in me making me feel proud of my choice on such a challenging MSc degree.

Finally, there are no words to describe how thankful I am to my family and my boyfriend Alessandro for their unconditional love and support.

Contents

List of Figures	xiii
List of Tables	xvii
Abbreviations	xix
Symbols	xxi
1 Introduction	1
1.1 Project aim	3
1.2 Objective and Methodology	3
1.3 Thesis structure	4
2 BLI Background	5
2.1 What is the Boundary Layer?	5
2.2 Boundary Layer Characteristics	9
2.2.1 Navier Stokes Equations	9
2.2.2 Reynolds Number and Regime of the Flow	12
2.2.3 Boundary Layer Dimensions	16
2.3 Boundary Layer Ingestion Phenomenon	19
2.3.1 A Theoretical Approach to BLI Concept	19
2.3.2 Ingested Drag of a BLI System	24
2.3.3 Efficiency and Power Saving Coefficient	27
2.4 BLI Benefits Analysis	29
2.4.1 BLI Literature Review	33
2.4.2 STARC-ABL Project	34
2.4.3 DisPURSAL Project: (PF) Propulsive Fuselage	35
2.4.4 D8-Double Bubble Concept	38
2.4.5 BWB Concept	39
2.4.6 A17-Zephyr	40
2.5 BLI Inlet Modelling	41
2.5.1 Intake and S-duct Design	41
2.5.2 Lip Design	46
2.5.3 Inlet Pressure Recovery	49
2.5.4 Mass Flow Ratio (MFR)	51

2.5.5	CFD and Turbulence Model	52
3	Methodology	57
3.1	Baseline Geometry and Sizing	60
3.1.1	Aircraft Initial Condition	61
3.2	Mesh Generation	63
3.3	Simulation Setup	67
3.3.1	Boundary conditions	69
3.4	Convergence Study	70
3.5	Post Processing	72
3.5.1	Extraction of the Boundary Layer Profile	73
4	Methodology for BLI System	77
4.1	Geometry and Domain	78
4.2	Intake Design	79
4.3	S-duct Design	81
4.4	Mesh Generation	85
4.4.1	Mesh Convergence	89
4.5	Boundary Condition and Simulation Setup	92
4.6	CFD-Post and Results	94
4.6.1	Mass Flow Ratio (MFR)	94
4.6.2	Approach to the Analysis	98
5	Results and Discussion	105
5.1	Results of the Elliptical Lip (Design A)	105
5.2	Results of the Naca Cowl and $\frac{1}{4}$ Ellipse Lip (Design B)	115
5.3	Pressure Recovery Analysis	123
5.3.1	Pressure Recovery and MFR	128
6	Power Saving Coefficient	135
6.1	Method of Analysis	138
7	Conclusion	143
8	Further Works	147

List of Figures

2.1	Boundary layer flow on a flat plate at zero incidences	7
2.2	Boundary layer separation over a cylinder	8
2.3	Comparison of flow past a sharp flat plate at low and high Reynolds numbers: (a) laminar, low-Re flow; (b) high-Re flow	14
2.4	Boundary layer along an airfoil illustrating separation	15
2.5	Displacement thickness estimation	17
2.6	Shape factor indication of the boundary layer profile	18
2.7	Podded and 100% BLI engines configurations	21
2.8	Propulsion system control volume and station definition	25
2.9	Comparison of BLI and Non-BLI in Mass Flow and Efficiency	30
2.10	Evolution of Mach number from free stream to AIP, 1=diffusion by the airframe, 2=diffusion by the pre compression zone, 3=diffusion by the inlet duct	31
2.11	STARC-ABL Concept	34
2.12	Distributed propulsion concepts with BLI	36
2.13	Propulsive Fuselage concept (up) and main components of after fan (down)	37
2.14	D8 Double Bubble concept developed within NASA N+3 project	38
2.15	Evolution of the D8-series concept	39
2.16	Conceptual design for BWB H3.4 configuration	40
2.17	A-17 tail view with BLI aft-prop	41
2.18	Schematic diagram of a nacelle profile	43
2.19	Side-view diagram of a inlet design parameters for BLI	43
2.20	Scheme of bends with a low radius of curvature	44
2.21	Scheme of bends with a high radius of curvature	45
2.22	Flow Separation	46
2.23	Influence of throat Mach number and capture flow ratio on total pressure losses	47
2.24	Inlet lip Mach number variation with the lip contraction ratio and throat Mach number	48
2.25	S-duct stations	49
2.26	Collected data on pressure recovery of subsonic intakes	50
2.27	Airflow demand at various conditions for BLI engine	51
2.28	Turbulent Boundary Layers	54
2.29	Different regions in boundary layer	55

2.30	Wall Modelling Strategies	56
3.1	Flow diagram of the main steps of the work process	59
3.2	2D Aircraft geometry: clean fuselage of the baseline geometry	60
3.3	Domain around the clean fuselage in the baseline geometry	62
3.4	Meshing around the clean fuselage	64
3.5	Smoothness of the meshing along the fuselage	65
3.6	2D planar blocking generation	66
3.7	O-grid generation	66
3.8	Residuals	70
3.9	Static Pressure for different mesh size	72
3.10	Mach Number Contour-clean fuselage	73
3.11	Total Pressure Contour-clean fuselage	74
3.12	Boundary layer thickness profile from the nose to the end of the fuselage (24 m)	75
3.13	Boundary layer velocity profile calculated at the end of the fuselage (24 m)	75
4.1	2D Aircraft geometry :Fuselage with the intake (Case 2)	78
4.2	2D Aircraft domain	79
4.3	2D Lips geometry: Elliptical lip shape profile on the left and Naca cowl external lip on the right	80
4.4	Wall contour shapes of contractions tested	82
4.5	S-duct main design parameters	84
4.6	General meshing domain with BLI engine	86
4.7	Blocking automation (Design B)	87
4.8	O-grid generation (Design B)	87
4.9	Blocking automation and C-grid generation around the nacelle (Design B)	87
4.10	Mesh around the elliptical lip (Design A)	88
4.11	Mesh around the sharp lip (Design B)	89
4.12	Inlet pressure recovery within coarse, medium and fine mesh (MFR=0.85, Design A)	90
4.13	Static Pressure along the fuselage within coarse, medium and fine mesh (MFR=0.85, Design A)	91
4.14	Difference in static pressure at the proximity of the inlet (roughly 24m) in coarse, medium and fine mesh. (MFR=0.85, Design A)	91
4.15	Mach Number Contour-MFR influence on the intake (Design B, AR=6, CR=1.10, M=0.78, $H_{throat}=0.4038$ m, MFR=0.56)	97
4.16	Contour of Stream Function (Design B, AR=6, CR=1.10, M=0.78, $H_{throat}=0.4038$ m, MFR=0.56)	97
4.17	Mach Number Contour-MFR influence on the intake (Design B, AR=6, CR=1.10, M=0.78, $H_{throat}=0.4038$ m, MFR=0.97)	97
4.18	Contour of Stream Function (Design B, AR=6, CR=1.10, M=0.78, $H_{throat}=0.4038$ m, MFR=0.97)	98

4.19	Static pressure comparison between the geometry of the clean fuselage and the geometry with the BLI system. Graphical representation of the point of divergence. (Design B, AR=6, CR=1.10, M=0.78, H_{throat} =0.4038 m, MFR=0.97)	99
4.20	Comparison of the pressure coefficient of the clean fuselage and the geometry with the BLI system (Design B, AR=6, CR=1.10, M=0.78, H_{throat} =0.4038 m, MFR=0.56)	100
4.21	Streamline of the flow ingested (Design B, AR=6, CR=1.10, M=0.78, H_{throat} =0.4038 m, MFR=0.97)	101
4.22	Boundary layer thickness profile from the nose to roughly 24 m (Design B, AR=6, CR=1.10 M=0.78, H_{throat} =0.4038 m, MFR=0.56)	102
4.23	Boundary layer velocity profile at the point of divergence (roughly 19 m) (Design B, AR=6, CR=1.10, M=0.78, H_{throat} =0.4038 m, MFR=0.56)	103
5.1	Schematic representation of Design A	106
5.2	Mach numbers at the throat of the duct (Design A)	107
5.3	Boundary layer thickness profiles (Design A)	109
5.4	Static Pressure along the fuselage (Design A)	110
5.5	Static Pressure Contour (Design A, AR=3, CR=1.25, M=0.78, H_{throat} =0.3590 m, MFR=0.85)	110
5.6	Static Pressure Contour (Design A, AR=3, CR=1.25, M=0.78, H_{throat} =0.3590 m, MFR=0.56)	111
5.7	Comparison of Mach Number at the AIP (Design A)	112
5.8	Mach Number Contour (Design A, AR=3, CR=1.25, M=0.78, H_{throat} =0.3590 m, MFR=0.56)	113
5.9	Mach Number Contour Design A, MFR=0.56	113
5.10	Percentage of boundary layer ingested respect to the variation of MFR (Design A)	114
5.11	Schematic representation of Design B	115
5.12	Boundary layer thickness profiles (Design B)	117
5.13	Static Pressure along the fuselage (Design B)	117
5.14	Static Pressure Contour (Design B, AR=6, CR=1.10, M=0.78, H_{throat} =0.4038 m, MFR=0.56)	118
5.15	Static Pressure Contour (Design B, AR=6, CR=1.10, M=0.78, H_{throat} =0.4038 m, MFR=0.97)	118
5.16	Comparison of Mach Number at the AIP (Design B)	119
5.17	Mach Numbers at the throat of the duct (Design B)	120
5.18	Percentage of boundary layer ingested respect to the variation of MFR (Design B)	121
5.19	Lip separation Design A, MFR=0.56	122
5.20	Lip separation Design B, MFR=0.56	122
5.21	Total Pressure loss (Design A, AR=3, CR=1.25 M=0.78, H_{throat} =0.3590 m, MFR=0.85)	124

5.22	Total Pressure loss (Design A, AR=3, CR=1.25 M=0.78, $H_{throat}=0.3590$ m, MFR=0.56)	125
5.23	Total Pressure distribution at the AIP (Design A)	125
5.24	Total Pressure distribution at the AIP (Design B)	126
5.25	Pressure coefficient distribution along the fuselage (Design A) . . .	127
5.26	Pressure coefficient distribution along the fuselage (Design B) . . .	127
5.27	Pressure recovery (Design A): from the AIP to the divergence point (PINK POINTS); from the outlet to the throat (RED POINTS); from the throat to the divergence point (BLACK POINTS); from the highlight to the divergence point (BLUE POINTS)	129
5.28	Pressure recovery (Design B): from the outlet to the divergence point (PINK POINTS); from the outlet to the throat (RED POINTS); from the throat to the divergence point (BLACK POINTS); from the highlight to the divergence point (BLUE POINTS)	130
5.29	Comparison of overall pressure recovery for different MFRs	132
6.1	Necessary power for a constant thrust at varying inlet velocities . .	137
6.2	PSC results	140
6.3	Comparison of propulsive power for BLI and no-BLI engine	141

List of Tables

2.1	Comparison of advantages and drawbacks for podded and embedded engines	33
3.1	Fuselage geometrical parameters	60
3.2	Data parameters at cruise condition	61
3.3	Number of nodes around the domain	65
3.4	Under-Relaxation Factors	68
3.5	Mesh size variation	71
4.1	Lips design	80
4.2	Geometrical characteristics of S-duct	84
4.3	Number of nodes around the domain	86
4.4	Number of nodes for each mesh size	89
4.5	Convergence of the model	90
4.6	MFRs studied for Design A	95
4.7	MFRs studied for Design B	95
4.8	Influence of MFR on intake design	96
5.1	Main results Design A	106
5.2	Main results Design B	115
6.1	Inlet conditions for BLI engine and isolated fan	138

Abbreviations

CFD	Computational Fluid Dynamics
BLI	Boundary Layer Ingestion
MFR	Mass Flow Ratio
CFD	Computational Fluid Dynamics
IPR	Inlet Pressure Recovery
FPR	Fan Pressure Ratio
AIP	Aerodynamic Interface Plan
NPF	Net Propulsive Force
PSC	Power Saving Coefficient
TSFC	Thrust Specific Fuel Consumption
BL	Boundary Layer
PR	Pressure Recovery
AR	Aspect Ratio
CR	Contraction Ratio
SST	Shear Stress Transport
BWB	Blended Wing Body
DB	Double Bubble
STARC-ABL	Single-aisle Turboelectric Aircraft with Aft-Boundary Layer Propulsion
SUGAR	Subsonic Ultra Green Aircraft Research
DisPURSAL	Distributed Propulsion and Ultra-high by-pass Rotor Study at Aircraft Level
PF	Propulsive Fuselage
RANS	Reynolds-Averaged Navier-Stokes equations

DNS	D irect N umerical S imulation
LES	L arge E ddy S imulation

Symbols

C_p	profile pressure coefficient
D	drag
M_∞	free-stream Mach number
y^+	non-dimensional wall distance
M_t	throat Mach number
p_0	free-stream pressure
R	universal gas constant
q	vector heat transfer
Re	Reynolds number
U_∞	free-stream velocity
\bar{x}	point of divergence x-axis
\dot{m}_{target}	target mass flow rate
\dot{m}_{out}	outlet mass flow rate
$h_{\bar{x}}$	height in divergence point
a	semi-major axis
b	semi-minor axis
H	shape factor
H_i	contraction height at the inlet
H_e	contraction height at the exit
Hm_i	inlet average mean line
Hm_e	outlet average mean line
D_i	inlet height
D_e	outlet height

Δh	inlet height
X'	non-dimensional streamwise distance: X/L and spanwise directions, respectively
P_{BLI}	engine BLI power
P_{podded}	engine podded power
F_{engine}	engine thrust
F_N	engine net thrust
F_G	engine gross thrust
u_j	exit engine velocity
u_w	wake engine velocity
u_τ	friction velocity
γ	specific heat ratio
δ_{BL}	boundary layer thickness
δ^*	displacement thickness
θ	momentum thickness
θ^*	momentum thickness
Φ	viscous dissipation function
$\Phi_{nacelle}$	nacelle force
μ	dynamic viscosity
ν	kinematic viscosity
ρ	density
η	efficiency
τ_{ij}	viscous stresses
τ_w	skin friction drag

Chapter 1

Introduction

The principle behind the Boundary Layer Ingestion (BLI) concept comes from the necessity, in the airline business, to reduce fuel consumption.

Indeed, specific fuel consumption represents one of the most crucial performance parameters of the engine that needs to be minimized to reduce emissions, to improve the reliability and maintainability and to lead to an environmentally friendly civil aviation industry.

To reduce fuel burn, aviation moved from turbojet with high jet velocity to high by-pass ratio turbofan with larger frontal areas and lowered specific thrust. This has resulted in higher propulsive efficiency along with remarkable reductions in fuel consumption. Although the trend has been and continues to be in developing higher by-pass ratio engines to save on fuel consumption [1], limitations occur in the design process where larger diameters demanded by higher and higher by-pass ratio result in a higher level of nacelle and installation drag. Moreover, materials used in modern gas turbine blades have to face with a harmful growth in temperature that can't be sustained without increasing in weight and using proper cooling techniques.

Looking at all these aspects, the BLI concept offers an innovative, but not so recent, opportunity to enhance the current engine aircraft configuration and performance, integrating the engine to the airframe.

An embedded engine in the fuselage exploits the possibility to ingest the slowed air of the boundary layer developed along the aircraft into the inlet of the engine and reenergize it through the engine jet. Since the boundary layer generates additional drag, its ingestion and then acceleration provides a reduction in terms of the overall aircraft drag and, therefore, a lower requirement in gross thrust to achieve the same net propulsive force. Moreover, with this kind of engine structure there is no need of structural components such as pylons or the nacelle around the engine that are both source of drag.

The benefits of the BLI architecture mainly consist of reducing fuel burn and noise, however, functional aspects are overcome by several drawbacks. Thanks to the ingestion of the lower energy boundary layer, the specific thrust drops, allowing the increase of the propulsive efficiency, but at the same time, it leads to a total pressure loss and the generation of flow distortion due to a non-uniform velocity profile along the airframe. These are the principal adverse aspects that negatively and strictly affect both the inlet and engine efficiency. Hence, they are still matter of study to give a practical shape to this future concept of distributed propulsion.

This investigation deals with the parametric analysis of a BLI engine located at the rear end of the airframe, embedded in the fuselage (a tubular body) and featured with an S-duct diffuser. The S-duct shape provides a lower wetted area, but it may require a careful analysis of the flow distortion at the AIP because of the possible flow separation along the curvature.

1.1 Project aim

This project aims to examine and evaluate the performance of the boundary layer ingestion in a conventional aircraft fitted with an aft-fan engine through a parametric study conducted with a CFD simulation.

The analysis concerns the investigation of the design process of an S-duct intake and the exploration of the main flow features through it.

The baseline geometry of this engine deals with different shape of the lip, throat height and CR of the intake in order to evaluate the flow behaviour at different mass flow ratios, and the structure of the S-shaped duct is built up in order to ensure a uniform flow at the AIP.

1.2 Objective and Methodology

The main objectives of this project are:

- Literature review on BLI and examination of previous work performed on it
- Identification of the main intake design parameters regarding BLI architectures
- Generation of a 2D streamlined lip and intake geometry and optimization of the mesh based on previous studies
- Computation of the flow behaviour due to the boundary layer ingestion
- Modifications of the geometry to reduce possible losses
- Fluid dynamics simulation for several values of mass flow ratio
- Investigation of the effect of the boundary layer ingestion at flight operating condition on the principal design parameters such as pressure recovery, static pressure and Mach number at AIP

- Quantification of the benefits of the finest design and summary of the proposals for the following study on embedded fan with S-duct intake.

The procedure undertaken for the realization of this project has required the use of different software:

- **MATLAB** Generation of graphic and geometric support scripts and import data for the post-processing analysis
- **Ansys ICEM** Meshing of the different geometric profiles
- **Ansys Fluent** Simulations, pre and post-processing.

1.3 Thesis structure

In the following chapters, a theoretical standpoint is firstly presented to more easily understand the physics behind this new engine architecture and to aid the investigation of this thesis. A literature review is then taken into account to explain the general background around the BLI concept, its main principles and a basic understanding of the distributed propulsion.

Afterwards, the methodology chosen for this study is described along the whole design process. Firstly the geometry generation and the computational analysis involved with the CFD simulation are presented, and later, the elaboration of results data and the validation of the model are systematically discussed. Finally, a conclusion on it is given, and remarks and recommendations for further work related to this project represent the latest part of this thesis.

Chapter 2

BLI Background

This Chapter firstly presents some theoretical key concepts about the boundary layer phenomenon for fundamental understanding. Then, the essential benefits deriving from the boundary layer ingestion are explained. Finally, a general overview of the BLI idea investigated in recent years is introduced in order to give basic knowledge about the main achievements developed and the principle technical challenges for future applications.

2.1 What is the Boundary Layer?

As an object moves through a fluid, the molecules of the fluid near the object are disturbed and move around the object. Aerodynamic forces are generated between the fluid and the object. The magnitude of these forces depends on different factors such as the shape and the speed of the object, the mass of the fluid going by the object and two other important properties of the fluid: the viscosity and the compressibility of the fluid.

Viscosity μ can be defined as the ability of a fluid to resist deformation by shear stresses τ , and as a fluid property, it affects the aerodynamic forces in a complicated way.[2]

For instance, considering the flow of a fluid over a solid surface, the influence of friction between the surface and the fluid adjacent to the surface acts to create a frictional force which retards the relative motion. This has an effect on both the surface and the fluid because the surface feels a *tugging* force in the direction of the flow, tangential to the surface and defined above as *shear stress* τ . [3]

Whereas, as an equal and opposite reaction, the molecules right next to the surface feel a retarding force that sticks them to the surface and decreases their local flow velocity. The fact that the flow adheres to the surface means that the influence of friction is to create a zero velocity property in a thin layer right at the body surface, which is called the *no-slip* condition for viscous flow.

In this way, the molecules just above the surface are slowed down, while the farther ones far away from the surface are less affected by the presence of the object and their velocity increases until it reaches the free stream velocity.

This phenomenon creates "A thin layer of fluid near the surface in which the velocity changes from zero at the wall (no-slip) to its full value which corresponds to external frictionless flow. The layer under consideration is called the boundary layer".[4]

From this definition, it can be asserted that depending on the viscosity of the fluid, which is affecting the object, the thickness of the thin layer changes and decreases with decreasing it. Accounting small viscosities, there are two main regions the field of flow can be split into: the thin boundary layer near the wall, in which friction must be taken into account, and the region outside the boundary layer, where frictional forces are small and may be neglected, and where, therefore, the perfect fluid theory offers an excellent approximation.[3] However, as can be observed in Figure 2.1 below, even with very modest viscosity the frictional shearing stresses are considerable because of the large velocity gradient across the flow which is mathematically explained by the law of viscosity:

$$\tau(y) = \mu \frac{\partial u}{\partial y} \quad (2.1)$$

In particular, the figure shows how the velocity profile in such a boundary layer at the plate changes from a uniform distribution in front of the leading edge to the constant growth of thickness δ moving further in the downstream direction.

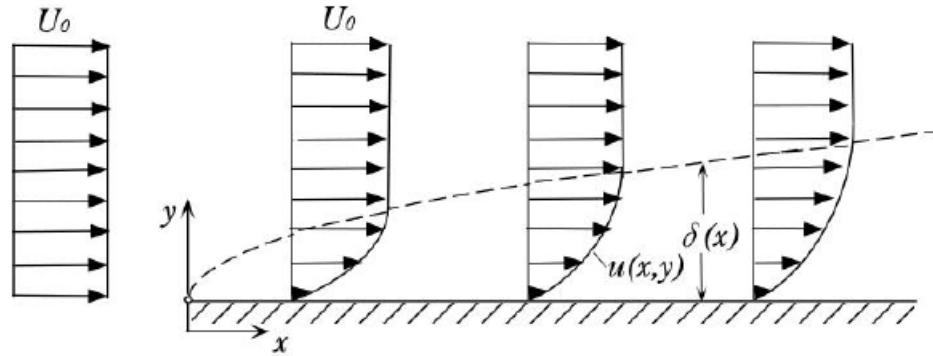


FIGURE 2.1: Boundary layer flow on a flat plate at zero incidences [4]

When the thickness increases significantly in the downstream direction, the flow may separate, which means that the flow in the boundary layer becomes reversed and detaches from the surface characterizing the so-called *boundary-layer separation* phenomenon.

The conceptual reason of this event can be explained assuming that the flow over the surface produces an increasing pressure distribution in the flow direction, namely an adverse pressure gradient, which forces the movement of the particles, already retarded by the effect of friction, to withstand the increasing pressure as well, which consequently tends to reduce its velocity further. As the fluid element continues to move downstream, it may ultimately come to a stop, and then, under the action of the adverse pressure gradient, actually reverse its direction and start moving back upstream.

As seen from Figure 2.2, the separation of the flow leads to the formation of a wake of sharply decelerated flow behind the body, associated with the formation of vortices, and with high energy losses due to the adverse pressure gradient.

The flow separation especially takes place near blunt bodies such as cylinders and spheres because they are mostly affected by a deviation in pressure distribution and in general, the point of separation occurs when the mathematical condition $(\frac{\partial u}{\partial y}) = 0$ is satisfied, so that the wall shear stress is zero.

In summary, in addition to the generation of shear stress, the effects of viscosity and the influence of friction can cause the flow over a body to separate from the surface. When such separated flow occurs, the pressure distribution over the surface is greatly altered, and a further drag force is generated.

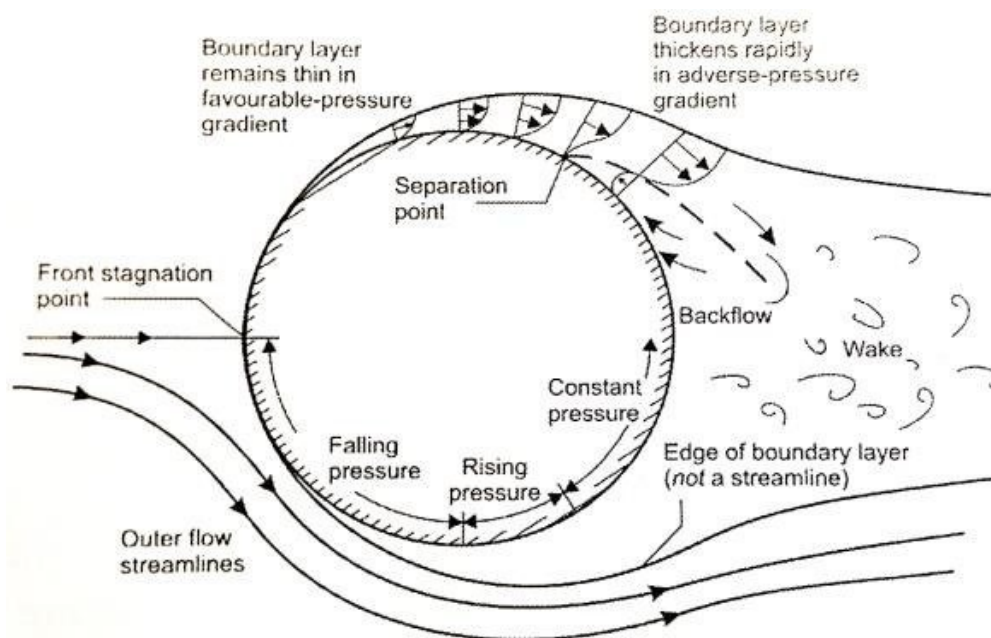


FIGURE 2.2: Boundary layer separation over a cylinder [5]

Along with the *skin friction drag*, the pressure drag, or *form drag* due to separation arises. The first one is the component in the drag direction of the integral of the shear stress τ over the body, while the second one is the component in the drag direction of the integral of the pressure distribution over the body. The sum of these contributions in drag is called the *profile drag* of a two-dimensional body.[3] However, the development of the wake and the consequences resulting from it dramatically affect the overall drag of the body.

In general, the boundary layer is considered to be detrimental to the performance of a conventional aircraft, as it contributes to drag and results in a momentum deficit, the wake. In this study, the boundary layer plays a key role in the development of the embedded engine enabling its ingestion (BLI) and, therefore, the increase of the propulsive efficiency.

On the other hand, the harmful behaviour of flow separation may occur within the intake due to the S-shaped duct design during ingestion. This event leads to a non-uniform pressure distribution at the AIP, causing the growth of a distorted flow that must be taken into account.

2.2 Boundary Layer Characteristics

2.2.1 Navier Stokes Equations

The basic equations of aerodynamics which describe the behaviour of the flow in a boundary layer can be derived from the Navier-Stokes equations for viscous flow. As extensions of the Euler Equations, they represent the mathematical model used to examine and describe how the main properties of the flow change during dynamic interactions. Velocity, pressure, temperature, density and viscosity of a moving fluid are all related and embodied in the Navier-Stokes equations, the development of which invokes three fundamental physical principles, namely: the conservation of mass, the conservation of momentum and the conservation of energy. [6]

All the underlying differential equations describing these laws can be derived by taking into account, in a Cartesian system of reference $(\partial x, \partial y, \partial z)$ for example, an elemental control volume of the flow, approximately one-dimensional, that passes through each side of the element and where all its properties are considered to be uniformly varying functions of time and position.

In order to give a general overview of the insidious Navier-Stokes equations, it's necessary to explore the origin of these physical principles behind the equations and highlight the most critical points of their derivation.

Starting from the conservation of mass, or the so-called *equation of continuity*, it states that the fluid mass of a one-dimensional flow passing through a control volume cannot change.

It deals with the variation of two important properties of the fluid that are the density of the mass flow and the velocity; both defined as continuum functions. That is, the flow may be either steady or unsteady, viscous or frictionless, compressible or incompressible. Moving on to the second principle, Newton's Law for a moving fluid can be developed from the same elemental volume taking into account different sources of forces acting on it, namely body forces and surface forces. Body forces are due to external fields such as gravity that acting on the differential mass within the element is defined as:

$$dF_{grav} = \rho g * dx dy dz \quad (2.2)$$

Whereas, the surface forces are due to the stresses on the sides of the control surface. These stresses are the sum of hydrostatic pressure and viscous stresses τ_{ij} that are proportional to the element strain rates and the coefficient of viscosity.

Finally, the conservation of energy is built on the first law of thermodynamics that deals with the energy exchange of a continuum system, as the fluid one in this context. It states that the total energy within the control domain remains fixed as energy is not created or destroyed but merely changes forms, going from potential to kinetic to thermal energy.

One essential aspect of this law is lead by the *Fouriers law of conduction* setting that the vector heat transfer per unit area, \mathbf{q} , is proportional to the vector gradient of temperature, ∇T and where similarly the *thermal conductivity* k plays the role of viscosity in the Newton's law.

The three basic differential equations of fluid motion, just described are summarize here:

- **Conservation of mass:**

$$\frac{\partial \rho}{\partial t} + \nabla \cdot \rho \mathbf{V} \quad (2.3)$$

- **Conservation of Momentum Flow:**

$$\rho \mathbf{g} - \nabla p + \nabla \cdot \boldsymbol{\tau}_{ij} = \rho \frac{\partial \mathbf{V}}{\partial t} \quad (2.4)$$

- **Conservation of Energy:**

$$\rho \frac{\partial \hat{u}}{\partial t} + p(\nabla \cdot \mathbf{V}) = \nabla \cdot (k \nabla T) + \phi \quad (2.5)$$

In their brief and compact form they introduce 5 unknowns: density ρ , pressure p , velocity \mathbf{V} , internal energy \hat{u} and temperature T forming five equations in these five unknowns.

All terms involved in the derivation have been generally present apart from ϕ , named the *viscous dissipation function*. [6]

At last, for a better understanding, \mathbf{V} represents a cartesian vector form of the velocity field that varies in space and time:

$$\mathbf{V}(r, t) = iu(x, y, z, t) + jv(x, y, z, t) + kw(x, y, z, t) \quad (2.6)$$

and ∇ is the gradient operator, defined as:

$$\nabla = i \frac{\partial}{\partial x} + j \frac{\partial}{\partial y} + k \frac{\partial}{\partial z} \quad (2.7)$$

Looking at these equations closely, they have no analytical solution because of their complexity, non-linearity, coupling and partial differentiability. There is just a little class of "exact" solutions obtained by the application of precise conditions to reduce the equations and to allow many terms in the Navier-Stokes solutions to be precisely zero, with the resulting equations being simple enough to solve.

Moreover the equations can be simplified by treating certain classes of physical problems for which some terms in the viscous flow equations are small and can be neglected.

This approach has been used in the boundary layer study where a certain order-of-magnitude assumptions have been done to greatly simplify the Navier-Stokes equations into boundary layer equations that are simpler, but still non-linear. The solution of the full viscous flow equations takes form with modern numerical techniques.

For example, *Computational fluid dynamics* (CFD) is now well developed and in conjunction with "exact" solutions for the inviscid flow equations carries over to exact solutions for the viscous flow equations.

2.2.2 Reynolds Number and Regime of the Flow

The thickness of the boundary layer increases with the distance from the leading edge, as shown in Figure 2.1, governing the way the air flows over the surface. Since the type of the boundary layer and its thickness influence the *skin friction drag* and because the flow separation influences the *form drag*, learning which factors control the growth and the shape of the boundary layer becomes essential. As explained in the previous section 2.1, the behaviour of the boundary layer depends on the pressure gradient in the direction of the flow. However, several other parameters such as velocity, density and viscosity are very relevant along with the geometrical shape of the body invested by the flow. The Reynolds number represents the coefficient that allows to connect all these factors and describe the flow dynamics. It is defined as the ratio of inertial forces to viscous forces, and taking flow past a flat plate, for example, it assumes this expression:

$$Re_L = \frac{UL}{\nu} \quad (2.8)$$

where U is the stream velocity, L is the characteristic linear dimension, the finite length of the plate in this case, and ν is the kinematic viscosity.

For high Reynolds numbers, the viscous forces can be neglected because they are minimal respect to the inertial forces. On the contrary, for low Reynolds numbers (< 1000), the inertial forces are prevalent respect to the viscous forces, and the behaviour of the fluid can't be defined as a perfect fluid.

The Reynolds number plays a vital role in the changeover of the flow in the external solution as well as inside the boundary layer described later in the next section. The flow ceases being smooth and steady *laminar* and becomes fluctuating and agitated *turbulent* through the so-called process of *transition* to turbulence.

Figure 2.3 well illustrates both the difference of the boundary layer behaviour between the two flow regimes and the fact that at higher Reynolds number, the patching of the viscous effects near solid walls with the outer inviscid motion is more successful.

For instance, taking a uniform stream U moving parallel to a sharp flat plate of length L , if the Reynolds number is low (Fig. 2.3a), the viscous region is vast and extends far ahead and to the sides of the plate. The plate retards the oncoming stream greatly, and small changes in flow parameters cause significant changes in the pressure distribution along the plate. A high-Reynolds-number flow is much more amenable to boundary layer patching. (Fig. 2.3b)

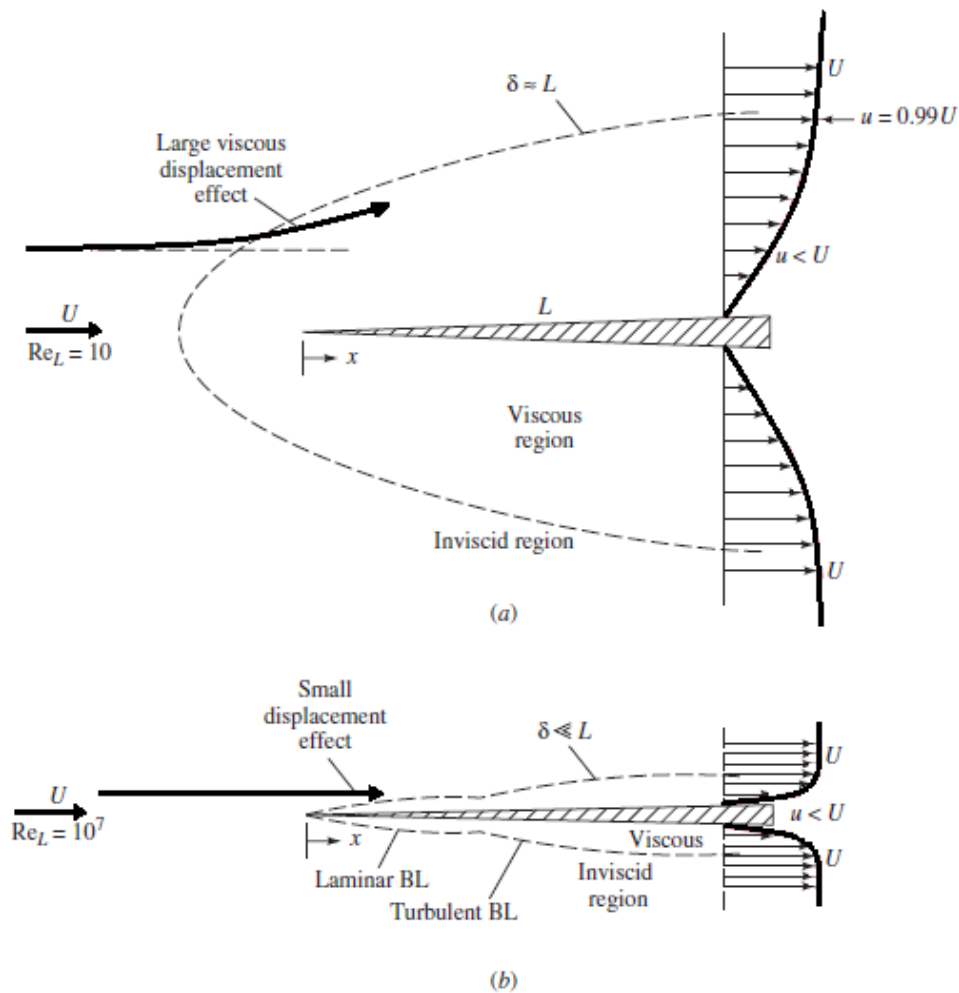


FIGURE 2.3: Comparison of flow past a sharp flat plate at low and high Reynolds numbers: (a) laminar, low-Re flow; (b) high-Re flow [6]

In all cases, these boundary layers are so thin that their displacement effect on the outer inviscid layer is negligible, especially for slender bodies, such as plates and airfoils parallel to the oncoming stream.

However, for a blunt-body flow, even at very high Reynolds numbers, there is a discrepancy in the viscous–inviscid patching concept.

Besides the theory, the interaction between viscous and inviscid layers is strong and non-linear, and even though the laminar flow theory is now well developed and many solutions are known, no analyses can simulate the random fluctuations of turbulent flow whose analysis typically uses empirical modelling laws to relate time-mean variables. [6]

A specific Reynolds number can be defined in function of a characteristic dimension of the profile x that governs the definition of the thickness of the boundary layer, accounting for an internal boundary layer solution.

In this context, the equation of reference is:

$$Re_x = \frac{Ux}{\nu} \quad (2.9)$$

The parameter x represents the exact position of the flow inside the boundary layer on which the Reynolds number is considered location to location. The boundary layer always deals with a transition from the laminar regime to turbulent.

Depending on the value of the Reynolds number, the boundary layers may be either laminar or turbulent; in particular, it is laminar for low Reynolds numbers. In contrast, for high Reynolds numbers, the boundary layer is turbulent and the streamwise velocity is characterized by unsteady swirling flows inside the boundary layer increasing its thickness. In Figure 2.4, the region of transition from the laminar regime to the turbulent is diagrammatically illustrated above the surface of an airfoil.

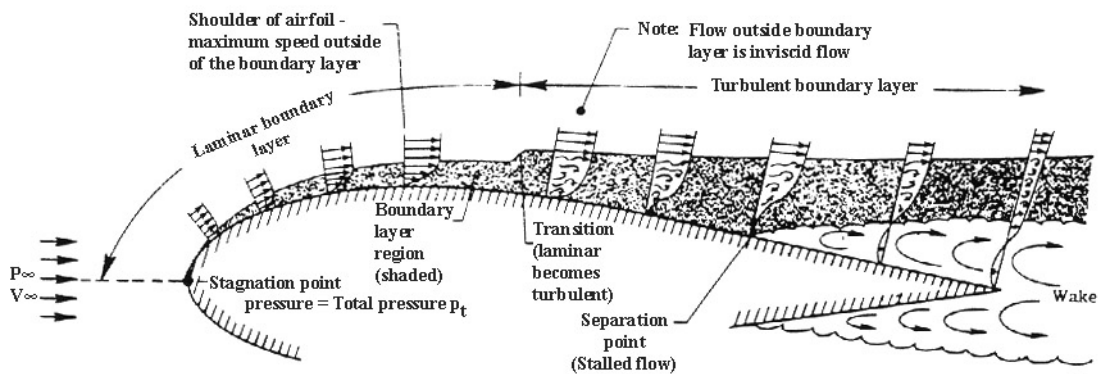


FIGURE 2.4: Boundary layer flow along an airfoil illustrating separation [7]

2.2.3 Boundary Layer Dimensions

It is possible to define the boundary layer thickness δ as that distance from the wall where the velocity u reaches 99 percent of the external velocity U .

According to the explanation in the previous section, it can be defined in terms of Reynolds number as :

$$\frac{\delta}{x} = \frac{1}{\sqrt{Re_x}} \quad (2.10)$$

From this general definition, δ for a smooth flat plate can be furthermore estimated for two flow regimes: laminar and turbulent.

$$\frac{\delta}{x} \approx \begin{cases} \frac{5.0}{Re_x^{1/2}} & \textit{laminar} & 10^3 < Re_x < 10^6 \\ \frac{0.16}{Re_x^{1/2}} & \textit{turbolent} & 10^6 < Re_x \end{cases} \quad (2.11)$$

This study focuses on turbulence in compressible flow, so the second expression of the system may be useful.

Along with the boundary layer thickness a number of additional dimensions that define the boundary layer are available: displacement thickness δ^* , the momentum thickness θ and the energy thickness θ^* . Each boundary layer thickness term represents the distance by which the surface would have to be displaced in an inviscid flow in order to result in the same mass flow, momentum or kinetic energy as the viscous flow.[4]

The displacement thickness indicates the distance by which the external streamlines just above the boundary layer are slightly shifted and displaced away from the wall due to the decrease in velocity in the boundary layer itself.

It is a physical measure of the boundary layer thickness that takes into account the mass flux deficit and is given by the equation:

$$\delta^* = \int_0^{\delta} \left(1 - \frac{u}{U}\right) dy \text{ or } \delta^* = \int_0^{\delta} \left(1 - \frac{\rho u}{\rho_{\infty} U}\right) dy \quad (2.12)$$

where u is the velocity at the vertical distance from the surface and U is the velocity at free-stream condition and the change in density (ρ) needs to be accounted for compressible flows (right equation) as it cannot be assumed constant such for the case of incompressible flows (left equation).

Figure 2.5 illustrates the displacement thickness estimation:

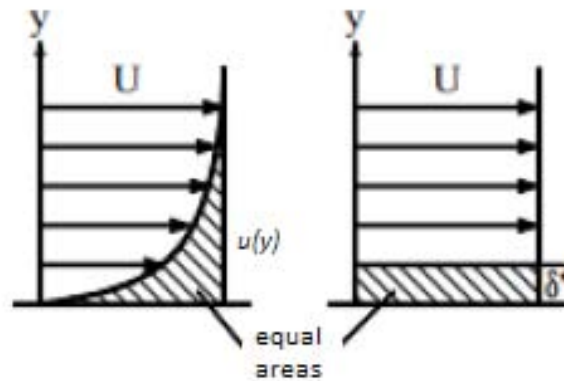


FIGURE 2.5: Displacement thickness estimation [8]

The momentum thickness is the distance by which a surface would have to be moved parallel to itself towards the reference plane in an inviscid fluid stream of velocity U to give the same total momentum as exists between the surface and the reference plane in a real fluid. The definition of the momentum thickness for incompressible flow is based on volumetric flow rate, as the density is constant:

$$\theta = \int_0^{\delta} \frac{u}{U} \left(1 - \frac{u}{U}\right) dy \text{ or } \theta = \int_0^{\delta} \frac{\rho u}{\rho_{\infty} U} \left(1 - \frac{\rho u}{\rho_{\infty} U}\right) dy \quad (2.13)$$

At last, the energy thickness represents the distance displaced to account for the energy flux deficit in the boundary layer, and it is defined by the equation:

$$\theta^* = \int_0^{\delta} \frac{u}{U} \left(1 - \left(\frac{u}{U}\right)^2\right) dy \text{ or } \theta = \int_0^{\delta} \frac{\rho u}{\rho_{\infty} U} \left(1 - \left(\frac{\rho u}{\rho_{\infty} U}\right)^2\right) dy \quad (2.14)$$

Another important parameter, used to estimate when the phenomenon of flow separation occurs, is the so called shape factor H , derived from the ratio of the displacement thickness to the momentum thickness:

$$H = \frac{\delta^*}{\theta} \quad (2.15)$$

Shape factor has always a value greater than 1 and larger its value, the more likely the boundary layer is near separation as can be easily observed in Figure 2.6:

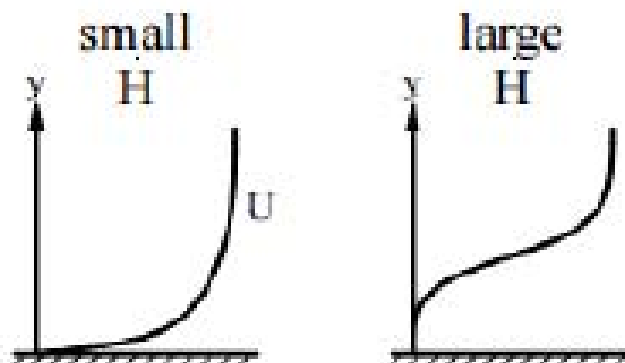


FIGURE 2.6: Shape factor indication of the boundary layer profile [8]

2.3 Boundary Layer Ingestion Phenomenon

Conscious now of what the boundary layer consists of from both a theoretical and physical standpoint, it is possible to take a step forward to explore what boundary layer ingestion deals with, which are the main characteristics that can lead to potential economic and environmental benefits, as well as the most severe drawbacks and limitations of its technology.

2.3.1 A Theoretical Approach to BLI Concept

The basic concept of BLI consists of moving the engine to the back of the fuselage to ingest the slowed air of the boundary layer coming from the fuselage.

It was shown that this could provide aircraft benefit by re-energizing the aircraft wake that enables less kinetic energy to be wasted. Indeed, exploiting the low momentum flow, an increase in propulsive efficiency is expected because of an overall reduction in drag. Subsequently, less gross thrust is required to generate the same net thrust for a given amount of mass flow, and this corresponds directly to a reduction in fuel consumption.(Ref. A.Plas [9])

The explanation suggested by Plas of what the boundary layer ingestion deals with, however, can be further described in terms of a ram drag standpoint.

Thanks to the boundary layer ingestion, “There’s still drag. Still a loss. But it’s less of a loss.” states James D Heidmann from NASA Glenn Research Center. [10] At its simplest, thrust, drag, weight and lift are the four major forces governing the equilibrium on a flying airplane. Whereas the lift offsets the weight to keep an airplane in the sky, drag tries to counteract the motion of the airplane given by thrust slowing it down. BLI deals specifically with the drag part of the equation by, ultimately, trying to reduce the total drag an airplane can experience during flight. As an airplane is invested by the air, the slower moving air of the boundary layer develops on the surface of the aircraft causing additional drag. At the front of it, the thickness of the boundary layer is almost zero, but as the air flows back over the surface of the airplane’s fuselage and wings, the layer grows thicker.

By the time it gets to the rear of the airplane, it can be more than a foot.[10]

In a conventional tube and wing airplane, where the jet engines are hung beneath the wings, the slower airflow can't be exploited as it just continues off the rear of the airplane ending up to mix with the undisturbed air. Something different happens when the airplane's engines are put in the path of the boundary layer, for example, by placing them at the extreme rear of the airplane. With the engines in this location, the slower air of the boundary layer enters the engine, or precisely, is ingested and then accelerated with the rest of the air passing through the engine and exhausted out the back.

The ingested boundary layer doesn't make the engines more or less powerful, but what really changes is the amount of drag that affects the performance of the aircraft. Ingestion of the lower kinetic energy flow allows the engine to produce propulsive power with a lower expenditure of kinetic energy in the exhaust jet compared to non-BLI configurations. In this way, the propulsive efficiency improves, leading to a reduction of airframe wake loss and thus reducing the total energy loss.

With less total drag, the engines need less thrust to push the airplane forward, and consequently, less fuel to burn and emissions.

The physical concept of boundary layer ingestion can be illustrated and easily understood looking at Figure 2.7 given by Plas [9], but first, some considerations need to be done.

The following representation and demonstration describe an easy simplification of the phenomenon involved in the ingestion of the boundary layer. The approach is for a quasi-one-dimensional case [11], an assumption of constant mass flow rate \dot{m} , u_∞ , and propulsion force was made. There is a lot of assumptions taken. Other than those mentioned above, the airframe drag, D_A , also assumed to be equal for podded and BLI configuration. The choice of an internal force control volume to estimate the performance of the propulsion system neglects various losses connected with the ambiguous split between the airframe and the propulsion system.

The flow that enters a BLI propulsion system has travelled over the aircraft surface, so the separation of the airframe and propulsion system is, therefore, more complicated for BLI-configuration respect to an isolated engine. Previous research on the simulation of BLI systems can be broadly split into two categories: computational fluid dynamics (CFD) analyses of the problem as a whole, and lower-order analytical methods which evaluate the system using boundary layer and propulsion system performance theory. CFD methods are useful for the analysis of the combined aircraft and propulsion system. However, it is important to be able to predict the performance of the propulsion system at a preliminary design stage without expensive experimental methods or complex and time-consuming simulations.[12]

Plas gave an ideal example of how local flow characteristics (such as boundary layer thickness or local free-stream velocity) influence the propulsion system performance and how the wake re-energization of a BLI system could influence the propulsion system requirements. The upper part of the figure shows the situation with no boundary layer ingestion, corresponding to conventional podded engines, and the lower part shows a situation with 100% of the aircraft wake ingested by the engine.

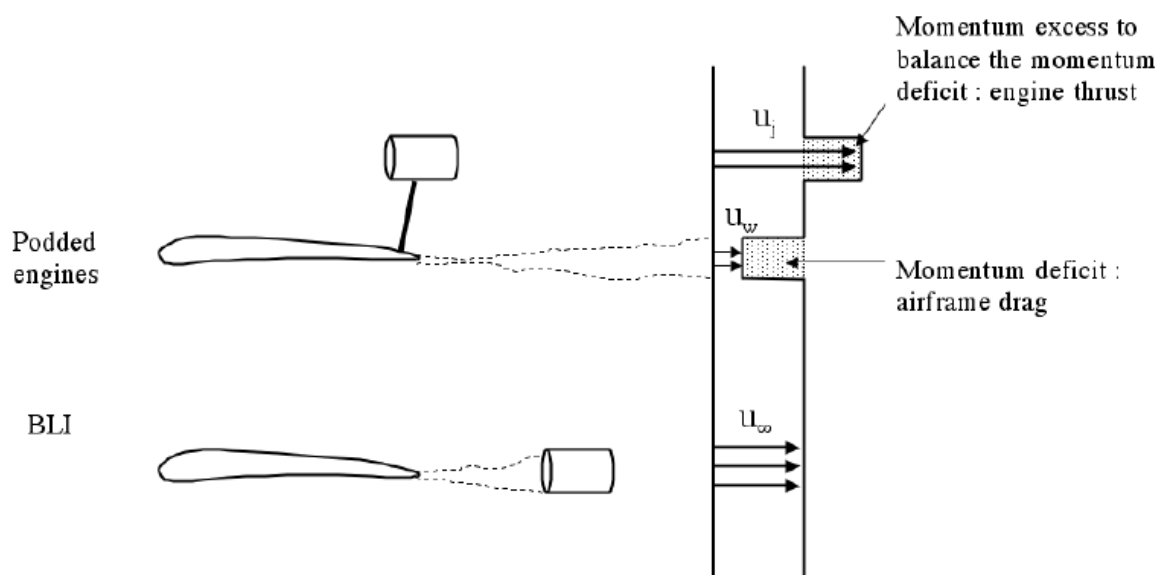


FIGURE 2.7: Podded and 100% BLI engines configurations [9]

With podded engines the flow entering has a free stream velocity u_{inf} then accelerated by the engine to a velocity u_i . This process creates excess momentum which is equal and balanced, for an ideally expanded nozzle, by the momentum deficit that occurs due to the airframe drag D_A .

The free-stream velocity u_∞ can be split into two velocity streams: the jet velocity u_j created by the flow accelerated by the engine and the average velocity u_∞ of the formed aircraft wake.

The crucial observation that can be made from this assessment is the potential benefit of lower power requirement obtained by having a 100% BLI with the basic idea of re-energizing the aircraft wake and thus preventing excessive loss of kinetic energy. Therefore, the thrust of the engine can be expressed through the difference between the velocity at the exit of the engine and the velocity far upstream of the engine in both cases thus:

$$F_{\text{engine}} = \dot{m}(u_i - u_\infty) = \dot{m}(u_\infty - u_w) = D_A \quad (2.16)$$

The additional power provided to the flow by the engine is proportional to the difference in kinetic energy per unit mass:

$$P_{\text{podded}} = \frac{\dot{m}}{2}(u_j^2 - u_\infty^2) = \frac{F}{2}(u_j + u_\infty) \quad (2.17)$$

This power added to the flow changes when the BLI engine is taken into account. In this case, all the wake is ingested and then accelerated by the engine from u_w to u_∞ leading to no changes in the aircraft drag and, hence, in the propulsive force which remains the same of the podded engine.

$$F_{\text{engine}} = \dot{m}(u_j - u_w) = \dot{m}(u_\infty - u_w) = D_A \quad (2.18)$$

However, something different happens with the additional power required to produce this force in the presence of boundary layer ingestion:

$$P_{BLI} = \frac{\dot{m}}{2}(U_j^2 - u_w^2) = \frac{\dot{m}}{2}(u_\infty^2 - u_w^2) = \frac{F}{2}(u_\infty + u_w) \quad (2.19)$$

By comparing the two equations of power, it is easy to prove the theoretical assumption about the main benefit of the BLI engine. Indeed, since u_w is lower than u_j , because of the boundary layer velocity profile, the velocity that enters the BLI engine is lower than the podded engine. This leads to $P_{BLI} < P_{podded}$, because less power needs to be added to a flow that enters the engine with a lower velocity. In other words, less power is required to achieve the same thrust, which means less fuel burn and so fewer emissions.

This kind of representation has been used in internal force control volumes that typically use thrust and drag accounting systems similar to the uninstalled performance calculations for conventional podded engines. However, BLI systems are inherently integrated and must include aspects of the aircraft configuration to represent performance sufficiently. The integration factor in a BLI system is considered to be a vital part of the system simulation.

A more in-depth representation of an aircraft with boundary layer ingestion can be performed based on the energy of the system, as shown by Drela [13], in his "Power and Balance Method". More recently, this has been expanded upon with an exergy approach by Arntz et al. [14]. Representations of the energy of the combined aircraft and propulsion system avoid the challenge of thrust and drag definitions in an integrated system. However, they are complex methods that move away from the conventional force representations used in propulsion system models. Besides, the energy methods rely on knowledge of the configuration as a whole by the use of a control volume that encompasses the whole aircraft.

2.3.2 Ingested Drag of a BLI System

First, to discuss the drag involved in a BLI system, it is highly useful to give a proper mention of what thrust consists. Especially in integrated architectures such as the BLI, there is a strong interaction between the propulsion system and the airframe so that it becomes more difficult to define the net thrust produced by a propulsion system. Indeed, in steady level flight, this net thrust parameter should be high enough to balance the drag of the combined fuselage and installed engine.

Therefore, to calculate it, it is necessary to account for both the momentum drag of the system and the gross thrust that is defined as:

$$F_g = \dot{m}u + A(p - p_0) \quad (2.20)$$

Such a definition of thrust can be evaluated independently of flight conditions and is ideal for uninstalled thrust tests of an engine. [15]

In a podded engine, thrust is typically quoted as a standard net thrust term (F_N), namely the difference between the gross thrust at the nozzle exit (F_{G9}) and the gross thrust far upstream (F_{G0}).

However, in an integrated system the installation terms are also linked to the performance, the propulsion system is better represented by a Net Propulsive Force (NPF).

This term typically includes the force terms associated with the engine cowl and after body, spillage drag, and interference drag. NPF can be defined as in the equation below, where $\phi_{nacelle}$ is the nacelle force, (F_{G9}) is the gross exit thrust, and (F_{G1}) is the force that acts on the inlet. [15]

$$NPF = F_{G9} - F_{G1} - \phi_{nacelle} \quad (2.21)$$

Because of the intrinsic interaction between the propulsion system and the airframe, in a boundary layer ingesting system, the portion of the airframe profile drag that enters the propulsion system inlet must be accounted for in the propulsion system. At off-design conditions or for inlet mass flow ratios not equal to unity, the engine suction may accelerate or decelerate flow into the inlet. This would result in changes in the skin friction drag directly before the inlet as a function of the propulsion system performance. For this reason, as shown in Figure 2.8, a suitable interface point i can be chosen, approximately twice the inlet height ahead of the engine highlight plane [9] [16], in order to adequately split the aircraft and propulsion system thrust and drag accounting.

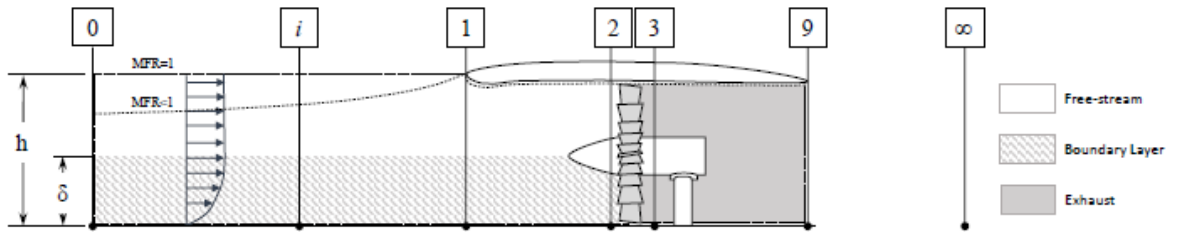


FIGURE 2.8: Propulsion system control volume and station definition [9]

This interface should approximately indicate the region where engine thrust and drag is no longer a function of the aircraft condition, and vice versa.

According to this station definition, the net propulsive force of the propulsion system becomes:

$$NPF = F_{G9} - F_{Gi} - \tau_w S_{wet} - D_{nacelle} \quad (2.22)$$

Where $\tau_w S_{wet}$ represents the skin friction drag from the wetted surface area between stations i and the inlet highlight (1).

The value of $\tau_w S_{wet}$ accounts for only a small proportion of the total drag of the aircraft because this portion of drag is now accounted for in the propulsion system and must be separated from the calculated aircraft drag.

Therefore, the drag of the airframe may be split into two components: the ingested drag, $D_{ingested}$, and the uningested drag of the airframe, $D_{aircraft}$ the sum of which

may be represented by the total aircraft drag, $D_{totaldrag}$.

$$D_{aircraft, clean} = D_{ingested} + D_{aircraft} = NPF \quad (2.23)$$

In steady level flight, the propulsion system is required to produce only enough net thrust to counteract the drag not recovered by wake re-energization, $D_{aircraft}$, rather than the entire drag of the clean aircraft. However, the net propulsive force is required to counteract the entire system drag. This definition highlights that the thrust (F_N) requirement of a BLI system is a value dependant on its configuration and location, despite a constant NPF.

Plas [9] references a method for calculation of the drag recovered by wake re-energization, $D_{ingested}$, based on the use of boundary layer characteristics at the interface point and the average boundary layer shape factor, between the interface point (i) and the wake (∞).

Assuming that the airframe drag remains constant, drag recovered by the propulsion system reduces the required thrust output in comparison to an equivalent propulsion system in free-stream flow. At first glance, an engine which ingests only free-stream flow can, therefore, appear a better option than a BLI engine, as F_N is greater. However, accounting for the ingested drag on the engine side of the NPF equation balances out this difference. In steady level flight, this means that the propulsion system NPF should be equal to the drag of the clean aircraft, $D_{aircraft, clean}$, the drag of the airframe excluding the propulsion system.

$$D_{aircraftclean} = NPF = F_{G9} - F_{Gi} - \tau_w S_{wet} - D_{nacelle} + D_{ingested} \quad (2.24)$$

The BLI system is therefore sized to achieve the NPF required by the aircraft design. Using this definition of NPF, both a propulsion system in free-stream flow and a BLI propulsion system would be required to produce the same net propulsive force on the same aircraft configuration.

2.3.3 Efficiency and Power Saving Coefficient

Evaluations of the efficiency are a requirement for the assessment of a propulsion system. For a BLI system, in particular, the performance relative to a conventional propulsion system must increase sufficiently to justify the adoption of the technology. However, proper definitions of efficiency are required to derive the efficiency of a BLI system. Propulsive efficiency ($\mu_{propulsive}$) contributes to the overall efficiency parameter of a conventional propulsion system. In the standard form used in propulsion system performance, propulsive efficiency quantifies the useful propulsive power output as a percentage of the power available from the free-stream flow. For a conventional propulsion system, this can be calculated using the following formula [12]:

$$\eta_{propulsive} = \frac{2u_{\infty}}{u_{\infty} + u_j} \quad (2.25)$$

This expression points out one of the leading statements of propulsion system design: maximizing the propulsive efficiency requires minimizing the exhaust jet velocity. However, this is related to a reduction in the specific thrust of the propulsion system. In the case of a BLI propulsion system, three velocities define the propulsive efficiency, as the flow entering the propulsion system is not equal to the flow available in the free-stream. These velocities are the velocity of the air entering the inlet, \bar{u}_i , the velocity of the exhaust jet, u_j , and the velocity of the free-stream flow, u_{∞} . The propulsive efficiency of a boundary layer ingesting system, therefore, cannot be defined in the same way as that of a free-stream engine. As the useful propulsive power is in terms of the local inlet stream, the propulsive efficiency of the system is defined relative to these terms [17]:

$$\eta_{propulsive,BL} = \frac{2u_{\infty}}{\bar{u}_i + u_j} \quad (2.26)$$

In the case of a purely wake filling BLI propulsor, the exhaust velocity is equal to the free-stream velocity ($u_j = u_\infty$), the ratio becomes equal to 1, and thus the efficiency is maximum. However, unlike a conventional propulsion system, the velocity at the BLI inlet engine is less than the free-stream ($\bar{u}_i < u_\infty$).

The denominator of the equation is, therefore, less than the numerator and, in this configuration, the propulsive efficiency is greater than 100%. An increase in the momentum deficit leads to further reductions in \bar{u}_i which results in an increase in propulsive efficiency.

Even in a BLI system with a higher exhaust velocity, the propulsive efficiency would be greater than that of an equivalent propulsion system in free-stream flow. This is due to the discrepancy between u_∞ and \bar{u}_i ($\bar{u}_i < u_\infty$) and the fact that, for the same specific thrust, u_j for a BLI propulsion system is lower than that of a propulsion system in free-stream flow.

As the momentum deficit reduces, \bar{u}_i tends to u_∞ and the propulsive efficiency returns to the conventional definition.

Propulsive efficiency is not the only descriptor of performance and efficiency. High propulsive efficiency in a BLI system may result from a thick boundary layer with a high momentum deficit. However, this may be affected by distortion and related issues elsewhere that are detrimental to the overall system performance. The performance benefit of a BLI system can instead be represented in terms of a power saving coefficient, as proposed by Smith [18]. This enables the assessment of the benefits of the propulsion system as a whole relative to a comparable system in free-stream flow.

$$PSC = \frac{P_{podded} - P_{BLI}}{P_{podded}} \quad (2.27)$$

Where P_{podded} indicates the power consumption of a podded propulsion system, operating in free-stream flow, required to propel an aircraft with drag $D_{aircraft, clean}$. P_{BLI} indicates the power consumption of a BLI propulsion system required to propel the same aircraft.

The benefit is thus the difference in power required to produce a given net stream-wise force. A positive power saving coefficient represents a BLI system with power consumption that is lower than that of a free-stream propulsion system. The power saving coefficient representation of efficiency includes any losses within the system and can show the changes of a BLI system relative to an equivalent free-stream model. Smith found that in some cases that the PSC for the propulsion system could be in the region of 7% for the configurations considered [18]. Plas notes that the power saving coefficient decreases as system losses increase, and this can cancel out the benefit of a BLI system.

The PSC parameter is used to assess the impact that a BLI configuration has on the system as a whole. A system with a PSC less than zero may be deduced to be unfeasible, as a free-stream propulsion system would be a more efficient option.

2.4 BLI Benefits Analysis

The following section attempts to summary differences between podded and embedded engines as well as to highlight the advantages and disadvantages of the two engine installation types. The principal difference between them deals with the position of the installation on the aircraft. Whereas the podded engines are installed out of the fuselage and beneath the wings, making BLI unachievable, the embedded engines are integrated into the aircraft and positioned at the rear of the fuselage.

Thanks to this semi-buried configuration, their frontal area is limited, enabling to reduce the overall aircraft drag and allowing to ingest part of the boundary layer of the upper surface of the fuselage. This offers one of the essential advantages of integrating engines because it disrupts the formation of the wake, contributing to airframe drag, allowing the wetted area to be reduced, helping to attain minimal drag and hence, lowering the power requirement.

Actually, it can be asserted that a key factor in the efficiency benefit of a BLI system is the reduction in airframe drag due to the re-energization of the wake.

Ingesting a boundary layer flow means ingesting a low energy flow, and so a low-velocity flow.

Figure 2.9 shows a comparison between BLI and non-BLI configuration in terms of mass flow and efficiency. With the same mass flow rate, a BLI propulsion system would require around 6% less power while at the same power requirement, there is a 23% mass flow reduction.

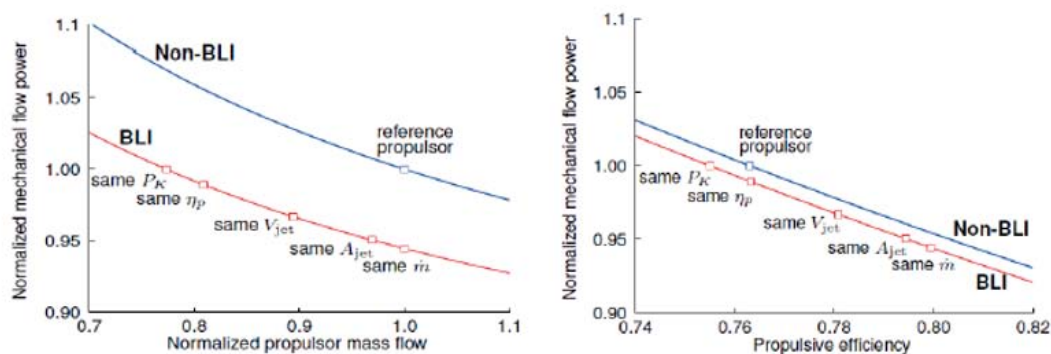


FIGURE 2.9: Comparison of BLI and Non-BLI in Mass Flow and Efficiency [19]

Another considerable advantage deals with the fact that the excess weight carried by the podded engines from structural supports such as pylons is no more required with BLI engines contributing to a relative reduction of weight. Moreover, embedded engines produce a thrust line closer to the aircraft centreline, avoiding a nose-down pitching moment, typically usual in the podded ones, thus diminishing the trim problems along with control surface size and power requirements [20]. The other important benefit of the embedded engine is the potential ability to reduce the overall noise of the aircraft. Since the engine is embedded, the airframe acts as a shield suppressing the intensity of the noise towards the ground.[21]

At first glance, from Figure 2.9, it can be deduced that BLI engines have higher efficiency compared to the podded engines with the same mass flow rate.[19]

However, in the propulsion system, an ingested turbulent boundary layer can give rise to total pressure loss and swirl non-uniformities at the engine face (AIP), which can have a negative impact on the performance of the engine and in the operability problems. The boundary layer may separate causing distortion and altering the engine efficiency.

It can potentially lead to additional vibration resulting in noise, cause structural damages and operational issues of the engine. The podded design has an advantage of the ease of maintenance, as embedded designs are much more restricted.

Looking at the AIP, the following Figure 2.10 shows how the air Mach number evolves from free-stream to AIP, where the range of Mach number should be approximately around 0.6-0.7.

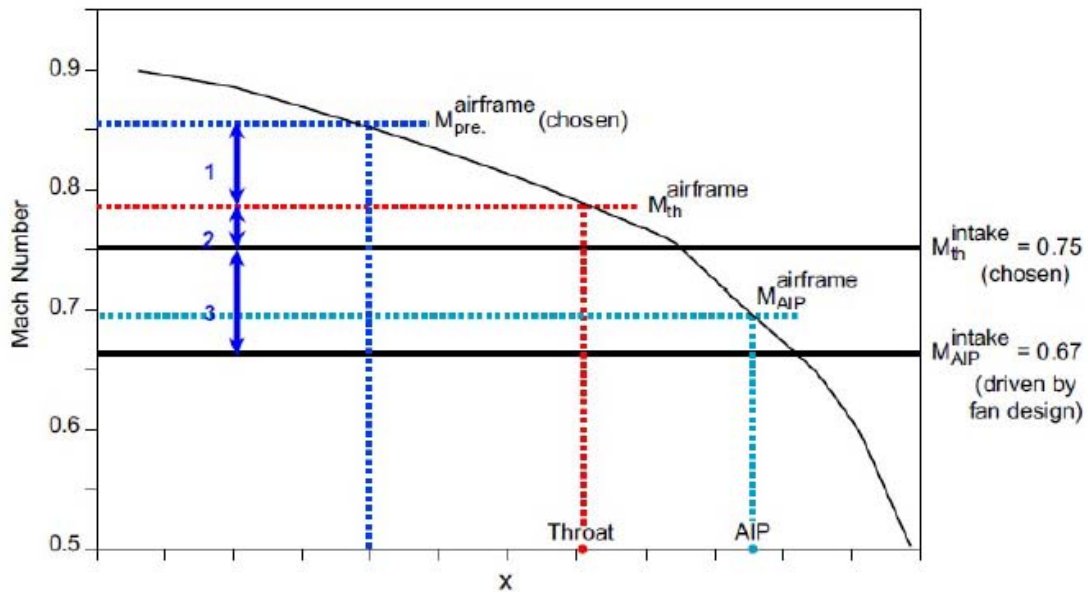


FIGURE 2.10: Evolution of Mach number from free stream to AIP, 1=diffusion by the airframe, 2=diffusion by the pre compression zone, 3=diffusion by the inlet duct [9]

Previews works conducted on this concept give a lot of relevant results based on test data that showed these opposite trends existing with BLI.

For instance, one of the first BL controlled flow investigations on a standard aircraft configuration performed by Smith [22] in the mid-1940s, assessed up to a 5 to 10% of reduction in fuel consumption at cruise for engines provided with boundary layer ingestion. The experiment provided a comparative study of three engine configurations: turboprop engine, turbojet engine with direct ramming inlets and turbojet engine with boundary layer inlets. Assuming no losses in the inlet, lots of BLI benefits occurred in the third configuration of respect to others; indeed, a 16% maximum propulsive efficiency improvement was calculated.

So how a better control parameter was verified thus aircrafts needed shorter runway length, produced higher maximum speed and cruising economy of 32% greater than that of the standard turbojet engine propelling the same airframe.

On the other side, in the presence of inlet losses (real condition) the Brayton cycle efficiency, which depends on many engine parameters or air properties, such as the overall pressure ratio, compression efficiency, temperature ratio, turbine efficiency and specific heat ratio, was reduced by 6.1% to 21%.[\[23\]](#) Therefore, it has been proved that two main conflicting behaviours can take place: an increase in propulsive efficiency and a decrease in cycle efficiency. Since fuel consumption is the product of the propulsive and cycle efficiency, the overall efficiency can rise or fall in boundary layer suction.

Therefore, although the embedded engine proposes many advantages, it occurs various complications. Using the embedded configuration for BLI is one of the most intensely researched fields which still matter of in-depth studies. Even with years of research, it is still an unproven technology. This shows the level of difficulty and risk associated with the complexity in the design of the airframe and of the engine that now becomes much more coupled. Table 2.1 presents a summary of the advantages and disadvantages of podded and embedded configurations.

	ADVANTAGES	DRAWBACKS
Podded Engine	<ul style="list-style-type: none"> ·Ease of maintenance ·Proved technology ·Uniformity of flow 	<ul style="list-style-type: none"> ·High weight for structural components such as pylons and nacelle ·Nose pitch moment ·Large amount of drag due to a large wetted area
Embedded Engine	<ul style="list-style-type: none"> ·Reduction in specific fuel consumption (SFC) ·Lower wetted area, so lower drag ·Noise reduction ·No structural weight added (no pylons) ·Mitigation of the nose pitch moment, lower thrust line 	<ul style="list-style-type: none"> ·Pressure loss ·Boundary layer separation ·Distortion at AIP ·Non-uniformity of flow ·Additional vibration ·Possibility of lower efficiency ·Unproven technology

TABLE 2.1: Comparison of advantages and drawbacks for podded and embedded engines

2.4.1 BLI Literature Review

This section consists of a brief investigation of several BLI concepts that have been analyzed by NASA, Boeing, Bauhaus-Luftfahrt, ONERA, and more in the later years. Even though the idea of ingesting BL has been examined for several years to improve propulsion systems and aircraft performance, the BLI system is still an unproven technology, and there is no commercial airliner with a functional BLI system on-board. Moreover, previous CFD studies are described in order to introduce the main achievements reached so far when applying simulations into designing and assessing a BLI concept. The idea of this part consists of the introduction of some of the most auspicious concepts that have been developed in the later years, finding improvements in TSFC of up to 18% and that might be taking off in the 2035 timeframe.

2.4.2 STARC-ABL Project

The “Single-aisle Turboelectric AiRCraft with Aft Boundary Layer” concept is a conventional single-aisle tube-wing configuration with a hybrid-electric propulsion system. In essence, two underwings mounted turbofan engines and an electrically driven BLI tail-cone propulsor, as shown in Figure 2.11.



FIGURE 2.11: STARC-ABL Concept [24]

This concept is based upon the Refined SUGAR concept developed by Boeing [25], an advanced technology airliner with capacity for 154 passengers in a two-class seating arrangement and cruise speed of Mach 0.7. The entry into services (EIS) of this concept is the 2035 timeframe assuming and implementing numerous technologies to improve the performance, reduce the overall weight of the aircraft and fulfil emissions and noise requirements [26]; [27]; [28].

This concept was deeply investigated in the second phase of the SUGAR project (code-name “N+4”), introducing cryogenically stored liquefied natural gas (LNG), hence “Freeze” for the main engines and implementing an electric aft-thrusters in the rear back of the fuselage [26]. A technology development plan is also included for the BLI propulsion system taking into account the difficulties of its technology such as total pressure drop due to the reduced velocity in the boundary layer and distorted flow, especially on engines placed over planer surfaces.

The latest version of the STARC-ABL aircraft integrates both concepts the SUGAR Volt and SUGAR Freeze, with resized turbofan engines considering a fan pressure ratio (FPR) of 1.30 (decreased from 1.45 in the Revision A), a design Mach number of 0.785 (up from 0.7 in the original version).

In contrast, the BLI propulsor will be running with a fixed input of 3500 HP, a fan pressure ratio (FPR) of 1.25 with an adiabatic efficiency of 95.6%.

The power for the after-prop is generated by electric generators allocated in the main engines accounting for 2000 HP (1.4MW) each turbofan. It is expecting that at low altitudes and speeds, the power would be generated by the main engines (around 80% of the thrust during the take-off phase), whereas during cruise condition, the aft-prop is designed to provide 1/3 of the total thrust. One crucial parameter is the location of the aft-fan over the axial location since the flow conditions are varying along the fuselage. For the STARC-ABL, the after propulsor is mounted around 97% of the fuselage length, and it is designed to capture 45% of the total boundary layer height. This would allow capturing 70% of the total momentum deficit [27], which is defined as the optimum amount of fraction to be ingested, since capturing the entire boundary layer would increase the size of the fan and require considerably more power, increasing weight and losses in the electrical system. It is reported that the STARC-ABL will generate significant reductions in terms of fuel burn, around 7% in block fuel burn for the economic mission, and 12% for the design mission comparing with a conventional configuration. [27]

2.4.3 DisPURSAL Project: (PF) Propulsive Fuselage

The idea of a Propulsive Fuselage (PF) was first designed within the “Distributed Propulsion and Ultra-high By-Pass Rotor Study at Aircraft Level” (DisPURSAL) project, a 2-year research project coordinated by Bauhaus Luftfahrt in partnership with CIAM, ONERA and Airbus Group Innovations [29],[30]. The main concept of the PF consists of an after-propulsor on the fuselage assessed under specific criteria such power system integration, noise, weight, operability (technical and non-technical) and efficiency, and for several configurations well illustrated in Figure 2.12 [31]:







Concept	Name and Description
	Aft-mounted fans covering the upper part of a cylindrical fuselage (REVOLVE)
	BWB with embedded fans on top of the lifting body trailing edge (BWB)
	Tube and wing configuration with fans integrated within a split-wing (SPLIT)
	Tube and wing concept with fans mounted on the upper wing side (WING)
	Cylindrical fuselage with circumferential fan at the aft section (PROPFUS)
	Cross-flow fan embedded into the trailing edge of the wing (CROSS)

FIGURE 2.12: Distributed propulsion concepts with BLI. Adapted from [31]

Based on this assessment, it was shown that the PROPFUS is the most innovative concept about efficiency since distortion and pressure losses might be lower than with the other concepts. Moreover, it was assumed that the aft-fan would be ingesting around 80% of the fuselage viscous drag, improving the overall efficiency of the propulsion system (smaller propulsor size, lower weight and drag). On the other hand, this concept presents a high number of drawbacks, mainly for operability and power system integration, due to its structural constraints for tail-strike, high impact of propulsor failure and foreign object damage.

The DisPURSAL project considered a wide-body aircraft similar to an Airbus A330-300 as the baseline airliner. Thus, the PF concept is supposed to have a range of around 4800 nm flying with a payload of 340 passengers.

Initially, the circumferential fan was allocated at 75% of the fuselage length, but after parametric studies, it was installed at 85% in the final configuration, with a cruise Mach number of 0.8 and an inlet duct height of 0.58 m expecting to produce a 9.2% block fuel reduction.[32][33]

For the PF concept, many tail boom arrangements were considered before selecting a T-tail configuration, avoiding additional issues due to landing gear integration while ensuring minimum flow distortion at the inlet. However, other aspects to consider are the thermo-structural integration of the propulsion system and tail-loads transmission. Nevertheless, final results published by Bijewitz, Seitz and Hornung [33] estimate a block fuel reduction of 12.1% for a similar but optimized concept targeting a POS +2035, with optimized underwing engines and under a thrust split ratio condition.

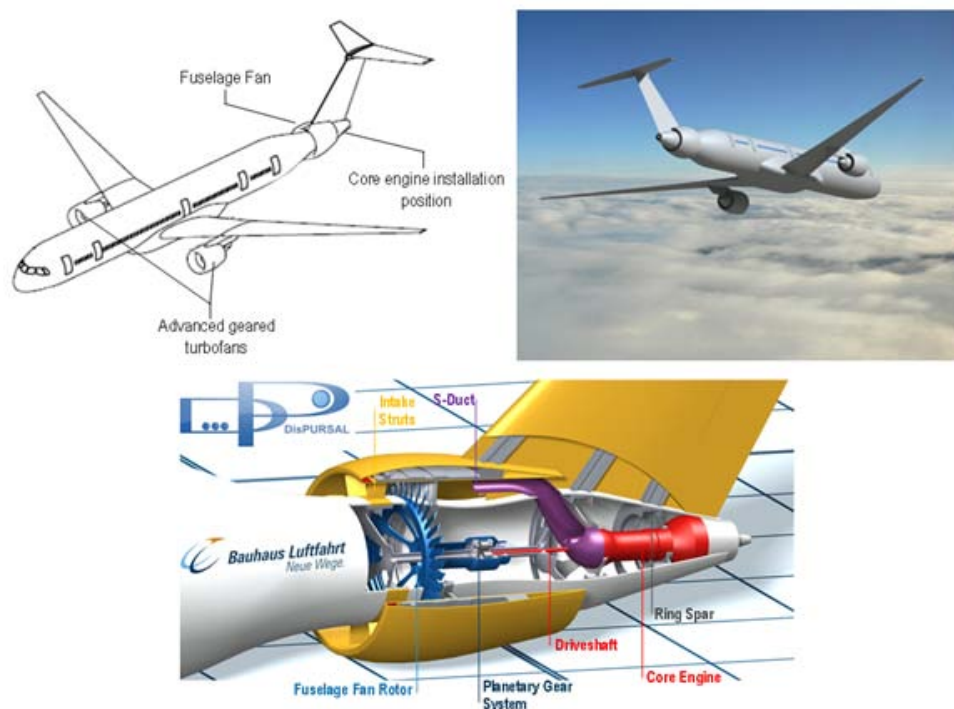


FIGURE 2.13: Propulsive Fuselage concept (up) and main components of after fan (down) [34]

2.4.4 D8-Double Bubble Concept

Another futuristic concept known as the D8 Series or "double bubble" shown in Figure 2.14 was introduced as part of the NASA N+3 Phase 1 project "Aircraft and Technology Concepts for an N+3 Subsonic Transport".



FIGURE 2.14: D8 Double Bubble concept developed within NASA N+3 project [35]

The D8 series satisfies three of the four objectives defined as intended goals: fuel burn reduction (a 70.87% reduction, slightly above the 70% initially defined), LTO NO_x below CAEP 6 (an 87.3% reduction, surprising the > 75% reduction aimed with the project) and a field length of 5000 ft (well below the 7680 ft required for the baseline aircraft) [36]. The final concept was the result of a team effort between MIT, Aerodyne Research, Aurora Flight Sciences, and Pratt and Whitney.

The D8 Series has been designed by applying a new methodology referred to as TASOPT where the effects of the embedded engines and BLI technology were taken into account. In the latest version of the D8 concept, it has been proved that the propulsion system is capable of ingesting around 40% of the BL during the cruise phase [37]. Undoubtedly, this concept has received much attention due to its unique configuration and capabilities. Its evolution is shown in Figure 2.15 where the introduction of the BLI propulsion concept generates a decrement of 15% in fuel burn.

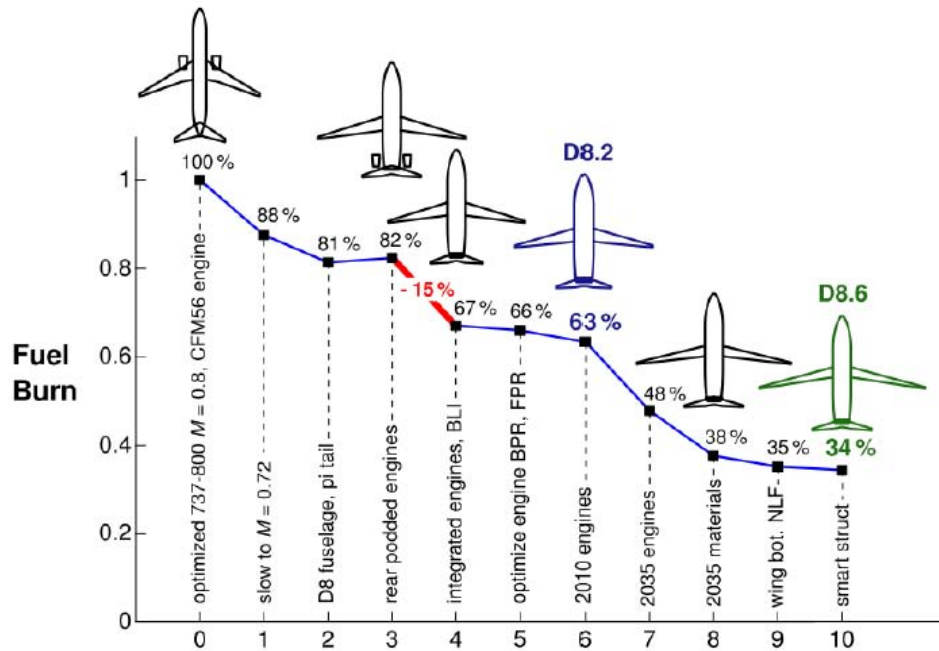


FIGURE 2.15: Evolution of the D8-series concept [26]

2.4.5 BWB Concept

The Blended Wing Body concept (*BWB*) is one of the futuristic BLI configurations firstly conducted by Boeing Phantom Works. The project aimed to evaluate the benefits of BLI inlets with active flow control (*AFC*) on a BWB by assessing different configurations of embedded engines and varying the nacelle aspect ratio and orientation concerning the airflow. Similarly, within the NASA N+3 Phase 1 project, a novel concept presented in Figure 2.16 was developed with the codename H3 Series. Within this new configuration, the BL to be ingested is estimated at around 30%, while the distortion levels may be higher than for the D8 series. On the other hand, the embedded aft-engines are less susceptible to bird strikes due to their location, whereas the noise parameters could be reduced.



FIGURE 2.16: Conceptual design for BWB H3.4 configuration [36]

Likewise, in the DisPURSAL project, a BWB configuration with a distributed multiple-fans concept (*DMFC*) was designed in order to develop a model capable of replacing the current A330-300 aircraft. Initial studies estimate a block fuel reduction around -7.8% for the DMFC. [33]

2.4.6 A17-Zephyr

Students of the MSc. Aerospace Vehicle Design from the University of Cranfield carried out a study as part of the Group Design Project of a short to mid-range airliner designed and named as A-17 Zephyr. Lots of advanced technologies were included in this concept; one of them is an after-prop BLI capable of producing one-third of the thrust at cruise condition. [38]

In Figure 2.17, the aft-prop is illustrated in his final configuration.



FIGURE 2.17: A-17 tail view with BLI aft-prop [39]

For the after-fan, the "average flow method" [40] was used to estimate the initial flow conditions for the design of the after propulsor. After modelling the inlet flow conditions, gas turbine theory was applied in order to go on with the design of the traditional propulsor keeping the flow conditions calculated before. At cruise conditions, the BLI fan is supposed to run at 2500 RPM while generating 10kN of thrust.[39]

It is worthy of mentioning that this fan was designed based on parametric studies, but the overall benefits produced by the BLI over the A-17 Zephyr aircraft are still unknown.

2.5 BLI Inlet Modelling

2.5.1 Intake and S-duct Design

The primary purpose of a subsonic intake is to perform as a diffuser and allow the internal airflow to reach the engine face with minimum distortion and with minimum total pressure losses as the engine performance relies on the quality of the incoming flow.

The integration of the engine and the airframe is indeed very important as it powerfully influences the aircraft performances. Developing the design of an inlet requires to take into account several characteristics that can be critical or even detrimental to the inlet performance.

The main parameters and specifications that must be considered properly deal with the distortion at the fan face and the pressure recovery, as well as a low drag, noise and weight requirement. Improving one of these characteristics, however, can be negative to one other, resulting in loss of efficiency of the whole system. A careful assessment of the relationships of the parameters is necessary to choose the best trade-off. The principal inlet variables can be summarized as:

- drag at cruise
- inlet total pressure ratio (pressure recovery)
- position of the engine (beneath the wing or on the fuselage)
- distortion levels required by the engine
- flow field interaction with the nacelle or the wing
- noise requirements

Figure 2.18 illustrates a typical intake of a podded engine with the definitions of the design parameters.

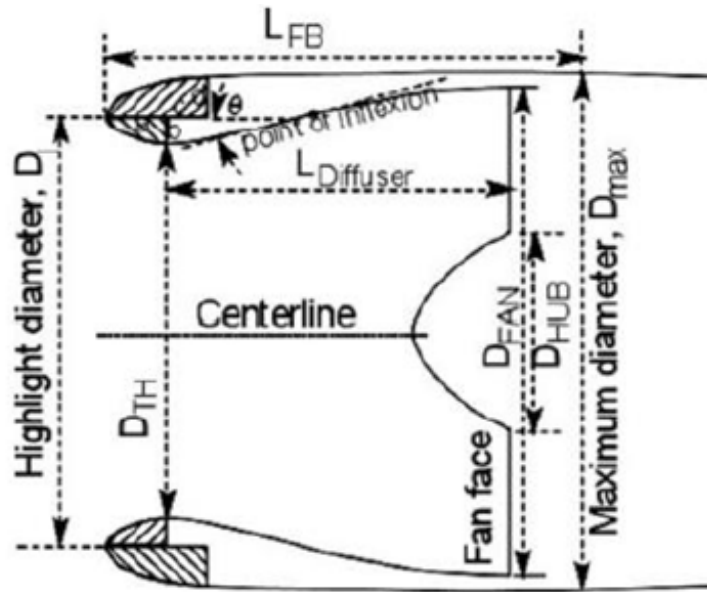


FIGURE 2.18: Schematic diagram of a nacelle profile [41]

For the case of an intake design for an embedded configuration, Figure 2.19 represents the design parameters for the BLI intake model with an S-shaped duct that could be a viable solution even in the civil aircraft due to its already existing use in air-intake systems for several military aircraft. This inlet offset highlights the strong difference respect to the podded engine, and hence other important parameters that require to be defined.

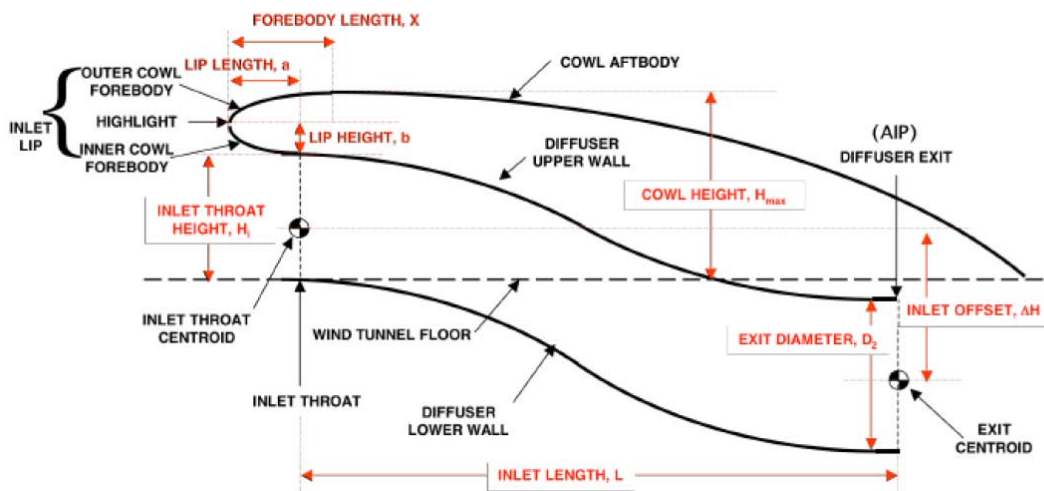


FIGURE 2.19: Side-view diagram of a inlet design parameters for BLI [42]

A good design duct is desired to guide the captured flow to the engine with minimal losses. The above figure illustrates a simple S-duct diffuser for an embedded propulsion system. One of the challenges of BLI propulsion deals with this added curvature that is susceptible to an adverse pressure gradient, which results in a region of flow separation. To achieve maximum engine performance, the S-duct should be designed to minimize total pressure losses within the duct and minimize total pressure distortion to prevent engine stall. Therefore, it is of great importance to design an S-duct that ensures high-pressure recovery (PR) and efficiently decelerates the incoming flow for different operating conditions.

However, all these requirements need to be satisfied simultaneously with size and weight restriction that induce the use of shorter duct, leading to greater streamline curvature and adverse pressure gradients that consequently cause secondary flows. The two primary sources of total pressure losses consist of skin friction drag and a non-axial flow velocity component caused by vortices and, as described in previous works, the first bend of the duct could be the primary origin of such detriment. [43]

The radius of curvature of the bend is furthermore an important parameter that can affect the arise of flow separation. A bend with a low radius of curvature (Figure 2.20) has a greater inclination compare to a bend with a high radius of curvature (Figure 2.21).

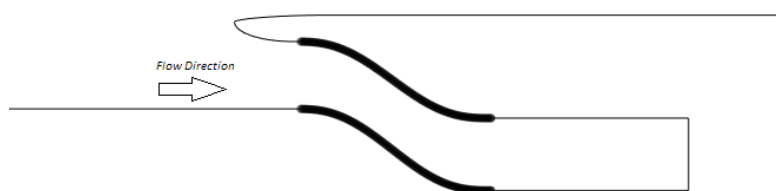


FIGURE 2.20: Scheme of bends with a low radius of curvature



FIGURE 2.21: Scheme of bends with a high radius of curvature

So increasing the radius of curvature can border flow separation, while pressure recovery is largely increased at fan-face as well as the length of the duct. Thus a choice has to be made regarding which parameter is predominant depending on the requirements.

In this study, as a design choice, the radius of curvature is given by the difference of the average heights of the inlet and outlet of the duct. This geometrical parameter will be explained in the next Chapter 4.

On the other hand, swirl occurs due to the duct curvature independently from the bend itself. It is the result of the interaction between low energy regions (associated with flow separation) and centrifugal pressure gradients. [44] A way to prevent swirl would be to ensure enough distance from each bends in order to avoid that flow separation, caused by the first bend, can reach and affect also the second bend. In the case of a diffuser duct, a flow deceleration is expected from the inlet to the engine face through a divergent duct. Indeed, most of the compressors are design to operate with the flow at around a Mach number of 0.4-0.7. Whereas the engine design fixes the area at AIP, the area at the throat and highlight is fixed by the designer. This reduction in flow velocity induces a rise in static pressure that impacts on the boundary layer behaviour. Local separation may occur at some points when the growth of pressure gradients, resulting from the divergence of the duct, becomes more significant than what is required to keep the boundary layer attached to the surface. Therefore, if the diffuser wall diverges rapidly, meaning a high increase in cross-sectional area, the flow will completely separate and behave more like a jet, as shown in the following Figure 2.22.

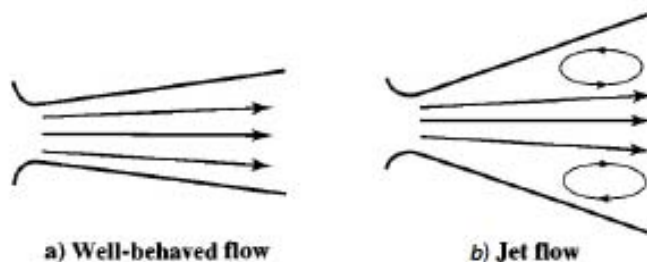


FIGURE 2.22: Flow Separation

In this thesis, the study is conducted on a BLI intake characterized by a smooth S-shaped duct. The highlight area is designed equally to the outlet area to prevent flow to separate. The nacelle consists of a rigid body whose structure is aligned parallel to the fuselage. Thus, a focus is given to the frontal area of the intake, the lip design and its thickness. The behaviour of the internal flow is studied until the fan interface rather than the after body nacelle design.

2.5.2 Lip Design

The very first component directly in contact with the airflow is the lip of the intake which allows splitting the air stream into an internal flow and an external flow while ingesting a certain amount of free stream. Intake lip design is critical to ensure airflow stability through a gas turbine engine or a duct. The internal flow feeds the engine, whereas the external flow influences the aerodynamic of the engine frame.

Lip design is a relevant feature as well as the intake design itself in order to ingest the incoming flow with minimum possible losses. Indeed, the lip shape is what influences the most the total lip pressure loss. Different lip shapes can be taken into account, and the following figure shows pressure recovery (Lip ratio) as a function of flow ratio at different free-stream Mach numbers for a sharp-lipped entry (contraction ratio $A_0/A_1 \sim 1.0$) and for an elliptic lip profile.

It shows that with a sharp lip, the loss increases rapidly once the flow ratio exceeds 1.0, whereas with an elliptic lip, the loss at a given M_t , throat Mach number, greater than about 0.6, is approximately constant with flow ratio up to $A_0/A_1 \sim 2$. The implications are that in the former case the flow separates from the inside of the lip as soon as the stagnation point passes to the outside, while in the latter case attached flow is possible for a range of flow ratio, in this instance from 1.0 to 2.0, before separation occurs.[45]

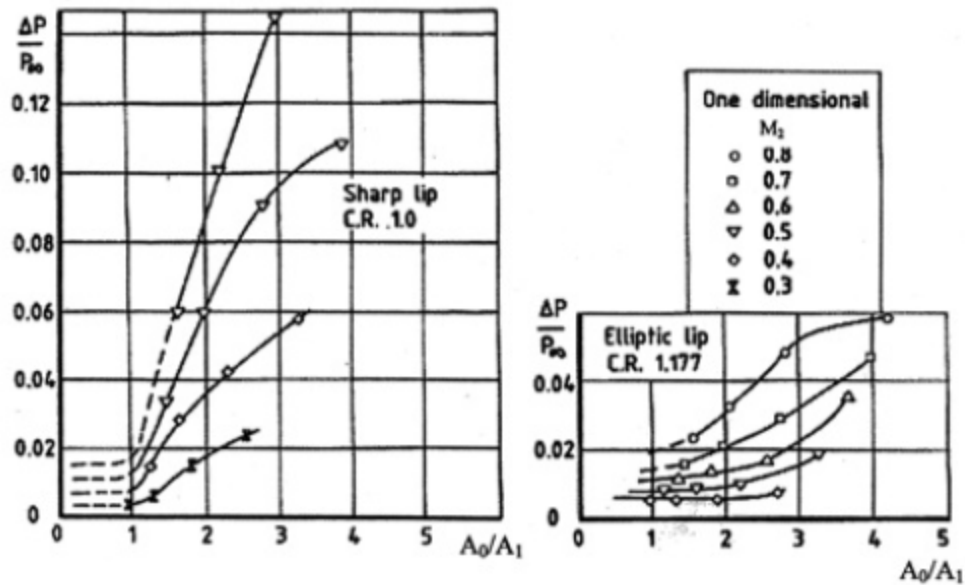


FIGURE 2.23: Influence of throat Mach number and capture flow ratio on total pressure losses [45]

Better performance are expected for the elliptical lip rather than for the sharp lip relative to high subsonic flow.

In Figure 2.24, the inlet lip contraction ratio A_{hlip}/A_{throat} is illustrated as function of the inlet lip Mach number for an average throat Mach number of 0.75. A large inlet lip contraction ratio contributes to a parameter known as the lip "bluntness", which is good for low-speed and high-angle-of-attack, and is bad for the drag divergence characteristics of the nacelle at high speed. A low contraction ratio inlet lip offers a good high-speed characteristic for the nacelle external drag and a poor low-speed characteristic toward the engine face and flow distortion.[1]

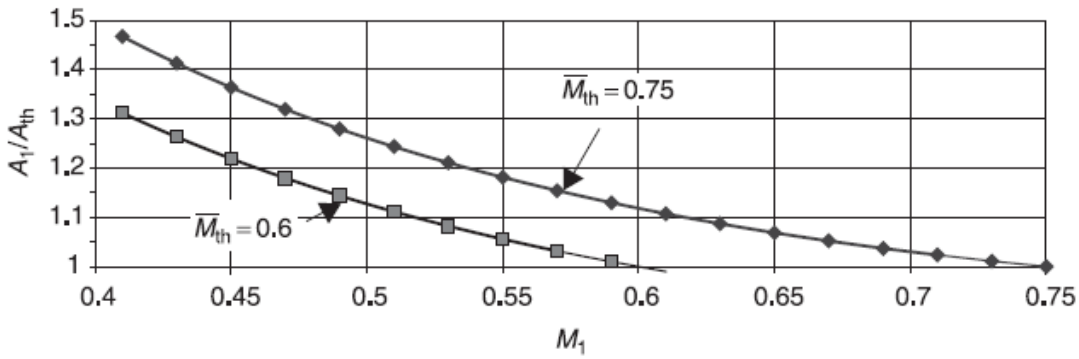


FIGURE 2.24: Inlet lip Mach number variation with the lip contraction ratio and throat Mach number [1]

In order to develop an elliptic lip design, some parameters need to be defined starting from:

- a semi-major axis of the internal lip
- b semi-minor axis of the internal lip

In most cases, the lower lip is developed by the engine manufacturer and usually matches the upper lip. With this assumption, the lip follows an elliptical shape, as shown in Figure 2.23.

In this study, however, in addition to an elliptical lip another type of lip is taken into account: the internal lip follows the elliptic geometry, while a NACA cowl profile gives the external lip.

Two other important parameters regarding the lip design are the following:

- Aspect Ratio:

$$AR = \frac{a}{b} \quad (2.28)$$

- Contraction Ratio:

$$CR = \frac{A_{highlight}}{A_{throat}} \quad (2.29)$$

The CR represents the area ratio between the highlight and the throat of the intake, as shown in Figure 2.19.

This parameter controls the lip thickness, while the AR defines the length of the lip based on a fraction of its thickness. It is suggested from [41], that the CR typically ranges from 1.05 to 1.20, where CR close to 1.0 represents a sharp lip and 1.2 characterizes a well-rounded lip.

2.5.3 Inlet Pressure Recovery

Inlet total pressure recovery is one of the most important criteria to define how efficiently the intake provides the air from ambient static pressure to the fan at AIP. It is a measure of how efficiently the kinetic energy of the intake flow is converted into pressure energy, and it is defined as the ratio of the total pressure at the AIP to the total pressure at upstream infinity.

$$IPR = \frac{P_{02}}{P_{01}} \quad (2.30)$$

The equation refers to the stations illustrated in the following Figure 2.25.

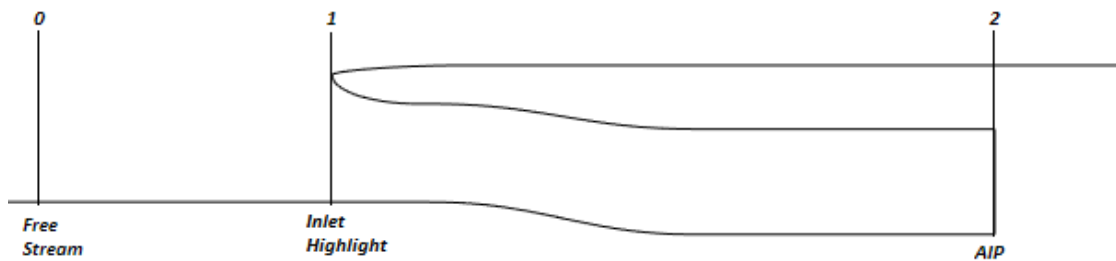


FIGURE 2.25: S-duct stations

From its mathematical definition, the IPR (Inlet Pressure Recovery) is clear to describe the losses in the total pressure. Even though the velocity constancy means a pressure recovery ratio next to unity, it is, however, impossible to reach 100% of intake efficiency. This means that there will always be a loss in total pressure that can occur in any of three ways:

- by friction on the walls of the duct and on any external surface which is wetted by flow going into the duct;

- from turbulent mixing, associated with flow separation or near separation;
- in shock waves, typically in supersonic flights.

Since the internal flow is normally being retarded, boundary layers in the duct and on forward surfaces are all subjected to adverse pressure gradients, which is the classical condition for the creation of flow separation and turbulent mixing.[45]

Figure 2.26 illustrates incompressible pressure recovery data of various types of intakes obtained from wind tunnel and flight data. The term S is defined as the wetted surface ahead of the intake and A_c is the intake entry area. It can be noticed that with larger S/A_c , which means larger surface ahead of the intakes, for all types of intakes data available, the total pressure recovery or efficiency tends to decrease. This is related to the characteristic of the boundary layer ingested by the intake.

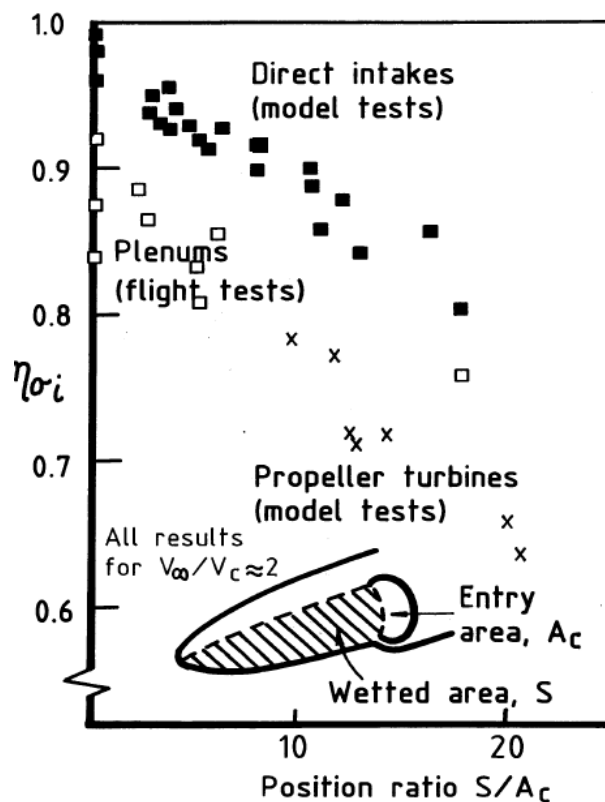


FIGURE 2.26: Collected data on pressure recovery of subsonic intakes [45]

2.5.4 Mass Flow Ratio (MFR)

MFR plays the role of a critical parameter establishing the engine mass flow requirement from the upstream free-stream air.

It can be defined with a relationship between crucial station areas:

$$MFR = \frac{A_0}{A_1} \quad (2.31)$$

where A_0 is the cross-sectional area of the captured stream tube upstream and A_1 is the cross-sectional area of the highlight of the intake. The demand for the engine mass-flow varies with the operating condition shown in Figure 2.27.

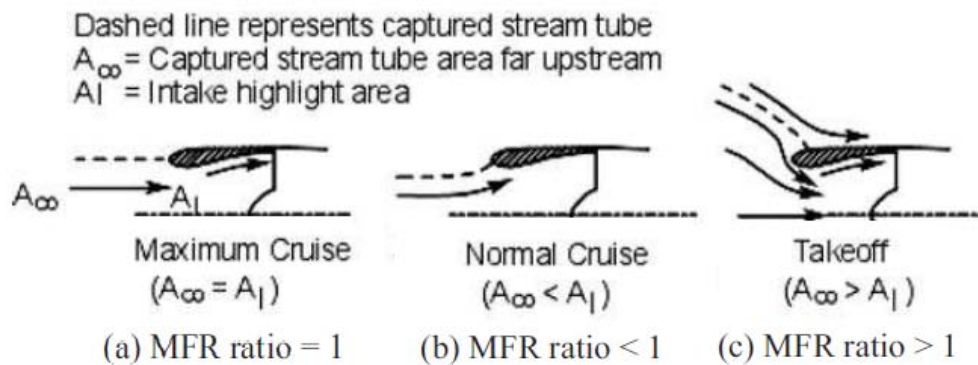


FIGURE 2.27: Airflow demand at various conditions for BLI engine. [Adapted from [41]]

The condition of $MFR=1$ (a), as illustrated in the figure above, relates to a maximum cruise case where the stream tube is cylindrical, and the condition is optimum, hence the velocity remains constant. In this situation, the flow regime is matched as the heights at 0 and 1 points are the same $h_0 = h_1$. Cases (b) and (c) describe typical cruise conditions where the whole efficiency decreases because of a change in the cross-sectional area of the airflow and indeed in the velocity trend which causes the development of a non-axis-symmetrical flow. The $MFR < 1$ condition is prone to a pre-compression zone since $h_0 < h_1$ (diverging stream tube) and thus, the airflow decelerates, leading to a "spillage" condition.

During high-powered flight (take-off condition), instead, the demand of the mass flow is high and requires a $MFR > 1$ as illustrated in (c). At this condition, the stream tube follows a convergent shape since $h_0 > h_1$ causing the airflow to accelerate while creating a decompression zone. This flow regime is said to be in "suction" mode.

2.5.5 CFD and Turbulence Model

Over the decade with the development of powerful computers, the use of numerical tools in engineering has become common. *Computational Fluid Dynamics* (CFD) is a method that helps in the assessment of fluid behaviour within a described flow field by applying numerical models and algorithms. The main reasons why CFD appeals more in comparison to the experimental method are due to being cost-effective and flexible. CFD tools use the Navier-Stokes equation to solve the turbulent flow field.

Three basic approaches can be used to calculate a turbulent flow that practically are called Direct Numerical Simulation (*DNS*), Large Eddy Simulation (*LES*) and Reynolds Averaged Navier-Stokes Equation (*RANS*). *DNS* and *LES* are more computationally expensive compared to *RANS*. *RANS* approach is the most widely used approach for industrial flow, and it deals with solving time-average Navier Stokes equations. It is also capable of accurately solving complex geometries at high Reynolds numbers. The limitation of the *RANS* method arises from the case of naturally unsteady flows where the cell sizes of the mesh are too small to be of similar size a part of the turbulent vortices.

For the case studied in this thesis, the flow is considered to be steady; thus, *RANS* simulation is used.

Firstly, to solve the *RANS* flow equation, the computational domain has to be established for the selected geometry (2D or 3D).

There are different boundary conditions to model the free stream conditions at infinity. The ones that are relevant to this thesis are far-field, wall, and pressure-outlet.

The commercial flow solver used in this thesis is ANSYS Fluent. A practical approach for getting started is choosing the turbulence model, that Fluent offers, which is more suitable for the application considered.

RANS turbulence method offers different models that can be considered for solving a case for turbulent boundary layers are: $k-\varepsilon$ model and $k-\omega$ model.

The drawback of the $k-\varepsilon$ model is that it is insensitive to adverse pressure gradients and boundary layer separation. Therefore, it is not a good selection of the study of external aerodynamics. For the analysis of the turbulent boundary layer in compressible flow at high subsonic speed, $k-\omega$ SST (Shear Stress Transport) turbulence model is suggested.[46]

This kind of model offers similar benefits as standard $k-\omega$ such as superior performance for wall-bounded layer respect to other models, and it is suitable for complex boundary layer flows under adverse pressure gradient and separation. In addition, it provides a more accurate prediction of flow separation than other RANS models.

For this thesis, the choice has been fallen on $k-\omega$ SST precisely because it is preferred where a highly accurate resolution of boundary layers is critical, like in this case.

For CFD, the most important regions making up a turbulent boundary layer are the viscous sub-layer, immediately adjacent to the wall and the log-layer, slightly further away from the wall as it is illustrated in the Figure 2.28 below.[46]

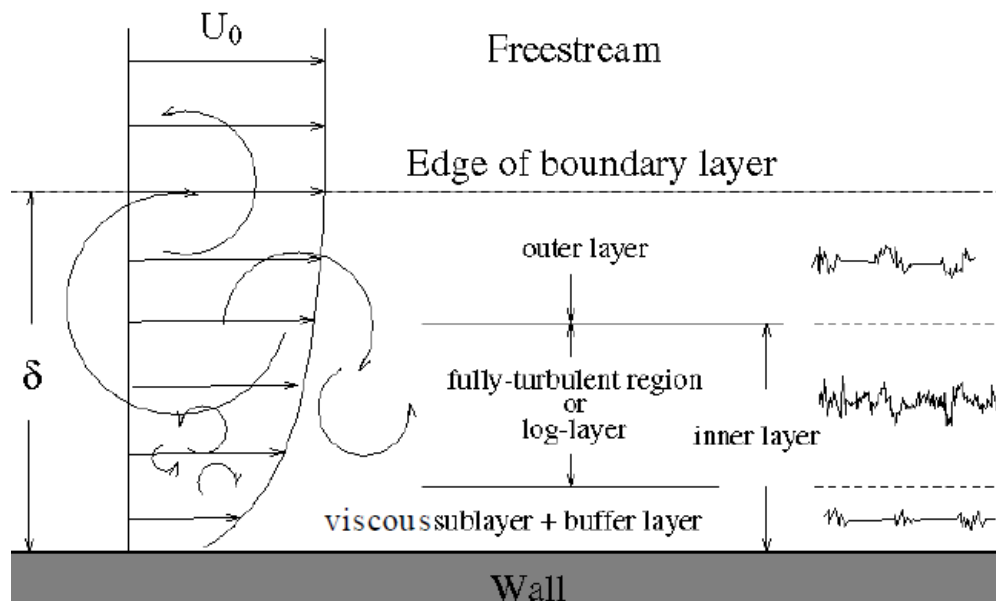


FIGURE 2.28: Turbulent Boundary Layers

By scaling the variables near the wall the velocity becomes dimensionless by dividing U/u_τ where:

$$u_\tau = \sqrt{\frac{\tau_{wall}}{\rho}} \quad (2.32)$$

as well as the wall distance which takes this form:

$$y^+ = \frac{y\tau_{wall}}{\rho\nu} \quad (2.33)$$

The y^+ is defined as a non-dimensional wall distance for a wall-bounded flow and is function of the friction velocity (u_τ), the distance (y) at the nearest wall and of the local kinematic viscosity of the fluid (ν). It is also known as *yplus* and is commonly used in boundary layer theory and to define the law of the wall. [47] Using the non-dimensional velocity and non-dimensional distance from the wall as log scale axes, the shape of the boundary layer results in a predictable form for a wide range of flows where a transitioning from linear in the viscous sub-layer to logarithmic behaviour in the log-layer can be highlighted. Figure 2.29 illustrates the trend of the boundary layer profile on a logarithmic scale.

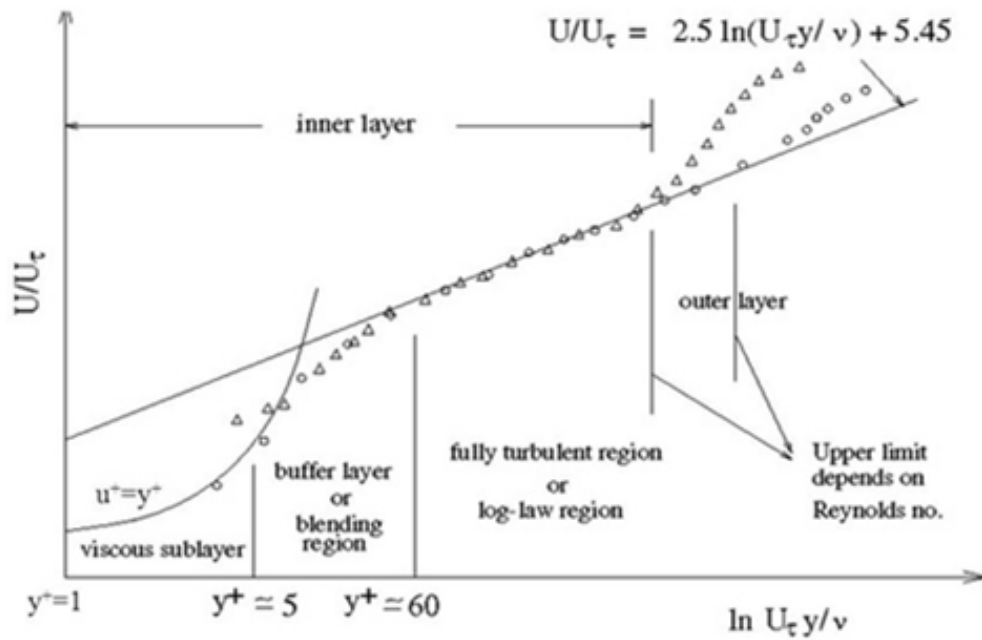


FIGURE 2.29: Different regions in boundary layer

Y^+ changes within the regions: the viscous sub-layer, which is the closest to the wall, can be divided further into a laminar sub-layer where $y^+ < 5$ and the blending region where $5 < y^+ < 30$. The log-law region is at $30 < y^+ < 1000$ and the outer layer at rest. In order to resolve the viscous sub-layer, the first grid cell needs to be at about $y^+ \sim 1$, and a prism layer mesh with a growth rate no higher than ~ 1.2 should be used. These values ensure the mesh will be able to resolve gradients in the sub-layer adequately, however, this will add significantly to the mesh count.

Regarding Ansys Fluent, which is the solver used in this thesis, the boundary layer is resolved by using two different wall modelling strategies: the wall function model and the near-wall model. The wall function model will assume that the first two-layer do not need to be resolved by the mesh. It requires the first cell to be in the log-law region or maximum thickness of $y^+ = 30-50$ extended to 20% boundary layer thickness. This method will result in low computational cost respect to the near-wall model that, on the other hand, fully resolves all three regions giving a very accurate simulation of the boundary layer.

However, this model requires the first cell maximum height to be $y^+ = 5$ or less and extended to $y^+ \cong 1000$ or 20% of boundary layer thickness.

Figure 2.30 shows the wall modelling strategies graphically.

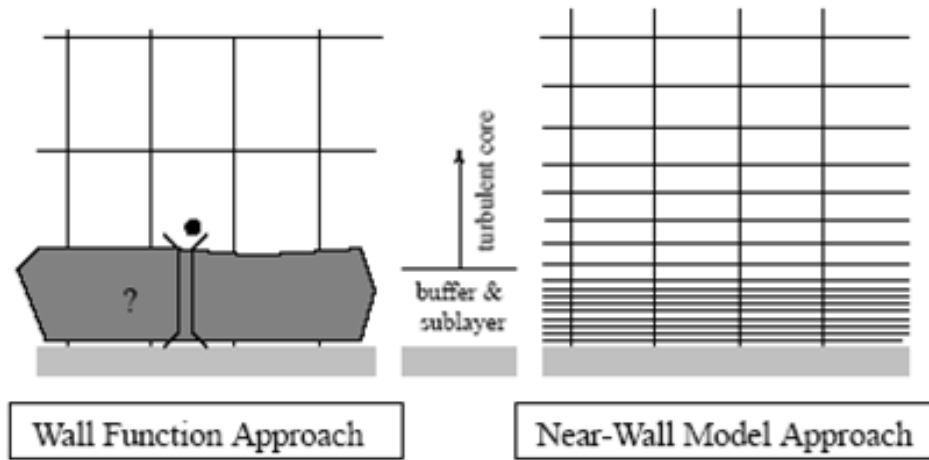


FIGURE 2.30: Wall Modelling Strategies

To accurately resolve the boundary layer, prism layers need to be generated at the model surface. The height of the first prism layer, as mentioned above, depends on the wall treatment chosen and extended to 20% of the boundary layer thickness.[\[46\]](#)

Chapter 3

Methodology

In this Chapter, the methodology used along this project is presented to describe the whole structure of the conducted study and to introduce the development of the BLI engine model with an overview of the single steps adopted, from the geometry generation to the computational analysis involved with the CFD simulation.

In this thesis, the phenomenon of the boundary layer ingestion was studied to observe its effect on the intake design and on its performance.

The very first considerations were formulated for a baseline case that aimed to represent a 2D clean fuselage without the BLI engine in order to learn about the behaviour of the airflow and the development of the boundary layer over a conventional aircraft characterized with podded engines.

Later, a modelled engine was integrated into a new 2D geometry simulating the embedded configuration in order to ingest the thickest boundary layer possible. It mainly consists of a BLI engine installation all-around a tubular fuselage and positioned at the rear of a baseline aircraft. It was created for different shapes of the lip of the intake, throat height and CR to evaluate the flow behaviour at different mass flow ratios, and the structure of the S-shaped duct was built up to ensure a uniform flow at the AIP. The methodology implemented for this kind of geometry will be presented in detail in the next Chapter 4.

Both the baseline and embedded geometry were built using Matlab code. The meshing generation was then realized on ICEM in order to run a Computational Fluid Dynamics (CFD) study on it using the Fluent solver. All the simulations were performed at the aero design point, meaning an altitude set at 11,000 m and a flying Mach number set at 0.78. Finally, when the convergence of the model was confirmed, flow behaviour was assessed, and results collected.

For all the cases are taken into account, the parametric study conducted with CFD was performed after developing a boundary layer thickness profile defined as the 99% of the free stream velocity.

The amount of boundary layer ingested will depend on the mass flow ratio derived from the studied geometry.

During the Chapter, the design modelling of the baseline geometry is firstly introduced and simulated to extract the boundary layer profile that will be consequently used as a starting point for the integrated geometry with the nacelle. The thickness of the boundary layer developed along the clean fuselage will give the geometrical parameter of height at which the nacelle will be placed in the second primary model studied.

The following Figure 3.1 displays the most important steps undertaken during the elaboration of the project through a flow diagram.

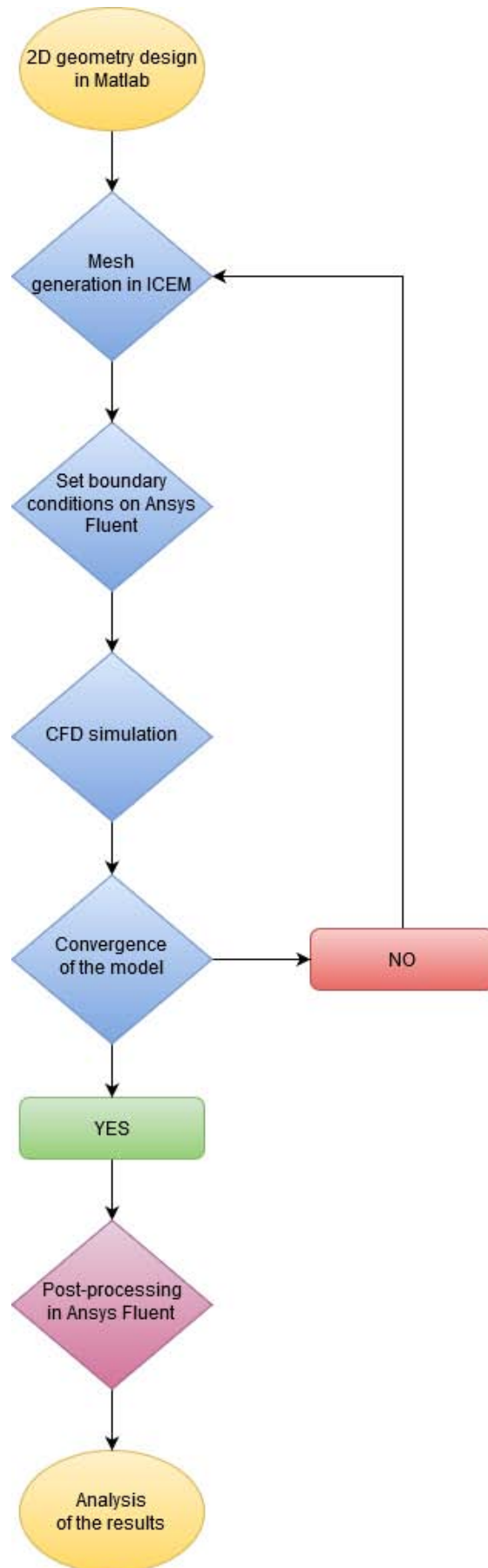


FIGURE 3.1: Flow diagram of the main steps of the work process

3.1 Baseline Geometry and Sizing

The baseline geometry consists of a bi-dimensional clean fuselage (named Case 1) that has been designed for answering the basic geometrical requirements such as fuselage length and radius and for studying how the boundary layer profile could develop over a standard civil aircraft in the absence of an embedded engine, which is here the matter of study.

It has been built starting from the generation of Matlab code, adapting the geometry to the parameters of a civil baseline aircraft that are summarized in the Table 3.1 below.

Radius Fuselage	2 m
Length Fuselage	24 m

TABLE 3.1: Fuselage geometrical parameters

The Figure 3.2 is the plain schematic representation of the modelled clean fuselage.



FIGURE 3.2: 2D Aircraft geometry: clean fuselage of the baseline geometry

3.1.1 Aircraft Initial Condition

The aircraft is supposed to fly at cruise condition at an altitude of 11000 m and with a Mach number of 0.78. All data parameters coming from this flight condition are listed in the following Table 3.2.

Parameters	Values
Altitude [m]	11,000
Ma	0.78
T [K]	216.82
P [Pa]	22696
ρ [kg/ m^3]	0.3648
μ [kg/ms]	1.44×10^{-5}
a [m/s]	295.14
U_∞ [m/s]	230.21
Re_L	1.7×10^8

TABLE 3.2: Data parameters at cruise condition

The choice of the far-field domain has been selected for the geometry, making some consideration about the meshing quality and resolution. [48]

Normally the dimensions of the domain are supposed to be at least 100 times the fuselage length, but since it would have required a considerable amount of simulation run time, a smaller domain has been taken into account which still ensures a reasonable level of accuracy to avoid any influence of the boundary conditions over the object of study.

Starting from the nose of the aircraft, the domain designed consists of a *distance from the far-field* (dff) two times the length of the fuselage (c), a rounded far-field in upper direction with a radius four times the length of the fuselage and leftward the outlet located after an extension of the surface of the fuselage of the dimension of the fuselage itself.

Figure 3.3 illustrates the domain around the clean fuselage built for the first model assessed.

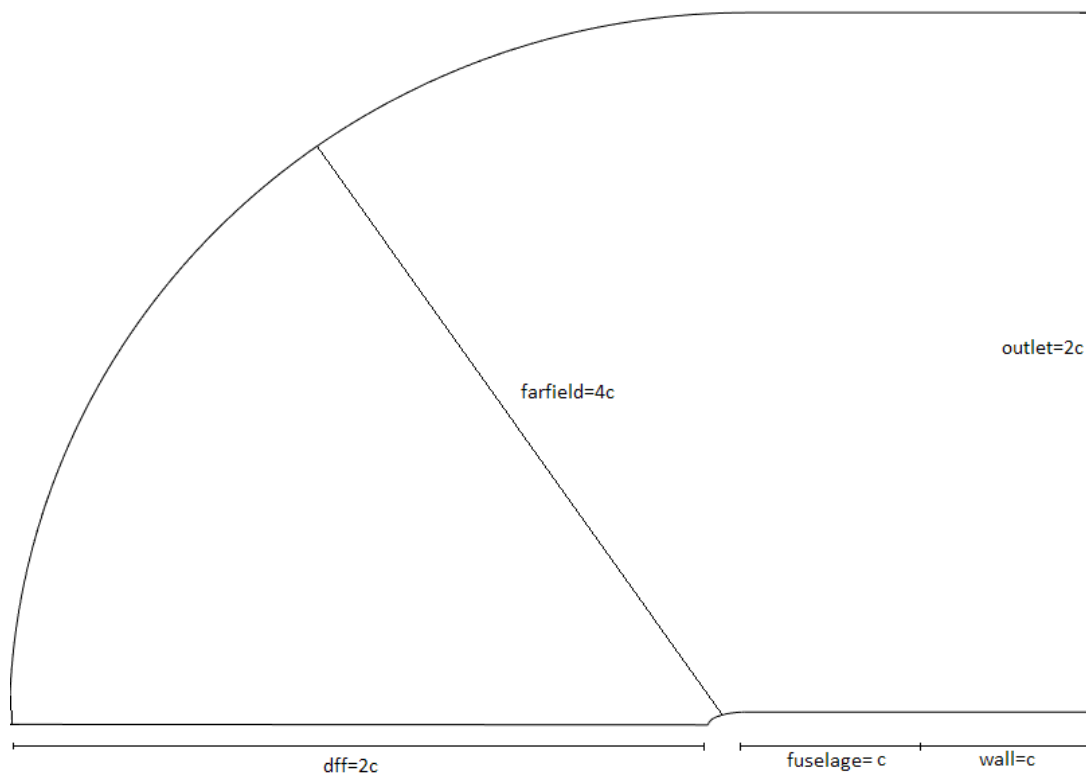


FIGURE 3.3: Domain around the clean fuselage in the baseline geometry

3.2 Mesh Generation

Mesh generation is a crucial step in performing a computational simulation as it represents one of the most crucial parts of the realization of a good CFD model. The simulation results are highly dependent on the mesh refinement and quality; thus, a finer mesh is best required to have better results.

However, a very fine mesh would take a long computational time consuming, and so the mesh that has been generated can be considered to be fine enough to capture the flow features of interest.

In order to provide a balance between accuracy and computational cost, a smaller domain has been created respect to previous works assessed, and in this study, it has been built using ANSYS ICEM.

The domain created and introduced in the previous section satisfies the requirement to be far enough from the model such that the flow around the geometry does not interfere with the boundary.

Firstly, some parameters need to be introduced to proceed with generating the mesh, in particular, the y^+ and Re which represent the first distance wall spacing and Reynolds number, respectively. They can be considered as model parameters that require to be estimated to capture the flow in the region of interest.

Reynolds number has been defined in Chapter 2 as the ratio of inertial forces to viscous forces describing the changeover of the flow in the boundary layer while the y^+ is defined as a non-dimensional wall distance for a wall-bounded flow.

Since $k-\omega$ SST (Shear Stress Transport) is the turbulence model used; the value of y^+ must be close to unity. To take full advantage of the fact that this model is formulated to be near-wall resolving model, where the mesh resolves the viscous sub-layer, y^+ should be ≈ 1 also in this work even to ensure an accurate prediction of flow separation. Actually it has been estimated to be equal to $y^+ = 5.8e-6$ m for a $Re=1.7e+8$. As it is explained in Chapter 2, low Reynolds numbers are likely to produce a laminar boundary layer while a high number will generate a turbulent one.

Since the Reynolds number for the simulation is very high, the boundary layer generated is fully turbulent.

In Figures 3.4 and 3.5, the meshing built from the far-field domain is graphically illustrated. A growth ratio of 1.05 and has been used approaching to the fuselage in the direction perpendicular to the surface, a *Cell-Wall Distance* of $2.86e-6$ m has resulted from the analysis and effective value of wall distance $y^+ \sim 0.5256$ has been derived.

These values ensured the mesh to be able to resolve gradients in the sub-layer adequately as the $k-\omega$ turbulence model and the *Near-wall model* approach required. A general overview and then a finer view of the smoothness of the mesh along the fuselage are shown in the pictures below.

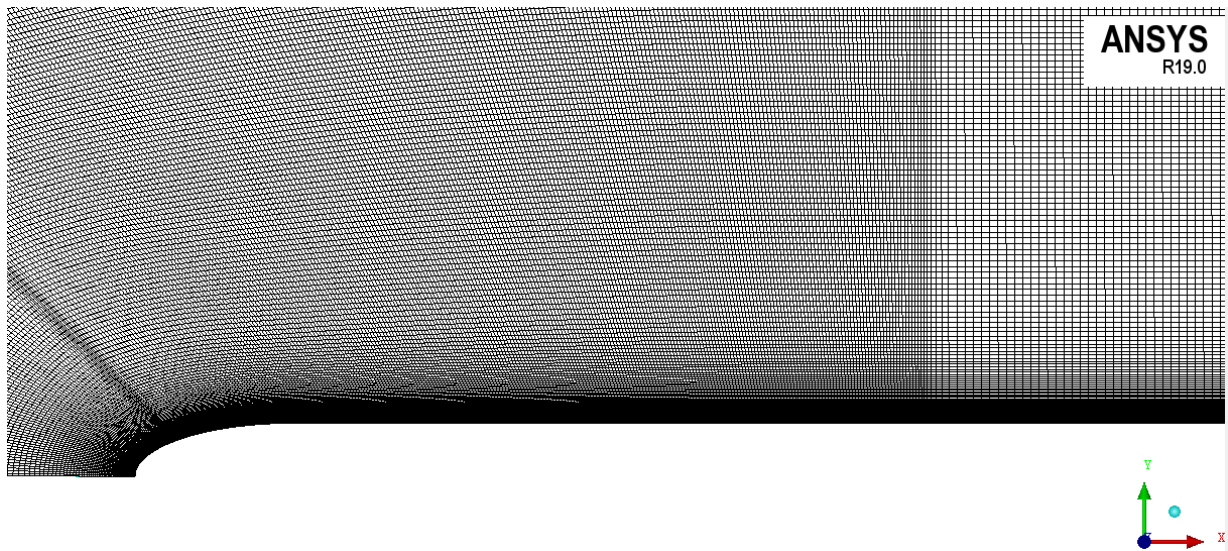


FIGURE 3.4: Meshing around the clean fuselage

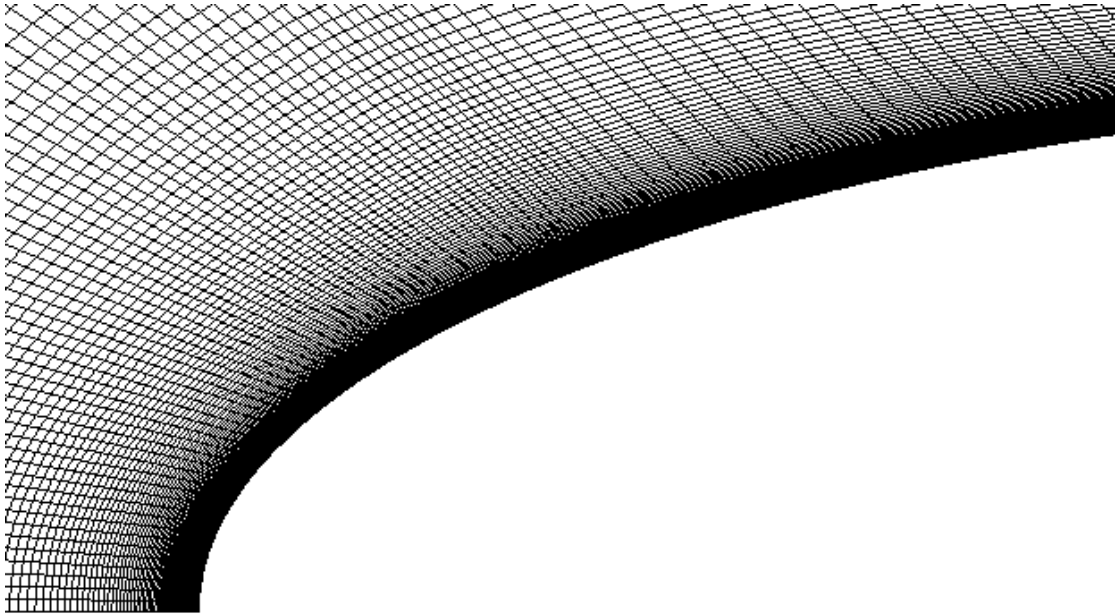


FIGURE 3.5: Smoothness of the meshing along the fuselage

An automated structured mesh and a multi-blocking strategy have been used to generate the mesh. A multi-block structure approach is a typical topology applicable to axisymmetric profile and intake geometries. Usually, manual creation of multi-block structures is more time consuming compared to unstructured meshes, indeed the procedure has involved the use of blocking and O-grid generation before building the mesh to ensure the smoothness in the presence of rounded geometries (visible in Figures 3.6 and 3.7). In an O-grid structure, lines go around the profile, from the profile surface to the outer boundary. "O" within the name comes from their "circular" shaped.

The number of nodes for mesh distribution around the domains is presented in Table 3.3, while the total number of nodes for the mesh of this geometry is 292600.

Location	Number of Nodes
Far-Field	420
Wall	1060
Outlet	700

TABLE 3.3: Number of nodes around the domain

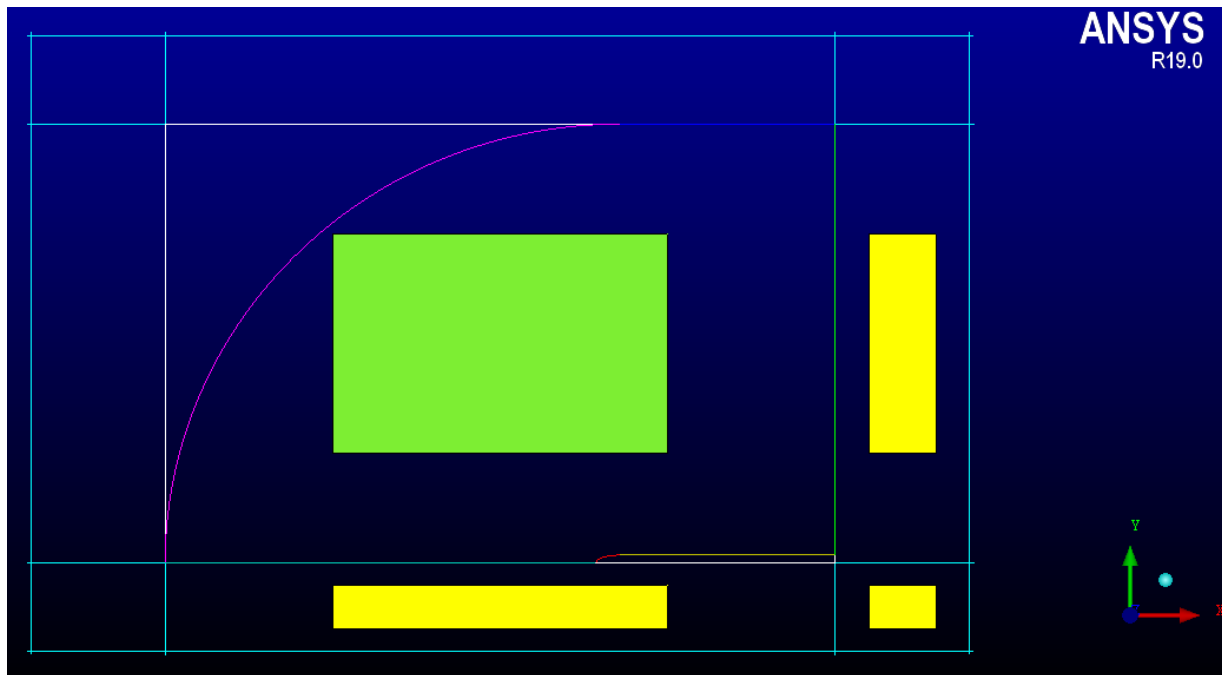


FIGURE 3.6: 2D planar blocking generation

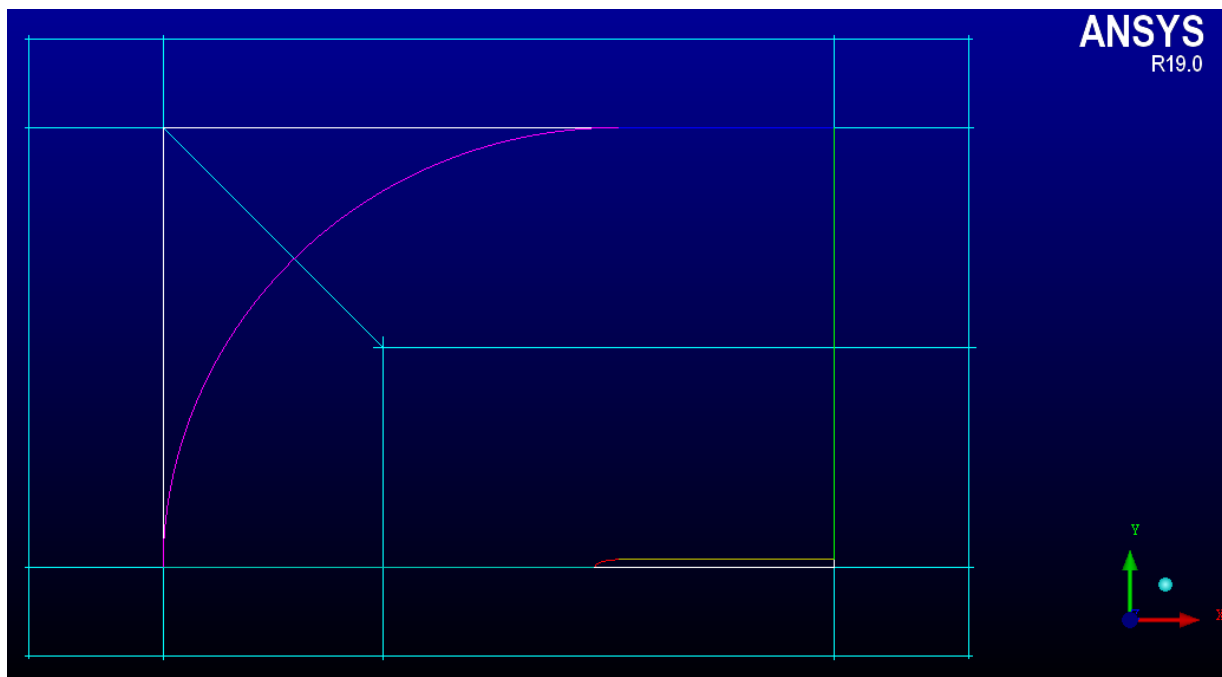


FIGURE 3.7: O-grid generation

3.3 Simulation Setup

This section deals with settings and tools developed in Fluent before running the 2D simulations. The very first case, run for the clean fuselage, aiming to study the behaviour of the flow within the lowest layers close to the wall and thus to extract the boundary layer profile as a term of comparison for other cases. Later, a certain number of simulations have been run and assessed encompassing the intake design at the rear of the fuselage (Case 2) and changing both geometrical parameters such as the shape of the lip and initial boundary conditions such as the mass flow ratio.

The simulation setup of the solver involved some initial choices:

- Pressure-based type
- Steady state time
- 2D axisymmetric space
- Absolute velocity formulation.

The pressure-based solver has been chosen because it was initially designed for incompressible and mildly compressible flows, while the other solver type, the density-based approach, shows advantages over the pressure-based solver for high-speed compressible flows. The energy equation was used to account for the energy dissipation within the diffusion of the flow.

The turbulence model selected was $k-\omega$ SST (*Shear Stress Transport*) as it takes account of the complex boundary layer flows under adverse pressure gradient and separation, previously mentioned in section 3.2 and Chapter 2. Even the viscous heating was turning on to include viscous dissipation terms, which describe the thermal energy created by viscous shear in the flow.

The material type selected for the analysis was fluid, namely air with the ideal gas property.

The material property of specific heat (C_p) is calculated as a function of temperature and was chosen to be described with the *piecewise-polynomial* option while the thermal conductivity was set constant at 0.0242 W/mK. For the viscosity, the Sutherland law with three coefficient method was used as it is suitable even for mildly compressible flow. The operation pressure is set to 0 Pa, at a far distance upstream to let the absolute value be equal to the static values. This is a valuable input to give as it addresses compressible flow.

Then, moving forward with the settings, about the solution methods, the coupled scheme was selected. Within the spatial discretization, the *Green-Gauss Cell-Based* was selected for the gradient. The rest of the discretization, including pressure, density, momentum, turbulent kinetic energy, specific dissipation rate and energy, was set up using the second-order upwind method. The second order is required to solve the boundary layer flow and shock waves occurrence. These selections help to obtain a more accurate solution but at the cost of a more expensive computation.

As solution controls, the explicit relaxation factors have been set to 0.5 for momentum and pressure. Besides, under-relaxation factors to control the update of computed variables at each iteration could be set for the pressure-based solver. In Ansys FLUENT, the default under-relaxation parameters for all variables are set to values that are near-optimal for the largest possible number of cases, and in this study, the calculation has begun using the default under-relaxation factors, which are summarized in Table 3.4.

Equation	Under-Relaxation Factors
Density	1
Body Forces	1
Turbulent Kinetic Energy	0.8
Specific Dissipation Rate	0.8
Turbulent Viscosity	1
Energy	1

TABLE 3.4: Under-Relaxation Factors

3.3.1 Boundary conditions

Several boundary conditions can be imposed at the boundaries of the computational domain. Starting with the baseline case, the following conditions were used in the current CFD study:

- *Wall* condition – for the aircraft surfaces, namely the fuselage. Wall condition with the no-slip condition and smooth wall with the adiabatic condition was applied, while the dff and the top part of the domain corresponds to the inviscid wall.
- *Pressure far-field* condition – far-field domain was imposed with this condition. The pressure far-field boundary condition is characteristic since it uses specific information to determine the flow variables at the boundaries. Pressure far-field conditions are used to model a free-stream condition at infinity, with free-stream Mach number and static conditions being specified. The gauge pressure was set to 22696 Pa, which is equal to the absolute pressure since the operating pressure is set to 0 Pa far upstream of the domain. Mach number was set to 0.78 and the temperature to a static value of 216.82 K. The two turbulence parameters: turbulence intensity and viscosity ratio have a value of 0.05 and 0.1, respectively.
- *Pressure outlet* condition – the outflow of the domain was applied with this condition. The gauge pressure was set to 22696 Pa and the temperature at 216.82 K and the average pressure specification was turned on.

The solver was then initialized using hybrid initialization from relative to cell zone frame and computed from pressure far-field.

The external-aero favourable settings was also selected from the initialization options. Finally, to verify the convergence state of the solution the global scale continuity residual value has to fall to at least three orders and all other globally scaled residuals must be less than a value of 10^{-6} .

No increments in the residuals have been observed after the 3 or 4 iterations, thus no changes have been made on the under-relaxation factors. These conditions were all met, and then the obtained results could be used for the analysis. An example of a converged residual is shown in Figure 3.8.

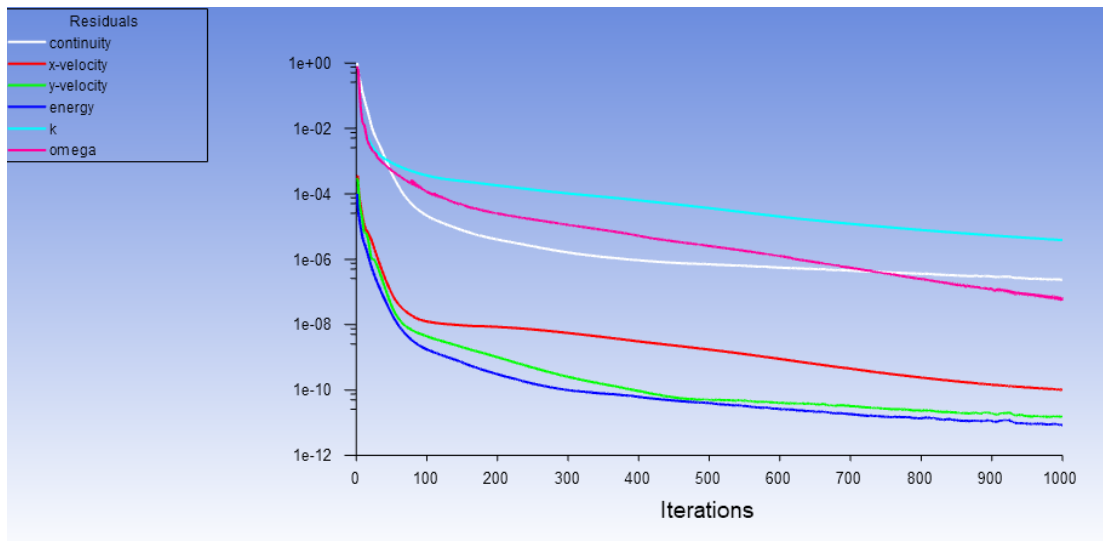


FIGURE 3.8: Residuals

3.4 Convergence Study

The convergence investigation is essential when an aerodynamic analysis is performed. The results accuracy and, in general, the convergence in CFD depends on several factors, such as the mesh quality and the suitability of the applied boundary conditions. Increasing the number of nodes increases the grid resolution that helps to improve the mesh quality.

This can be processed simulating three or more different mesh sizes that commonly correspond to a fine, medium-fine and a coarse mesh.

Relatively to this project, the number of elements involved is generally rather low because the study conducted is bi-dimensional.

A convergence study was managed for both the cases accounted for. For each mesh size, the number of elements was incremented and reduced of the 30% of elements respect to a medium initial mesh size adopted.

All cases have been run at simulation conditions with a number of 1000 iterations while the results were monitored.

This convergence study was necessary to verify the quality of the mesh and the consistency of the results that are used as a starting point assessment for the main geometry. For this first case, the coarse mesh consists of roughly 140 thousand elements, the medium mesh of 295 thousand elements, and the fine mesh of 495 thousand elements that are shown in detail in the next Table 3.5.

Mesh	Coarse	Medium	Fine
Far-field	294	420	546
Wall	294	420	546
Outlet	490	700	910
Number of Nodes	143080	292600	495040

TABLE 3.5: Mesh size variation

Later, to ensure the convergence of the model, the consistency of the obtained results was verified by assessing the convergence of a physical parameter. The results were compared in terms of the evolution of the static pressure along the fuselage as functions of the number of cells. Figure 3.9 shows how the development of the static pressure along the fuselage doesn't change considerably among the different size meshes. Global differences are less than 1%; thus, all the models converge, and the medium mesh can then be chosen as a verified mesh since it showed reasonable simulation run time for the initial simulation.

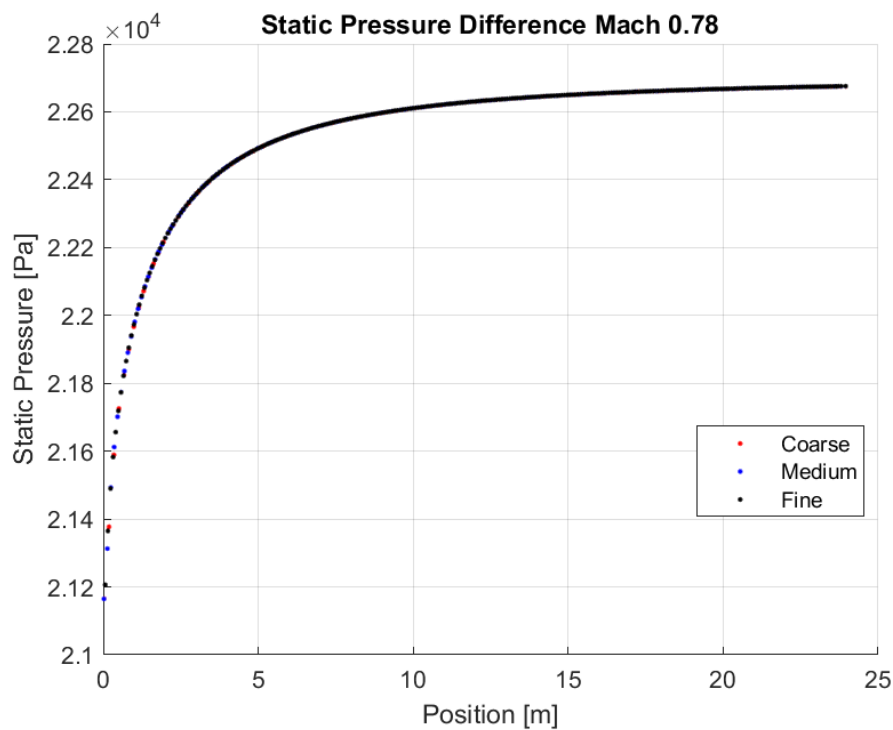


FIGURE 3.9: Static Pressure for different mesh size

3.5 Post Processing

Once the mesh has been verified, the first simulation has been run at cruise conditions in the solver Fluent to obtain a satisfactory boundary layer profile along the fuselage length. This section aims to assess the behaviour of the flow over a surface simulating the fuselage of a conventional aircraft through the CFD post-processing tools.

To evaluate how much boundary layer can be ingested with a BLI system, assessing the thickness of the boundary layer developing over the fuselage becomes firstly essential.

This part deals with the process involved in extracting the boundary layer profile at the rear of the fuselage, where a BLI engine would be ideally located.

Then, at the end of this part, the results are summarized and collected to be exploited in the following section.

3.5.1 Extraction of the Boundary Layer Profile

All the post process was automated by writing a journal file through a script created in Matlab that produced the correct session files to play in CFD-Post. This automation was necessary to generate a *Rake – surface* along the entire wall and thus to evaluate the thickness of the boundary layer at a distance of 24 m, where the intake will be placed.

Figure 3.10 illustrates the distribution of Mach numbers close to the surface. The flow, moving on the upper surface, rapidly reaches high speed after the stagnation point keeping the subsonic far-field condition, and then tends to decelerate downstream of the fuselage. Since the location of interest is far away from this region, it is not considered a concern. As can be seen, the slight change in colour next to the wall represents the decrease in velocity due to the no-slip condition at the wall, and thus the presence of the boundary layer. At the same time, in the Figure below 3.11, the reduction in total pressure proves the presence of losses due to the viscosity of the flow in proximity of the wall.

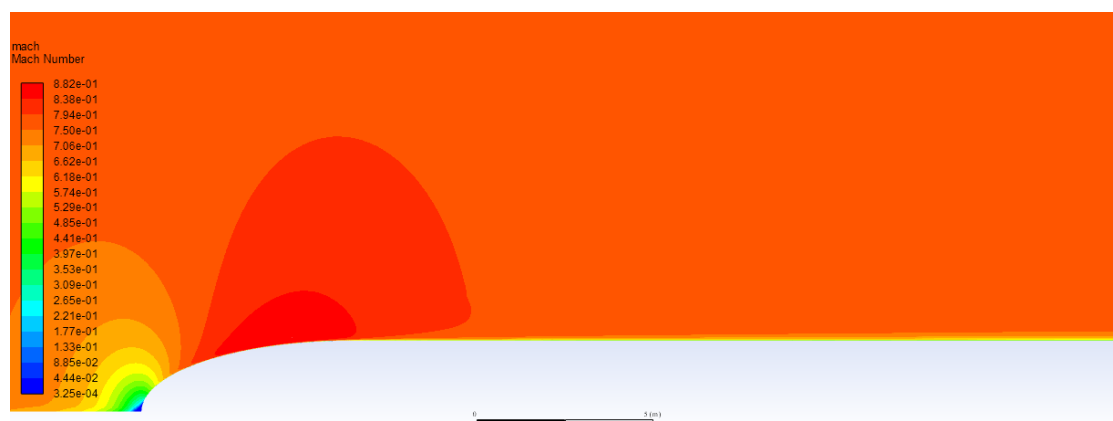


FIGURE 3.10: Mach Number Contour-clean fuselage

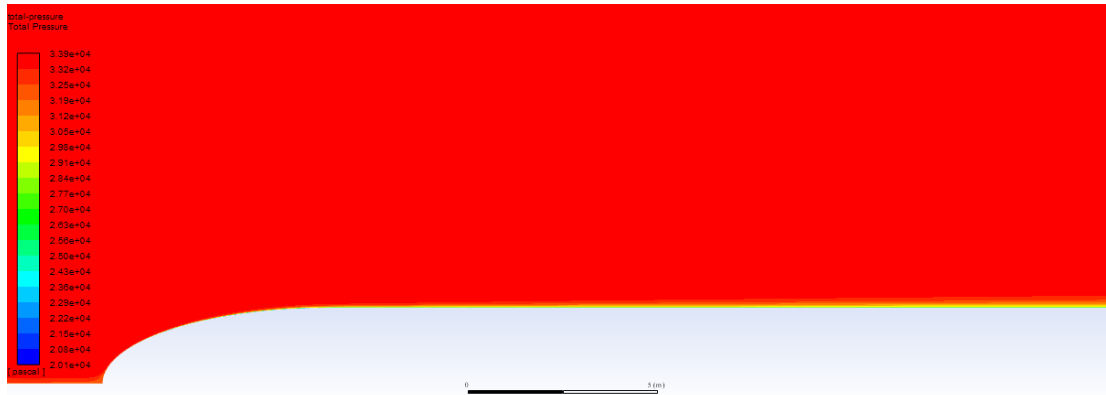


FIGURE 3.11: Total Pressure Contour-clean fuselage

The 99% definition has been used to calculate the thickness of the boundary layer. Defining δ as that distance from the wall where the velocity reaches 99% of the free stream velocity, the *y*-coordinate points of the *Rake – surface* system have been interpolated to find the height of the boundary layer accounting for a free stream velocity of 230.21 m/s.

Figure 3.12 shows the shape of the boundary layer developed along the fuselage until the distance of 24 m, while Figure 3.13 is a representation of the typical velocity profile within the boundary layer at the end of the fuselage (24 m). The velocity profiles extracted for a Mach no. of 0.78 indicated no sign of reverse flows. This showed that the boundary layer has fully developed and, thus, was used for analysis. As known from theory, the velocity close to the wall is roughly equal to zero, while a rapid increase in velocity is visible moving away from the surface where it reaches the free stream velocity.

At the distance of 24 m the 99% of the free stream velocity corresponded to the searched height:

$$\delta = 0.4405m \quad (3.1)$$

With the information extracted from the boundary layer, the geometry of the nacelle has been set out for the main analysis of this thesis.

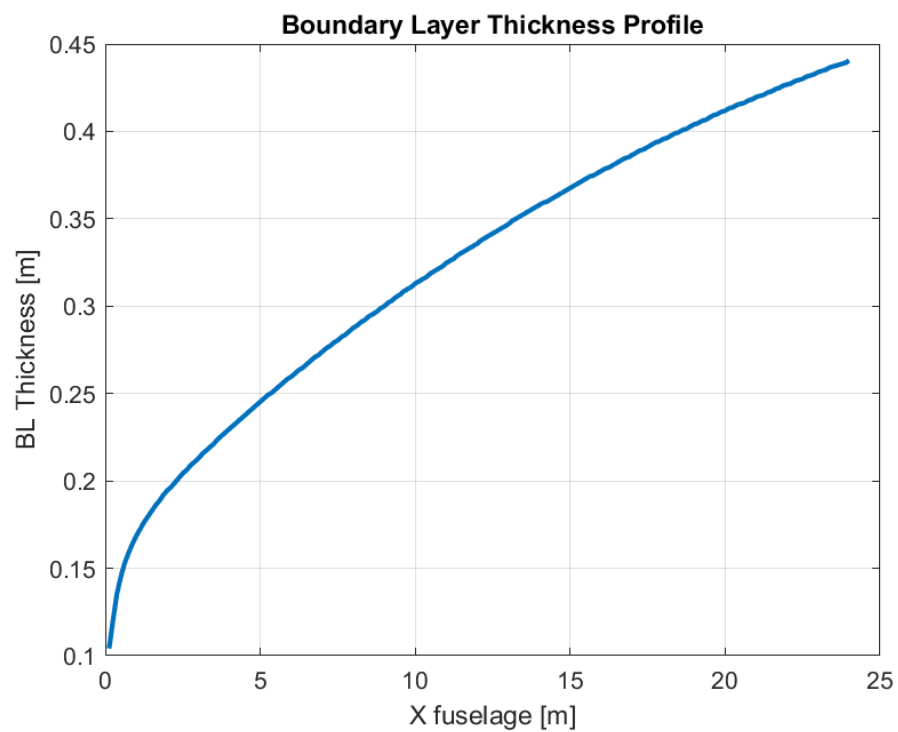


FIGURE 3.12: Boundary layer thickness profile from the nose to the end of the fuselage (24 m)

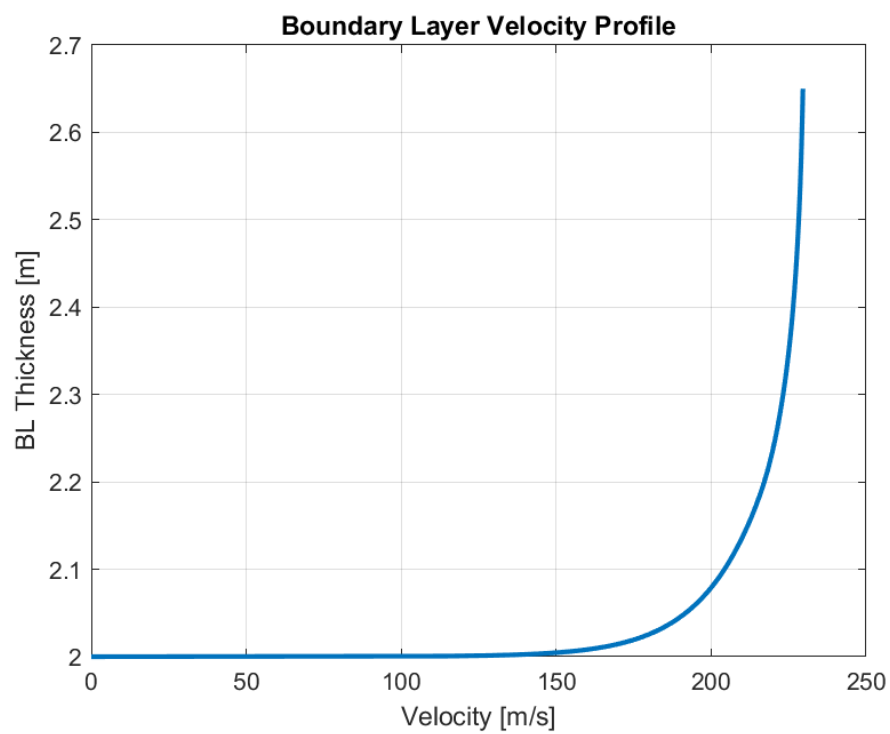


FIGURE 3.13: Boundary layer velocity profile calculated at the end of the fuselage (24 m)

Once derived this data, a construction line with the same height has been realized at the distance of 24 m, namely, where the nacelle will be placed for the next analysis. The mass flow rate passing through the relative annulus area $\dot{m}_{cleanfuselage}$ has been also calculated to quantify it within the boundary layer and then compare how much of it will be ingested in the presence of the nacelle.

$$\dot{m}_{cleanfuselage} = 470.2904 \text{ kg/s} \quad (3.2)$$

Chapter 4

Methodology for BLI System

In this section, the intake design for a BLI modelling is set and run. Starting from the realization of the geometry and the simulation domain, all the dimensions and main parameters are described and established through several Matlab scripts in order to design the S-duct and the intake accounting for the effect of the lip, different throat heights, and contraction ratios (CR).

Later, the simulation is run for different MFRs in the solver Fluent after the validation of the mesh generated with ICEM that is shown and described during the section. Particular attention will be reserved for the accuracy of the mesh around the lip of the intake that firstly faces the free-stream and within the duct, especially at the outlet where the fan face is located.

The whole investigation neglects the back of the engine, thus the fan duct and the fan nozzle components, as well as their losses counting to focus on the lip and S-shaped duct design and explore the main internal flow features through it.

At the end of this part, the post-processing work is set to analyze data and results of each model and thus evaluate the pressure recovery within the duct and the uniformity of the flow at the AIP.

4.1 Geometry and Domain

Starting from the baseline geometry presented in the previous sections, an embedded engine has been integrated into the fuselage (named Case 2) to study the capturing of the boundary layer. In this case, 2-D geometry has been built, adding to the fuselage the first component of the engine, namely the intake encompassing the lip and the duct that has been chosen to be an S-shape duct.

Since the flow entering the intake is not the same depending on where the engine is placed on the airframe, this study is performed for the engine that ingests the thickest boundary layer achievable.

Thus, here the case of a central engine is studied, meaning an engine located at the rear of the fuselage ingesting the thickest boundary layer. The idea was to match the height of the inlet of the computation domain with the boundary layer thickness extracted from the previous study. In this way, the boundary layer will grow over 24m of fuselage before being ingested by the intake schematically represented in Figure 4.1.



FIGURE 4.1: 2D Aircraft geometry :Fuselage with the intake (Case 2)

For the first simulation, no changes have been made to the cruise condition of flight that is the same as the previous model, shown in Table 3.2. Figure 4.2 shows the selected domain and the distances from the model to the boundaries. In comparison with the baseline geometry, an extension of the wall has been built leftward, simulating the external surface of the intake.

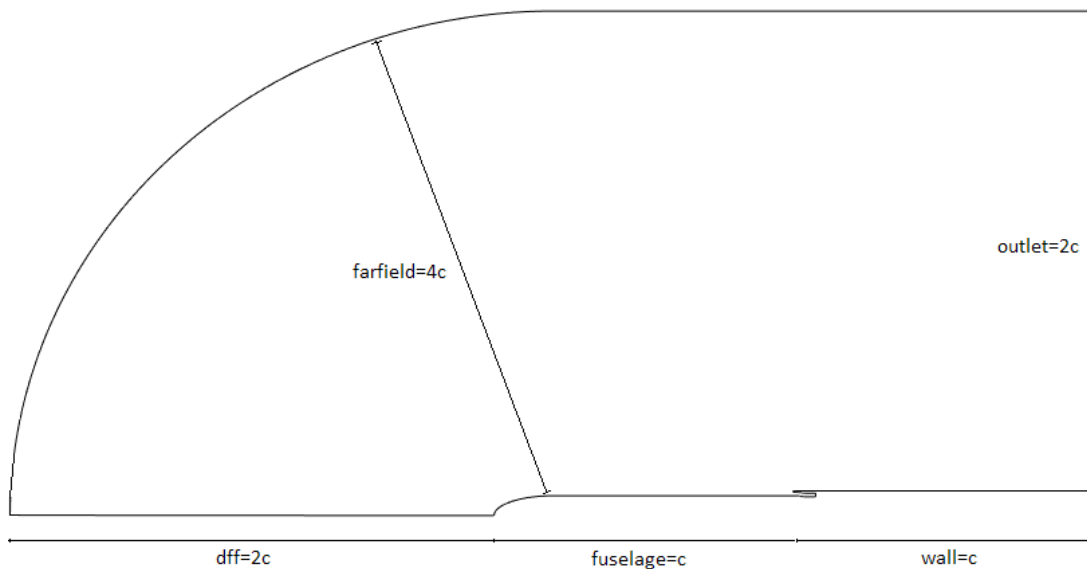


FIGURE 4.2: 2D Aircraft domain

4.2 Intake Design

In this thesis, two different shapes of the lip, throat heights and contraction ratio (CR) have been taken into account.

The first model of the intake has been realized accounting for a profile of the lip entirely realized with an elliptical geometry. The design choice made deals with an area contraction ratio between the highlight and the throat of 1.25, and an aspect ratio of the lip equal to 3.

$$A_{highlight} = 1.25 * A_{throat} \quad (4.1)$$

With this geometrical construction, the shape of the lip shows a well-rounded shape (Figure 4.3). This represents the first modelled geometry (Design A) of Case 2, while the second configuration processed in Case 2 deals with the choice of a cowl profile from the NACA 1-Series Inlets database elaborated from NASA (Design B) [49], and an area contraction ratio of 1.10.

The selected design coordinates are given from the NACA 1-85-100 inlet profile that has been used for the outer part of the lip.

The lower internal part, instead, has been built with a quarter of an ellipse, providing a thinner shape to the lip of the intake. Respect to Design A, indeed, the aspect ratio is more significant and equal to 6, giving the sharpness to the profile (Figure 4.3).

Here, the Table 4.1 with a summary of the main geometrical parameters describing both the profiles and the respective graphic representations.

	ELLIPTICAL LIP (Design A)	NACA COWL AND 1 / 4 ELLIPSE LIP (Design B)
Aspect Ratio (AR)	3	6
Contraction Ratio (CR)	1.25	1.10
Throat Height	0.3590 m	0.4038 m

TABLE 4.1: Lips design

The lips geometry has been chosen based on a previous study testing different inlet configurations and considering that the CR typically ranges from 1.05 to 1.20, where CR close to 1.0 represents a sharp lip and 1.2 characterizes a well-rounded lip.

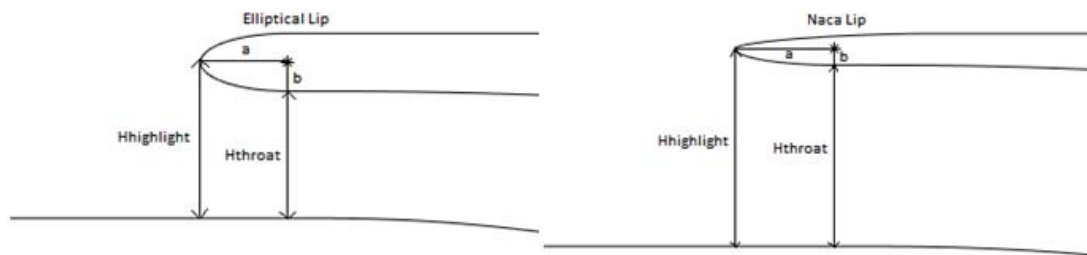


FIGURE 4.3: 2D Lips geometry: Elliptical lip shape profile on the left and Naca cowl external lip on the right

Both the configurations represent the first component facing the airflow, namely, the inlet of the intake. The inlet duct represents the part connecting the inlet with the fan. In this thesis, a S-shaped duct has been modelled and assessed to exploit its several benefits.

Actually, S-duct used in the boundary layer ingestion system has the benefit to reduce drag, size and weight by shortening the inlet duct, and it also allows to reduce ram drag and so the momentum of the inlet flow. However, such advantages need to be related to a high inlet pressure recovery, fan face Mach number in the range of 0.6-0.7 and an acceptable level of distortion during the engine operations. Moreover, the model accounted for does not include an engine core inside the duct.

4.3 S-duct Design

Regarding the design of the shape of the S-duct for the boundary layer ingestion, the fifth-order polynomial shape has been selected from a list of optimal wall shapes designed for small, low-speed wind tunnels test. [50]

An overview of wall contour shapes of the main polynomial orders can be observed in Figure 4.4.

Following the structure of the 5th order equation:

$$Y(X) = H_i - (H_i - H_e) * [6(X')^5 - 15(X')^4 + 10(X')^3] \quad (4.2)$$

where H_i is the contraction height at the inlet, H_e is the contraction height at the exit and X' is a non-dimensional streamwise distance: X/L and spanwise directions respectively. Both the upper and the lower bends have been designed with this polynomial shape.

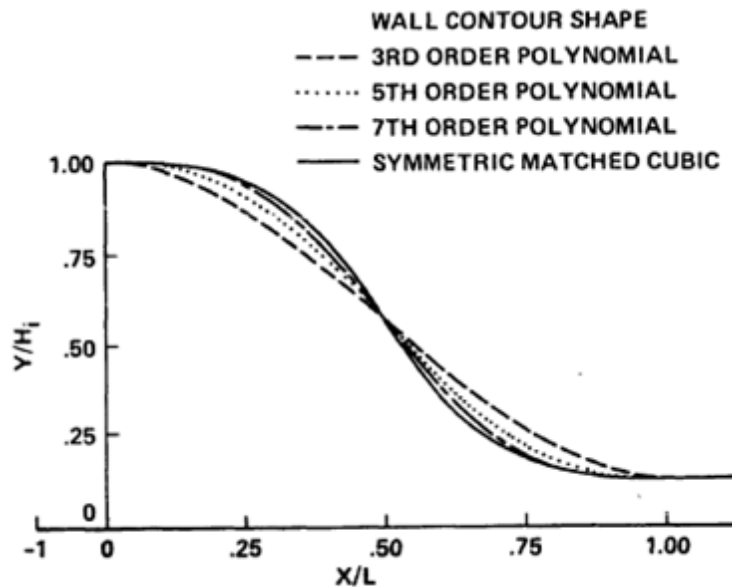


FIGURE 4.4: Wall contour shapes of contractions tested [50]

The main parameters for the S-duct are:

- Inlet height: D_i
- Outlet height: D_e
- Inlet average mean line: Hm_i
- Outlet average mean line: Hm_e
- Distance between the average mean lines inlet-outlet: Δh

All the parameters are dependent on the height of the inlet area which is the only variable left free.

As a first design choice, it has been decided that the highlight height, and thus the highlight area, which represents the wetted area exposed to free stream, would depend on the thickness of the boundary layer assessed in the model of the clean fuselage (Section 3.5).

The choice of D_i is, thus, a function of the shape of the lip of the intake and of the contraction ratio. Looking at the Figure 4.5 it can be noticed that D_i also represents the throat height of the duct and since

$$A_{throat} = \frac{A_{highlight}}{1.25} \quad (4.3)$$

and the height distance of the lower bend (Hi_{bottom}) is known, because equal to the radius of the fuselage, the inlet height of the duct can be derived easily through the evaluation of the annulus areas. These few calculations allowed to find the inlet average mean line Hm_i and, therefore, all the parameters upstream the duct.

Regarding the outlet of the duct another design choice has been done accounting for the minimum average distance Δh between the mean line of the inlet and the outlet. This parameter is essential because it controls the radius of curvature of the bends. It has been fixed at the value of 0.1 m in order to have the maximum radius of the throat to be roughly equal to the maximum radius of the outlet. Since the fan is not too much embed in this study, the length of the S-duct is about 2 m and the curvature is very light, aiming to border flow separation and help pressure recovery increasing at the fan interface. The average outlet mean line Hm_e is, therefore, calculated as the difference of the average inlet mean line (Hm_i) and the Δh .

Finally, some considerations have been done relative to the outlet height of the duct D_e , and consequently to the outlet area. The expansion ratio inside the duct has been put equal to 1. In this way, the outlet of the duct has been built with the exact same area as the highlight limiting the possibility of the flow separation.

$$A_{out} = A_{highlight} \quad (4.4)$$

Setting the same areas should prevent from reaching Mach numbers major of 0.78, and thus supersonic condition, keeping at the AIP a Mach number no higher than the condition of the far-field.

Testing MFRs less than 1, the Mach number expected at the outlet would always be less or even equal to 0.78.

The following Table 4.2 presents the main geometrical characteristics of the reference geometry calculated from the axis of symmetry of the fuselage, and Figure 4.5 gives an idea of where the variables are located within the duct.

Dimension	Design A	Design A
D_i	0.3590 m	0.4038 m
D_e	0.4704 m	0.4653 m
Δh	0.1	0.1
Hm_i	2.1795 m	2.2019 m
Hm_e	2.0795 m	2.1019 m
Hi_{up}	2.3590 m	2.4038 m
He_{up}	2.3147 m	2.3345 m
Hi_{bottom}	2 m	2 m
He_{bottom}	1.8443 m	1.8692 m
L	2 m	2 m

TABLE 4.2: Geometrical characteristics of S-duct

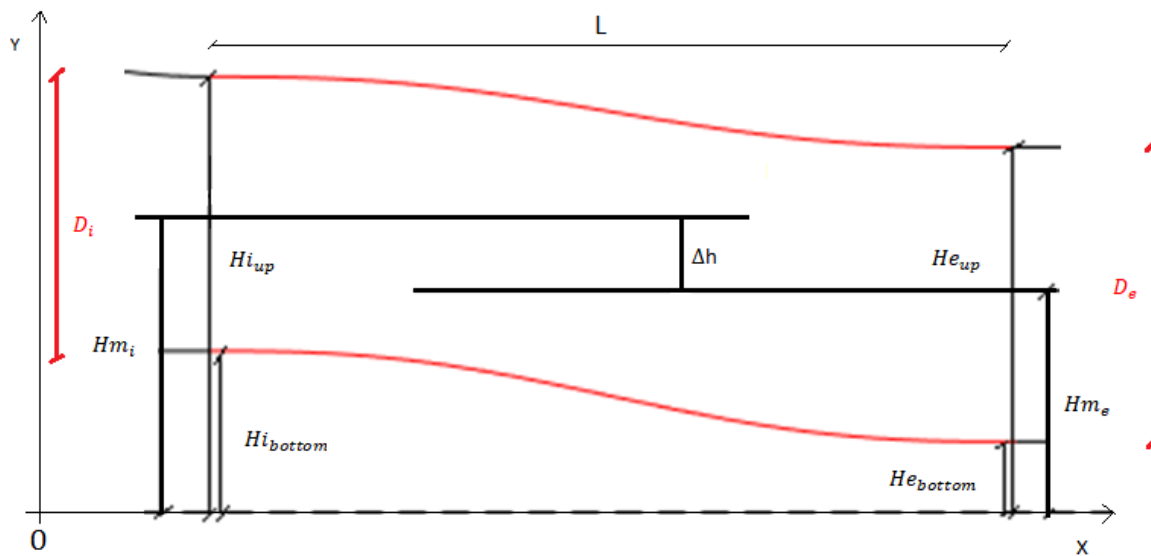


FIGURE 4.5: S-duct main design parameters

Next, before sending this geometry into ICEM for the meshing, it is necessary to check if all the surfaces, including the S-duct geometry, are merged properly.

This is a very important step to take because otherwise, the mesh may not be successful due to the presence of holes or discontinuities within the geometry.

4.4 Mesh Generation

Accounting for more complex geometry, the construction of the mesh needs to be accurate enough close to the most critical areas. This thesis aims to test the diffusion upstream of the intake and to understand how the flow behaves when it goes through the duct; this is why the mesh generated was made gradually smaller near the areas of interest within the intake. In particular, since the lip of the intake and the internal flow inside the duct are the areas of interest in this investigation, higher mesh resolution is present in these sections; otherwise, the model may not be accurate enough, leading to a false conclusion about the flow behaviour in these regions.

All the domain was placed far enough from the model to avoid interference with the boundary. In this project, $k-\omega$ SST is the turbulence model used. Thus the value of y^+ must be kept close to unity. The non-dimensional spacing of the first node (y) was calculated and estimated to be $y^+ = 5.8e-6$ m for a $Re = 1.7e+8$, while the effective calculated value on the wall resulted in being about $y^+ = 0.7092$.

A growth ratio of 1.1 and 1.2 was used close to these areas in the direction perpendicular to the surface and propagating far away in order to ensure the mesh being fine enough to capture the flow features of interest. A *Cell-Wall distance* of $3.33e-6$ m has resulted from the process of meshing along the fuselage, while a *Cell-Wall distance* of $3.42e-4$ m was found around the nacelle.

Figure 4.6 gives an overview of the whole meshing system around the model encompassing the intake.

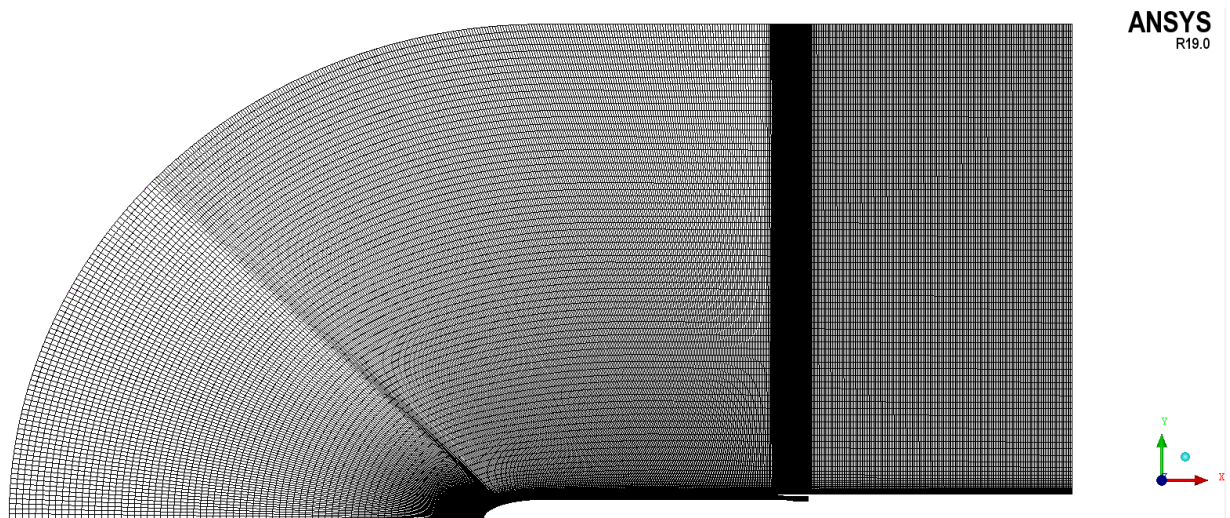


FIGURE 4.6: General meshing domain with BLI engine

As the previous geometry, a multi-block strategy was used to generate the mesh. An O-grid was used in the far-field, and the outer block of the O-grid was wrapped around the nacelle to form a C-grid. The quality of the solution is affected by the number, size and distribution of cells in the domain. The grid quality was checked for the mesh, and thus a convergence study was carried out to ensure the result obtained were reliable.

Figures 4.7, 4.8, 4.9 show a representation of the realization of the blocking system through the O-grid tools considering the main geometry.

The number of nodes for mesh distribution around the domains is presented in Table 4.3, and the total number of nodes for the mesh of this geometry is 113416.

Location	Number of nodes
Far-Field	585
Wall	377
Outlet	91
Outlet duct	91
Duct	260

TABLE 4.3: Number of nodes around the domain

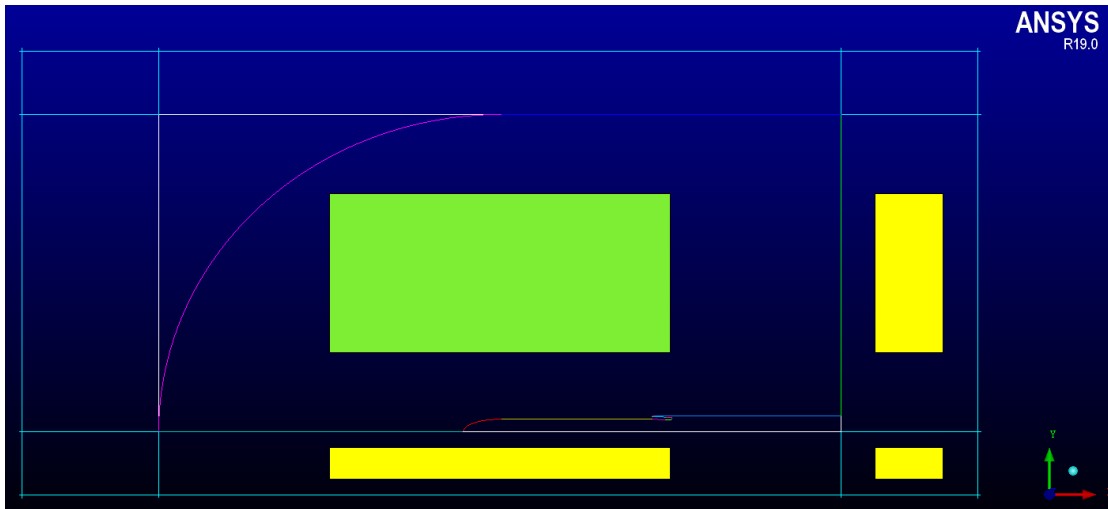


FIGURE 4.7: Blocking automation (Design B)

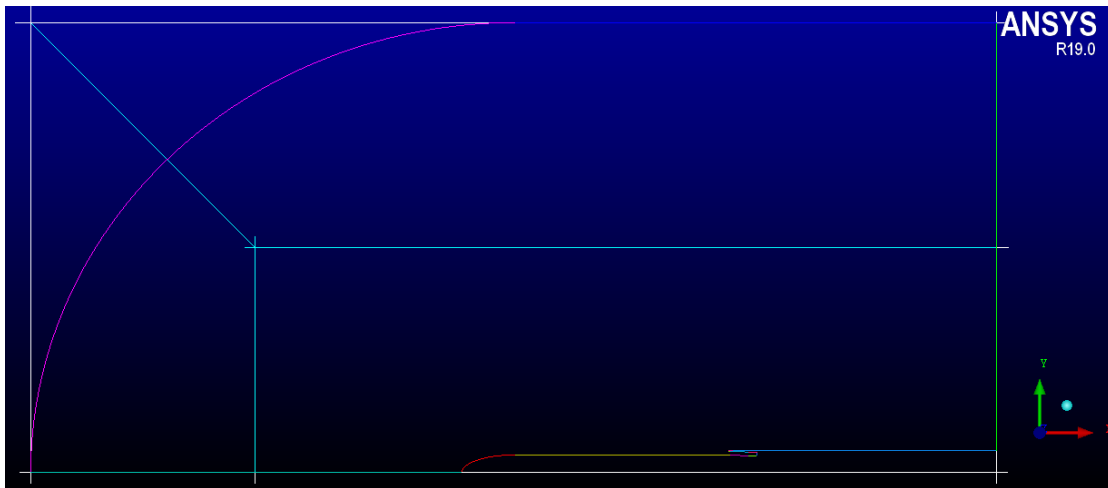


FIGURE 4.8: O-grid generation (Design B)

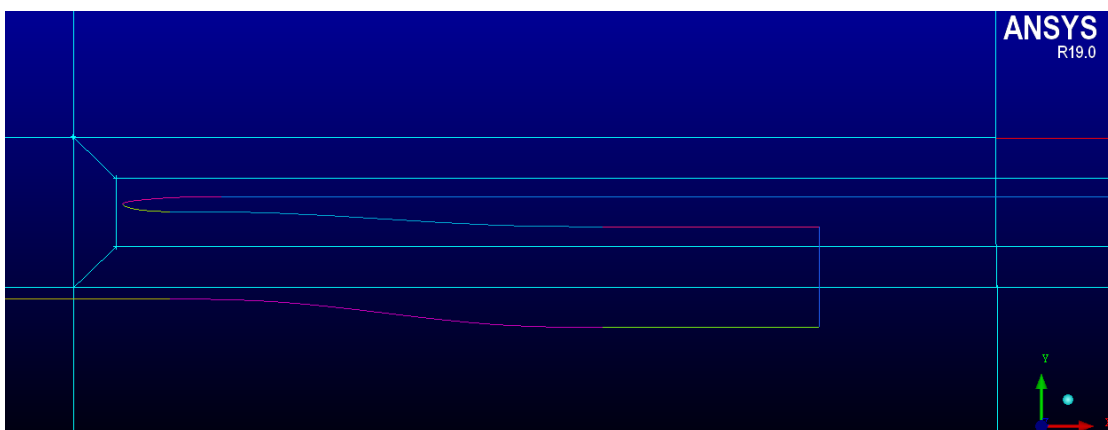


FIGURE 4.9: Blocking automation and C-grid generation around the nacelle (Design B)

This data comes from the meshing of Design B, which has been considered as the reference model. Indeed, the differences in geometry construction between the two profiles are very slight. Therefore, the characteristics of the meshing of Design A are very similar in terms of the distribution of nodes around the domain and dimensions of the cells.

However, a meshing representation of the different types of lips accounted is given in Figures 4.10 and 4.11 displaying the mesh around the region of interests.

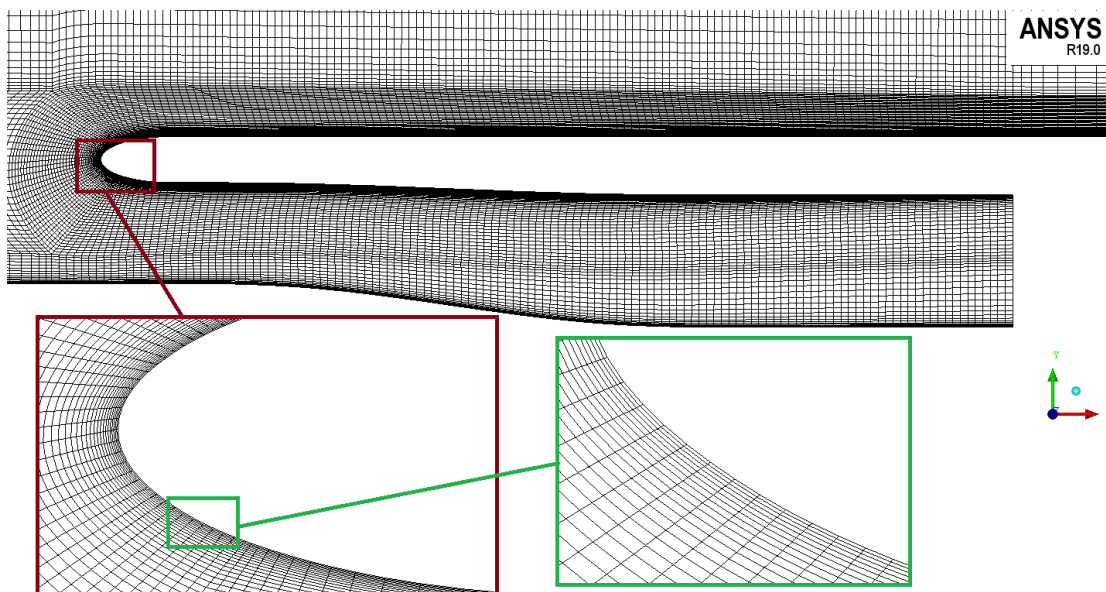


FIGURE 4.10: Mesh around the elliptical lip (Design A)

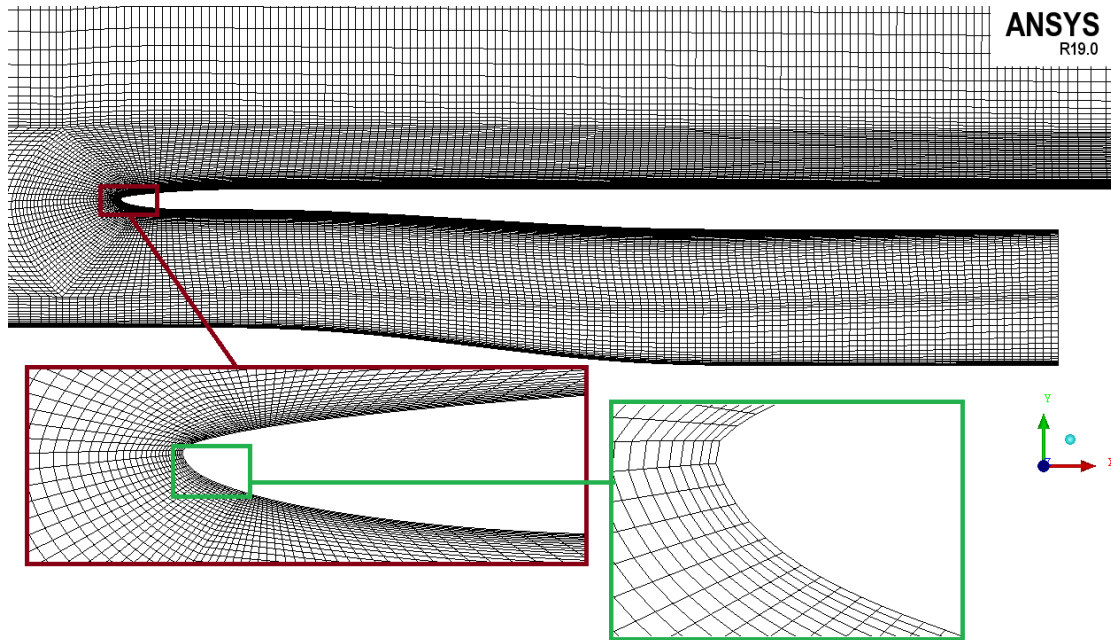


FIGURE 4.11: Mesh around the sharp lip (Design B)

Finally, for each model, the meshing has been verified and then opened with Ansys FLUENT to process the simulations and get results.

4.4.1 Mesh Convergence

The consistency of the obtained results was verified by assessing the convergence of a physical parameter to ensure the convergence of the model. The results were compared in terms of the evolution of the static pressure along the fuselage and of the inlet pressure recovery as functions of the number of cells.

The coarse mesh consists of roughly 70 thousand elements, the medium mesh of 115 thousand elements, and the fine mesh of 195 thousand elements. Three different mesh sizes are used to compare the results that are shown in Table 4.4.

Mesh	Coarse	Medium	Fine
Number of Nodes	66695	113416	192570

TABLE 4.4: Number of nodes for each mesh size

The model is convergent as it can be seen thanks to the following table (Table 4.5) and the following graphs (Figure 4.12, 4.13 and 4.14). The first shows the value of the pressure recovery as functions of the number of cells accounting for a MFR=0.85. The second the development of the static pressure over the fuselage, from the nose to the inlet where at approximately 24 m, the drop in static pressure deals with the behaviour of the flow that, while approaching the throat, accelerates on the internal wall of the lip. The third may represent in more detail the little divergence of the different meshing data.

Mesh	Coarse	Medium	Fine
Inlet Pressure Recovery	0.9424	0.9432	0.9438

TABLE 4.5: Convergence of the model

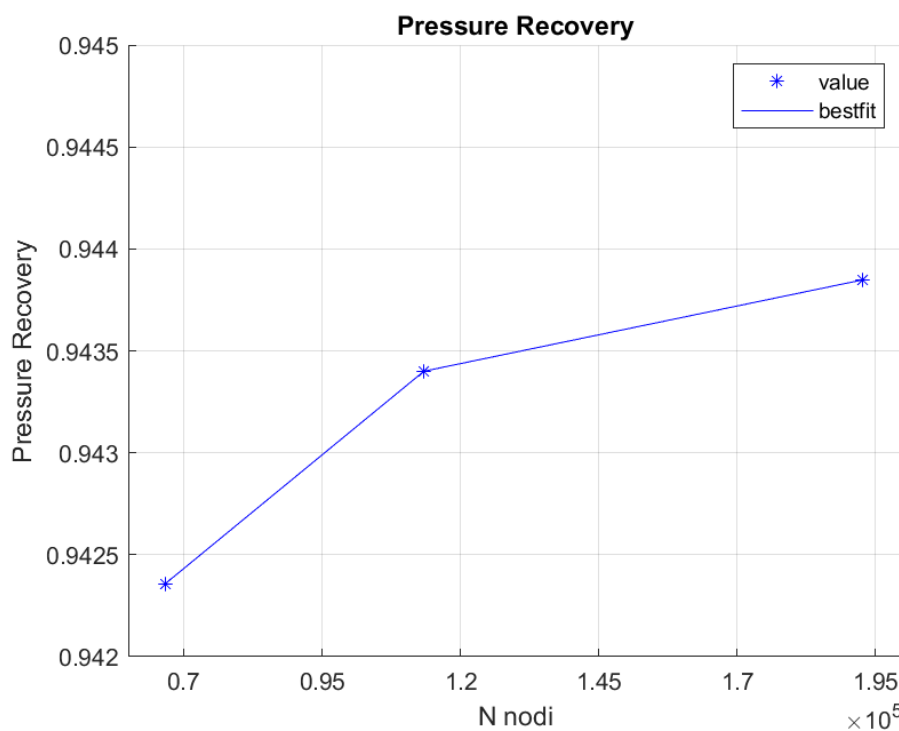


FIGURE 4.12: Inlet pressure recovery within coarse, medium and fine mesh (MFR=0.85, Design A)

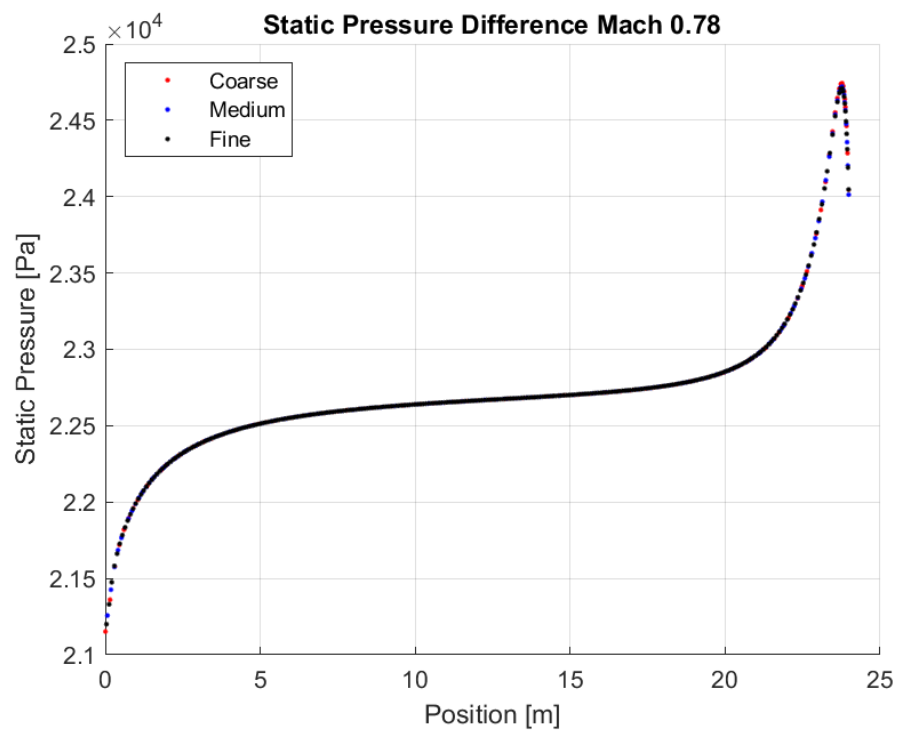


FIGURE 4.13: Static Pressure along the fuselage within coarse, medium and fine mesh (MFR=0.85, Design A)

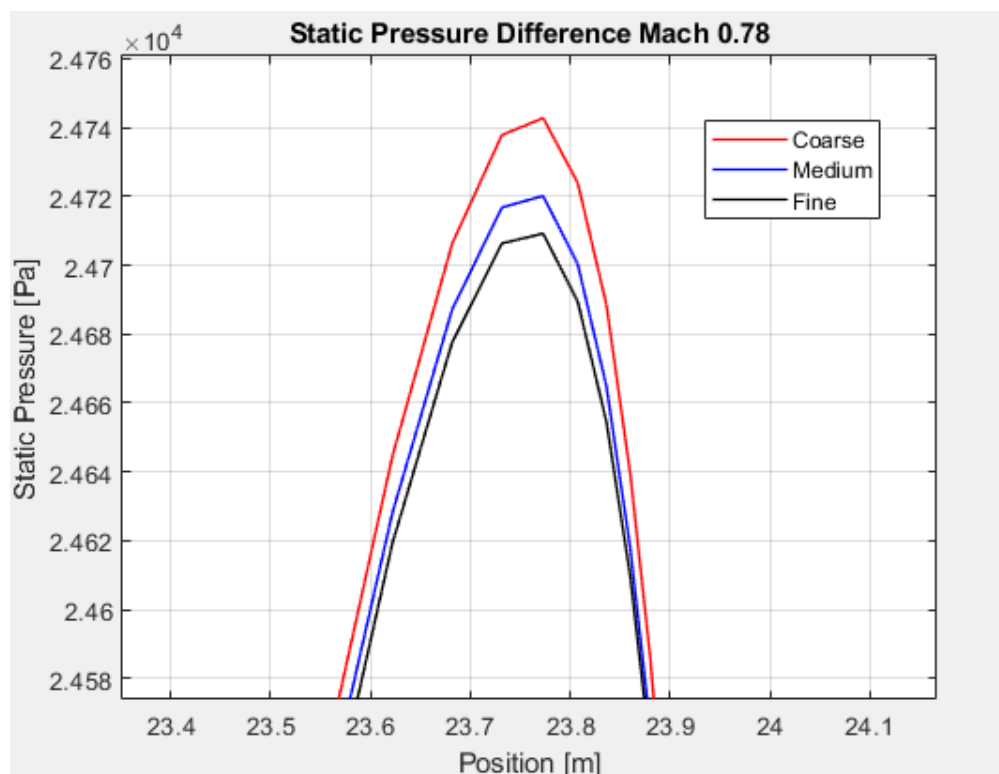


FIGURE 4.14: Difference in static pressure at the proximity of the inlet (roughly 24m) in coarse, medium and fine mesh. (MFR=0.85, Design A)

Less than 4% difference in static pressure can be observed between the medium and fine mesh, as well as between the medium and the coarse at the proximity of the inlet, at roughly 24 m along the fuselage. Further increase in mesh elements is expected to result in an even smaller change, and the result is converged.

Usually, smaller elements lead to more accurate results, but the computing time gets significant as well; for this reason, if by increasing the mesh element the output parameter shows no relevant changes, then the convergence is achieved, and the result is grid-independent. Further increase in total mesh element number would not generate changes in the results but only increasing the computational cost, thus unnecessary. The most optimum mesh can then be chosen as a verified mesh.

For accuracy purposes and since it showed reasonable simulation run time for the initial simulation, the medium mesh was selected to be used for the rest of the simulations.

4.5 Boundary Condition and Simulation Setup

Settings of the boundary conditions have followed the simulation run for Case 1 accounting for, in addition, the extension of the geometry leftward to the fuselage and of the S-duct.

The imposed boundary conditions to the BLI model were:

- *Wall* - four parts in the domain were applied with a no-slip and a smooth (adiabatic) wall condition. The nacelle, the fuselage and the curvature in the duct represent the viscous walls, while the dff and top part of the domain corresponds to the inviscid wall.
- *Pressure far-field* - the rounded face upstream of the domain was imposed with a pressure inlet condition. This allowed the boundary layer total pressure profile to be implemented to conduct the main study.

The gauge pressure was set to 22696 Pa that is equal to the absolute pressure since the operating pressure is set to 0 Pa far upstream of the domain. Mach number was kept to 0.78 and the temperature to the static value of 216.82 K.

- *Pressure outlet* - The face downstream of the domain and the outlet of the duct were applied with a pressure outlet condition. The gauge pressure was set to 22696 Pa and the temperature at 216.82 K and the average pressure specification was turned on.

In comparison with the first simulation, the *Wall* condition was thus set up for the surface of the intake, and the *Pressure-Outlet* condition was extended to the outlet of the duct.

For the parametric analysis, an approach that enables the definition of mass flow rate was also used in this case. The target mass flow rate sub-function was selected in order to force the mass flow rate at the outlet to reach a target chosen as a goal to achieve. In the pressure outlet dialogue box, it was required to specify the upper and the lower limit of absolute pressure. Specifying the range of the pressure limits improves convergence in cases with a large number of outlet boundaries, which have different pressure variations on different boundaries. However, there is a loss of reliability of the overall solution associated with this function as the flow velocity approaching sonic speed is automatically limited by the solver. Furthermore, this function is necessary to study low inlet mass flows.

Once completed the boundary conditions, the hybrid initialization was chosen to initialize the solver, and the external-aero favourable setting was also selected. Similarly to the previous simulation, the explicit relaxation factors have been set to 0.5 for momentum and pressure, while the under-relaxation factors were left at the default values. Besides, the global scale continuity residual value had to drop below at least three orders of size and all the other globally scaled residuals had to be less than a value of 10^{-6} to verify the convergence state of the solution.

Finally, the simulations were run, and the obtained results were used for the analysis.

4.6 CFD-Post and Results

The purpose of post-processing is to exploit the results acquired during the simulations. Here the goal is to assess the performance of the intake.

In this section, the flow behaviour around the intake is assessed; in particular, the boundary layer profile is calculated in several simulations characterized by mass flow ratios less than 1. The focus of the analysis is to determine how much boundary layer is ingested by the intake within different boundary conditions given at the outlet of the duct, and thus with different lip designs of the intake to study the pre-diffusion in terms of pressure recovery.

The majority of all the post-processing was conducted with the generation of several scripts in Matlab that helped in the extraction of the boundary layer profile and the collection of the results.

During this paragraph, the development of the procedure involved is described taking into account one case data as a point of reference for all the other cases and simulations. Each step will be explained in terms of implemented methodology and represented through the generation of graphics and contours. At the end of this part, the results will be summarized and collected in order to be discussed in the following Chapter.

4.6.1 Mass Flow Ratio (MFR)

The main varied parameter for each simulation was the mass flow ratio (MFR) because it has a considerable influence on all variables. For this study, it was accounted between two crucial cross-sectional areas of the geometry, namely the highlight area A_1 the area of the captured stream tube located where the calculation of the boundary layer has been carried out A_0 .

$$MFR = \frac{A_0}{A_1} \quad (4.5)$$

Whereas the highlight area was kept the same for all the simulations because it depended only on the design of the intake, the A_0 instead changed every time the boundary condition at the outlet of the duct has been changed. This variation determined globally 8 different MFRs, 4 relatives to the profile with the rounded elliptical lip (Design A) and 4 relatives to the thinner profile built with the Naca cowl coordinates for the external surface of the lip (Design B). MFRs are summarized in Table 4.6 and Table 4.7, respectively.

Design A	MFR=0.87	MFR=0.85	MFR=0.65	MFR=0.56
-----------------	----------	----------	----------	----------

TABLE 4.6: MFRs studied for Design A

Design B	MFR=0.98	MFR=0.97	MFR=0.67	MFR=0.56
-----------------	----------	----------	----------	----------

TABLE 4.7: MFRs studied for Design B

These MFRs were simulated, and the intakes for BLI were modelled and analyzed. The effect of the lip design, intake throat height, duct curvature and boundary layer profiles were studied. Figure 4.15 and 4.17 display the Mach number contour of two MFRs (0.97 and 0.56) and show the effect of a high and low MFR on the intake (Design B data) in the upstream region and then inside of the duct.

For low MFR, the pre-diffusion of the flow is considerable and a partial spillage of the air occurs: air is spilled outside the intake instead of being ingested into the engine face. This leads to a severe pressure loss due to the loss of energy of the slowed down flow, and an increase in the spillage drag that is an additional propulsion performance drawback for the inlet.

In Figure 4.16, this phenomenon can be observed by looking at the divergent stream tube of the flow through the *stream function* contour.

However, the contour also shows that the existence of low velocities due to the development of an adverse pressure gradient in the proximity of the inlet allows keeping an overall decelerated flow even inside the duct and at the AIP.

On the other hand, when MFR=0.97, the suction of the airstream reduces the δ as it produces a favourable pressure gradient. Upstream of the intake, the diffusion of the flow is weaker since the stream tube is almost cylindrical.

A less deviation of the streamlines is visible in Figure 4.18 through the *stream function* contour. The uniformity of the flow is conserved, leading to better pressure recovery.

However, in this case the flow accelerates through the intake and causes the development of a sonic bubble in the proximity of the throat. As can be seen, the supersonic condition is not achieved through the duct, because, the fact that the throat area is the minimum area within the duct is only a necessary but not sufficient condition to achieve the supersonic regime. Therefore, due to the pressure condition at the AIP, the sonic bubble hasn't affected the downstream region. This avoided the flow to accelerate again and prevented the duct from experiencing distorted flow that can cause engine damages or lead to engine stall out.

Generally, the intake design should be realized considering the right trade-off between the advantages and drawbacks of the variation of the mass flow ratio. The Table 4.8 gives a summary of the main consideration that can influence the intake design.

	MFR\sim1	MFR\ll 1
Positive Aspects	<ul style="list-style-type: none"> ·Less deviation of the streamlines of the flow: optimal shape of the stream tube ·Low pressure loss upstream of the intake ·Less spillage drag ·Overall higher efficiency 	<ul style="list-style-type: none"> ·Significant diffusion of the flow entering the intake ·Stability and uniformity of the flow at the AIP ·No supersonic velocities involved at the throat
Negative Aspects	<ul style="list-style-type: none"> ·Weak pre-diffusion ·High velocities inside the intake ·Instability of the flow at the AIP ·High pressure loss in-wall 	<ul style="list-style-type: none"> ·High spillage drag ·High pressure loss upstream of the intake ·Flow separation ·Secondary flows

TABLE 4.8: Influence of MFR on intake design

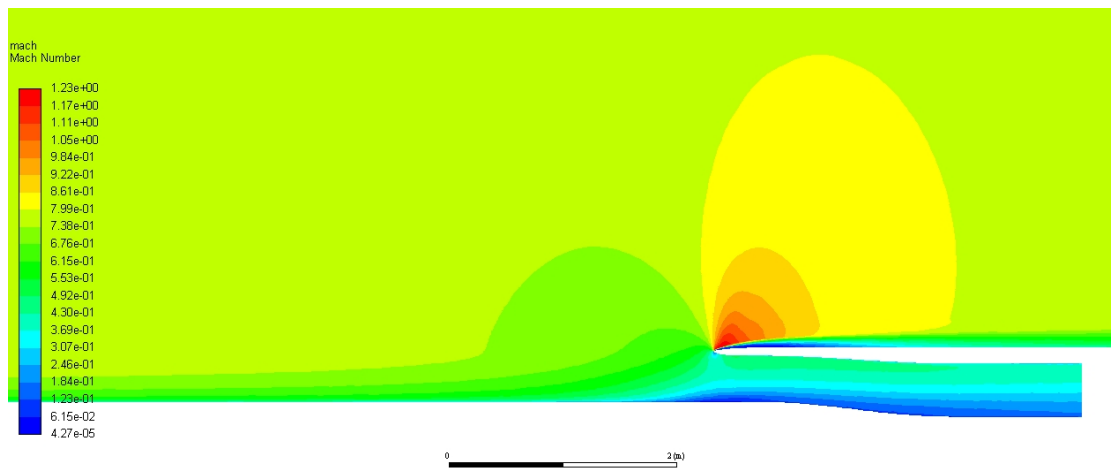


FIGURE 4.15: Mach Number Contour-MFR influence on the intake (Design B, AR=6, CR=1.10, M=0.78, $H_{throat}=0.4038$ m, MFR=0.56)

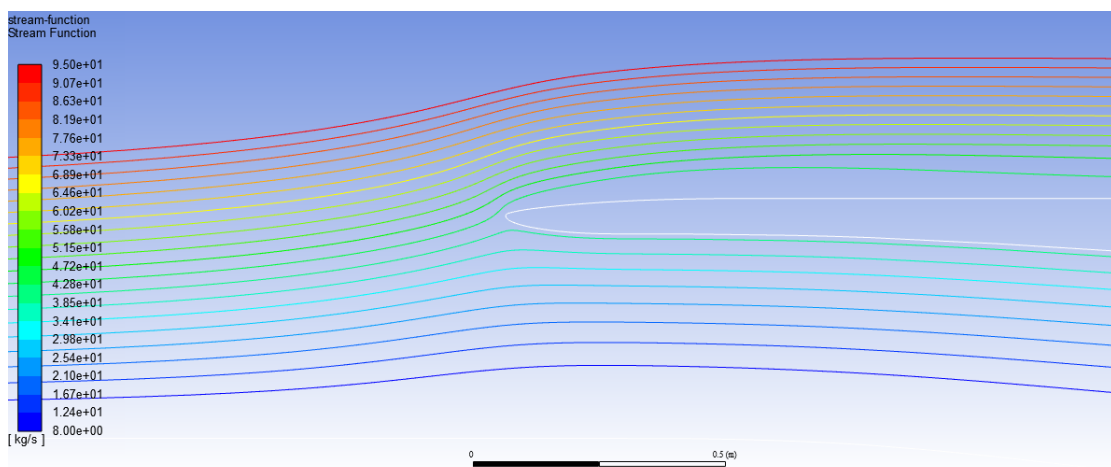


FIGURE 4.16: Contour of Stream Function (Design B, AR=6, CR=1.10, M=0.78, $H_{throat}=0.4038$ m, MFR=0.56)

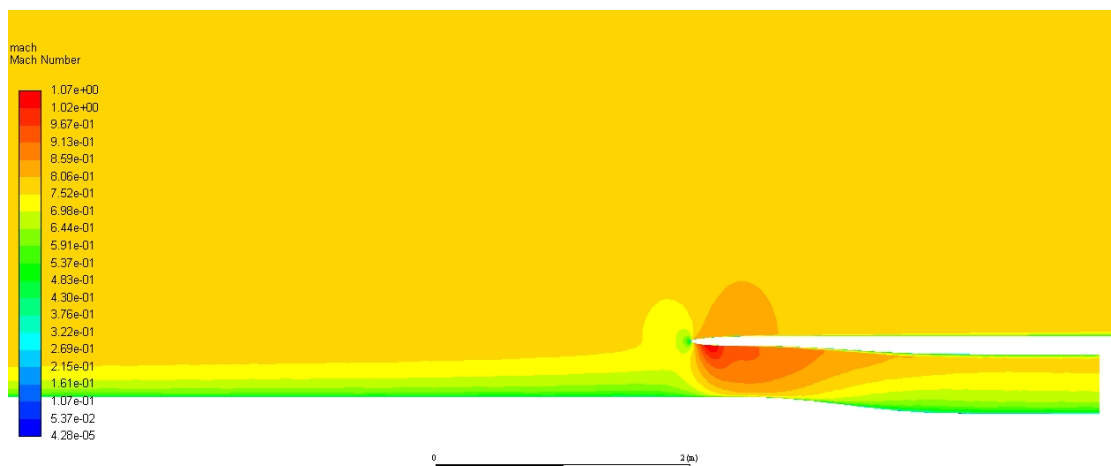


FIGURE 4.17: Mach Number Contour-MFR influence on the intake (Design B, AR=6, CR=1.10, M=0.78, $H_{throat}=0.4038$ m, MFR=0.97)

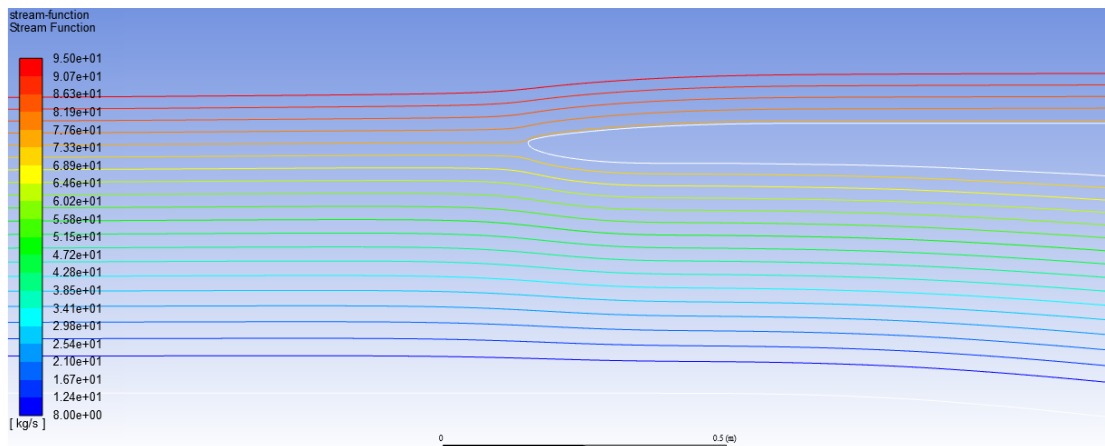


FIGURE 4.18: Contour of Stream Function (Design B, AR=6, CR=1.10, M=0.78, $H_{throat}=0.4038$ m, MFR=0.97)

4.6.2 Approach to the Analysis

In a BLI system, the presence of the nacelle facing the free stream affects tremendously the upstream flow moving over the surface of the fuselage. The interaction with the nacelle leads to a changeover of the flow in all its main thermodynamic and physical characteristics. Density, velocity, temperature, pressure and viscosity are subjected to a variation that has an impact on the behaviour of the flow ingested by the engine, and thus on the intake performance and efficiency.

Therefore, to counteract and prevent the possible losses and the penalty given by the existence of the nacelle, the intake design is fundamental.

For each intake design undertaken in this study, the first consideration made dealt with finding the location of a suitable interface point along the fuselage in a region upstream of the intake. This research aimed to consider a position where a consistent thickness of the boundary layer could be taken into account to evaluate its main properties.

The static pressure along the fuselage was assessed for this purpose. Firstly, it has been calculated for the baseline geometry (Case 1) and then compared to the one extracted from the geometry encompassing the intake (Case 2).

As expected, the outcome of this comparison showed a divergence between data in pressure. The development of the static pressure of Case 2 is influenced by the presence of the nacelle, and thus its path gradually diverged from the constant

growth of the pressure of clean fuselage (Case 1).

Therefore, to find out the opportune point describing the initial and relevant growth of the boundary layer, a divergence of 1.5% has been sought between the two evolutions of static pressure. Figure 4.19 illustrates this behaviour and the comparison between the two cases. The required position of 1.5% of divergence is also graphically visible.

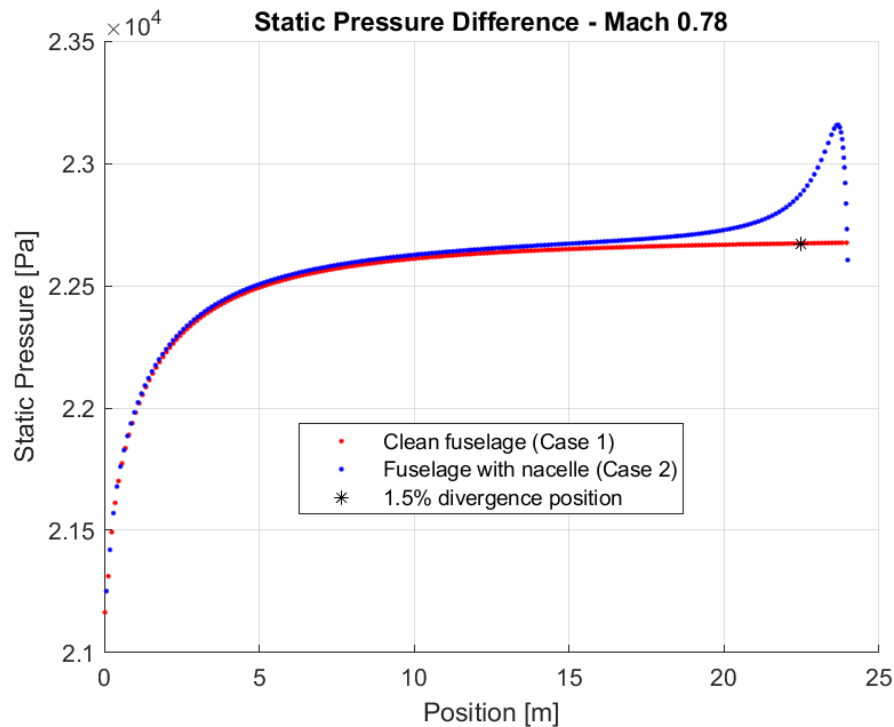


FIGURE 4.19: Static pressure comparison between the geometry of the clean fuselage and the geometry with the BLI system. Graphical representation of the point of divergence. (Design B, AR=6, CR=1.10, M=0.78, H_{throat} =0.4038 m, MFR=0.97)

Along with the static pressure, a focus was also given to the evolution of the pressure coefficient. It best shows the divergence of the static pressure due to the deceleration of the flow approaching the intake (roughly 24 m) and then a slight decrease in the proximity of the throat where the flow is supposed to accelerate.

Figure 4.20 gives an example of a pressure coefficient extrapolated from Design B at MFR=0.56 compared with the clean fuselage.

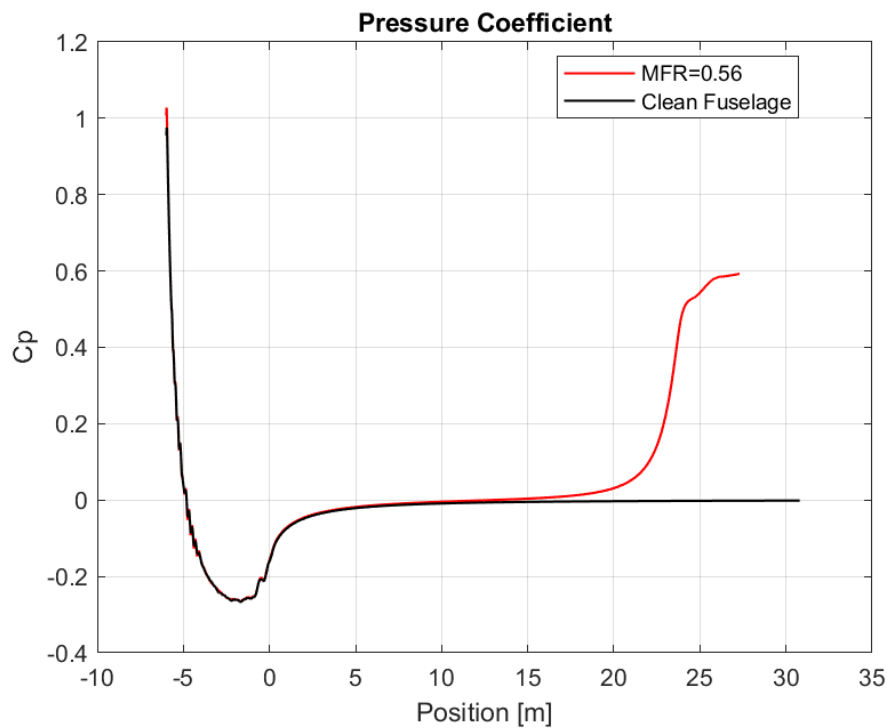


FIGURE 4.20: Comparison of the pressure coefficient of the clean fuselage and the geometry with the BLI system (Design B, AR=6, CR=1.10, M=0.78, $H_{throat}=0.4038$ m, MFR=0.56)

After deriving the point of divergence between the static pressure of the clean fuselage and the fuselage encompassing the nacelle, the next target dealt with the calculation of the area in this characteristic point through which the stream tube is approaching the intake.

To measure this area, a construction line was created in the x-coordinate of the point of divergence along the y-coordinate up to the height of the stream tube that can be visualized in the figure 4.21. The streamlines are computed to check the correct dimension of the ingested stream tube.

After the calculation of the annulus area, the MFR of the specific simulation has been evaluated.

The mass flow rate through this section has been assessed with the option *fluxes* in Fluent to verify and check the continuity of the mass flow.

The design of the intake had an influence on the value of the mass flow rate

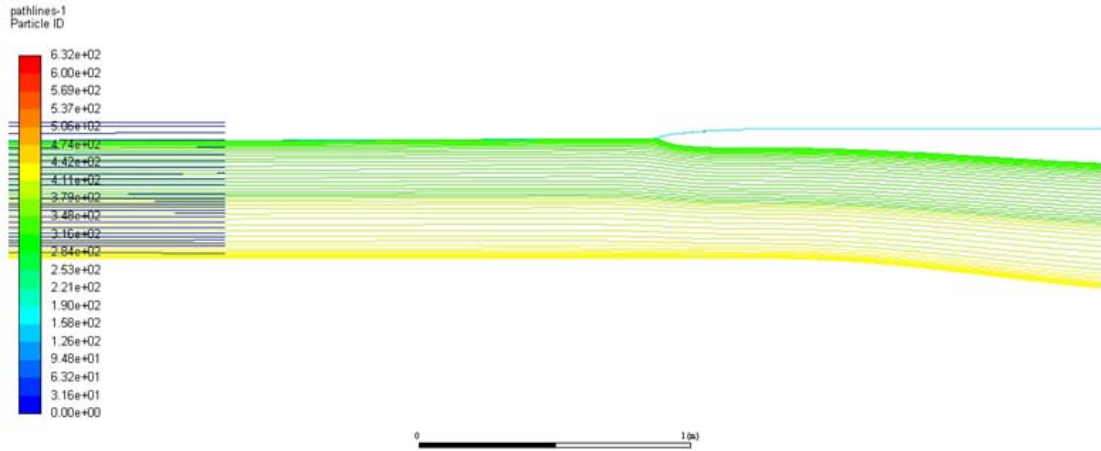


FIGURE 4.21: Streamline of the flow ingested (Design B, AR=6, CR=1.10, M=0.78, $H_{throat}=0.4038$ m, MFR=0.97)

involved in the simulation. To verify how much mass flow rate has been ingested by the intake respect to the total air moving along the clean fuselage, a mass flow rate ratio has been studied:

$$ratio_{out,cleanfus} = \frac{\dot{m}_{AIP}}{\dot{m}_{cleanfuselage}} \quad (4.6)$$

With this equation, the percentage of how much mass flow rate goes through the duct respect to the free stream can be derived. This allows understanding how the construction of the intake can affect the behaviour of the flow upstream, the spillage of air and then the condition of the flow at the interface with the fan.

The next crucial step dealt with the calculation and the extraction of the boundary layer profile in the region of interest determined by the point of divergence.

The procedure adopted was the same described in Section 3.5.1, where the writing of a journal file through a script created in Matlab provided the correct session files to implement in the solver.

A journal file contains a sequence of Ansys Fluent commands, arranged as they would be typed interactively into the program and recorded as scheme code lines.

[46] This record and playback tool has enabled the generation of a *Rake – surface*

upstream of the intake and, therefore, the evaluation of the thickness of the boundary layer up to the location of the point of divergence.

It mainly consisted of a set of construction lines built with a step of 0.0625 m from the x-coordinate 0 to the x-coordinate of the point of divergence and with a height of a symbolic y-coordinate chosen to be far enough from the surface of generation to ensure the full visualization of the boundary layer profile.

Figures 4.22 and 4.23 give an example of what explained. In particular, the first one displays the boundary layer profile, from the nose to roughly 24 m of fuselage, calculated interpolating the velocity data and extracting the 99% of the free stream velocity for each set of 1000 points drawn by the *Rake – surface*. The second one shows the boundary layer velocity profile at the point of divergence ~ 19 m.

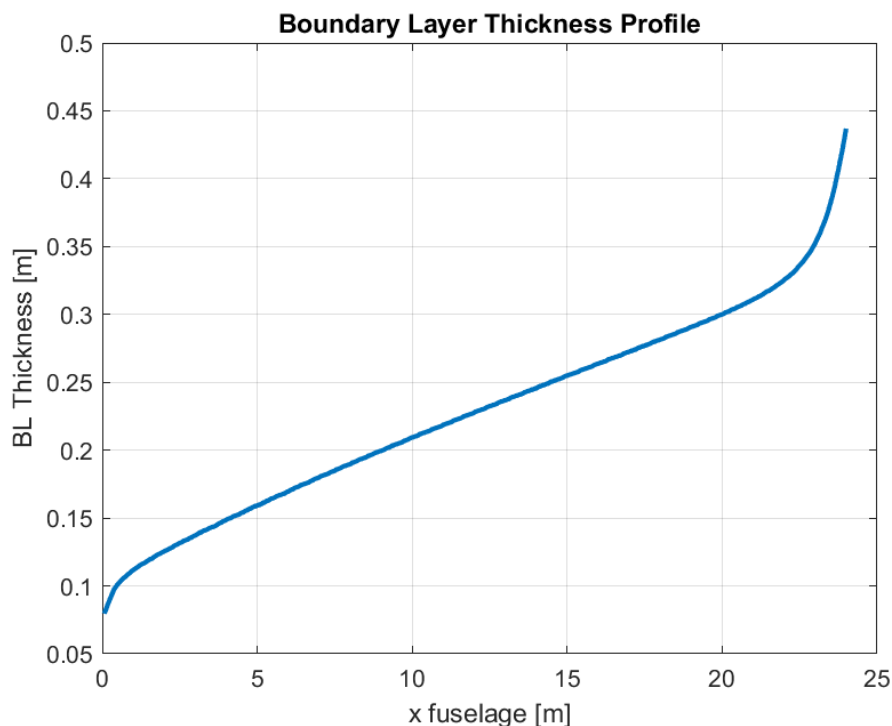


FIGURE 4.22: Boundary layer thickness profile from the nose to roughly 24 m (Design B, AR=6, CR=1.10 M=0.78, H_{throat} =0.4038 m, MFR=0.56)

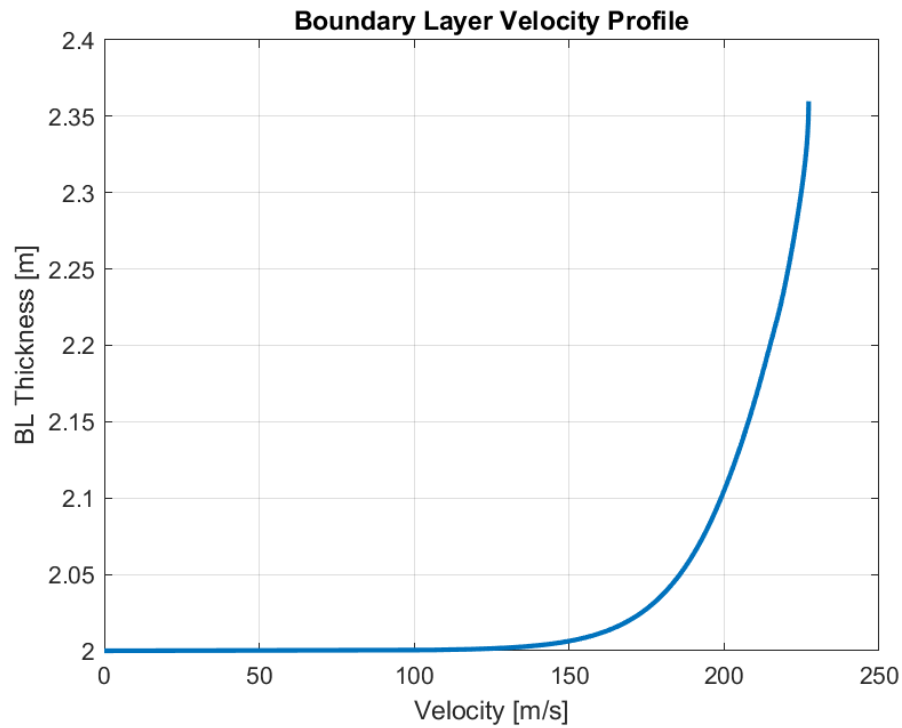


FIGURE 4.23: Boundary layer velocity profile at the point of divergence (roughly 19 m) (Design B, AR=6, CR=1.10, M=0.78, $H_{throat}=0.4038$ m, MFR=0.56)

As can be seen from the first figure, the boundary layer increases its thickness approaching the intake due to the growth of the Reynolds number, as expected from the theory of the flat plate described in Section 2.2.2.

In the proximity of the leading edge, the Reynolds number is very low, the boundary layer is attached to the surface and the thickness is negligible. No differences can be found in terms of external and internal boundary layer solution at this point. At a certain distance, the scale factor passes from 1 to 100 in terms of Reynolds number and the complete solution can be split into an external solution and a boundary layer solution. When Reynolds number increases over the value of 10^6 turbulence occur. The diameters of vortices develop considerably, affecting the thickness of the boundary layer.

About the equation defining the thickness of the boundary layer (2.10), the rationalization of it strengthens the concept of how the thickness of the boundary layer depends on the characteristic parameter x , and thus on the Reynolds number.

$$\delta(x) = \sqrt{\frac{x\nu}{U}} \quad (4.7)$$

Approaching the end of the fuselage, the boundary layer grows as x increases.

The last phase of the analysis consisted of the assessment of the mass flow rate passing through this thickness in order to understand how much boundary layer is ingested by the intake respect to the free stream.

To do this, another construction line has been created in the x -coordinate of the point of divergence and up to the height of the characteristic thickness of the boundary layer. Then with the *fluxes* option in Fluent, the mass flow rate has been derived $\dot{m}_{\delta BL}$. The percentage of boundary layer ingested has been calculated with the following equation:

$$\%BL = \frac{\dot{m}_{AIP}}{\dot{m}_{\delta BL}} \quad (4.8)$$

Once extrapolated all this data, the behaviour of the flow has been highlighted, especially at the AIP. The development of the Mach number, as well as of the static pressure, have been estimated and displayed. At last, the pressure recovery has been studied in the upstream region of the intake and inside of the duct, varying the MFRs.

All this process has been followed for both the models investigated in this study. The variation in MFR ($MFR < 1$) has been considered as the starting point for all the simulations to run. A changing of the boundary condition at the outlet of the duct allowed to vary it. In the next chapter, the results obtained from all the simulations are collected and discussed.

Chapter 5

Results and Discussion

In this chapter, the CFD results are summarized and then shown for both the configurations studied. Firstly, the investigation conducted on Design A is introduced with a schematic representation of the geometry and a table of the main results. All the procedure is repeated for 4 simulations varying the boundary condition at the outlet of the duct by choosing a target mass flow rate in the *Pressure-outlet* condition. Later, the same pattern is used for Design B.

In addition to all the parameters assessed, some contours are displayed to help to visualize the results. In the last part of the chapter, a particular focus is given to the assessment of the pressure recovery and its relationship with different MFRs for the two different designs.

5.1 Results of the Elliptical Lip (Design A)

As described in the previous chapter, the first consideration for this model has been done relative to the evolution of the static pressure along the fuselage in order to determine the location of the point of divergence \bar{x} . Here, the height and thus the annulus area of the stream tube ingested by the intake has been calculated characterizing the MFR. After extracted the thickness of the boundary layer in \bar{x} , the mass flow rate through it has been assessed.

At last, accounting for the different mass flow ratios for each simulation, the percentage of boundary layer ingest has been determined.

The following Table 5.1 summarizes all the results derived from 4 simulations and Figure 5.1 displays a schematic representation of the reference geometry with the main parameters involved in the analysis.

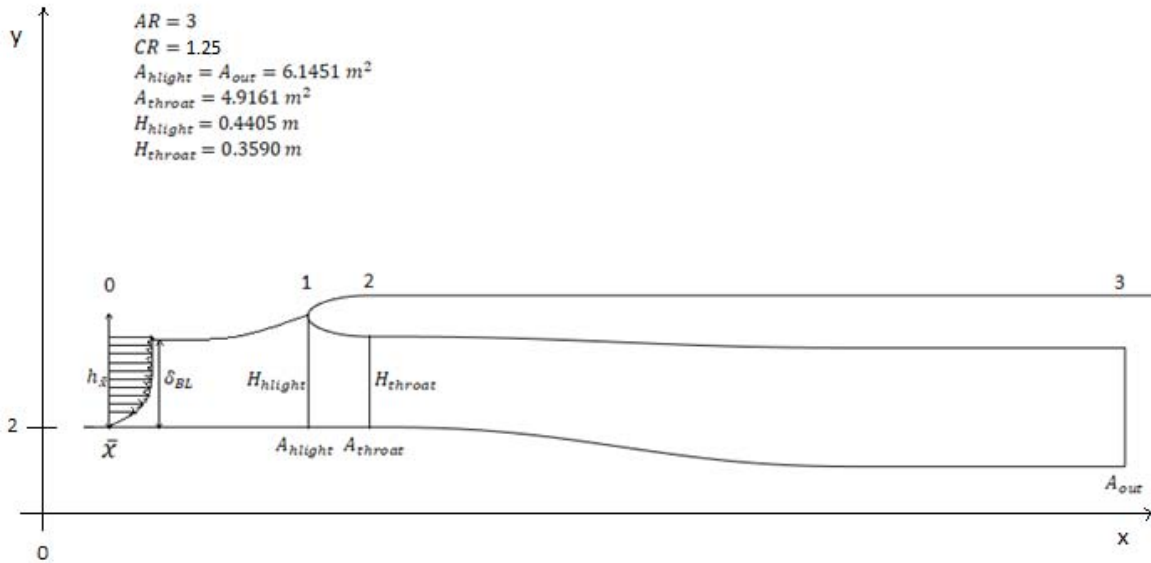


FIGURE 5.1: Schematic representation of Design A

Parameters	MFR=0.87	MFR=0.85	MFR=0.65	MFR=0.56
\bar{x}	20.7206 m	20.7206 m	19.6196 m	19.1792 m
\dot{m}_{target}	470.2904 kg/s	None	300 kg/s	250 kg/s
\dot{m}_{out}	400.8394 kg/s	400.7 kg/s	300 kg/s	250.1009 kg/s
$h_{\bar{x}}$	0.3907 m	0.3810 m	0.3 m	0.2606 m
$A_{h\bar{x}}$	5.3892 m ²	5.2438 m ²	4.0527 m ²	3.4881 m ²
δ_{BL}	0.3189 m	0.3189 m	0.3097 m	0.3054 m
$\dot{m}_{\delta_{BL}}$	320.0367 kg/s	320.0367 kg/s	310.0275 kg/s	305.193 kg/s
$ratio_{outcleanfus}$	0.852	0.852	0.637	0.5318
%BLI	100	100	96.7	81.9
M_{aveout}	~ 1	~ 0.7	~ 0.5	~ 0.4

TABLE 5.1: Main results Design A

All the simulations have been run under the same boundary conditions. However, apart from the baseline simulation (MFR=0.85), the definition of the mass flow rate was also used as a target to achieve at the outlet of the duct.

Firstly, the aim was to compare the quantity of the air approaching the suction of the intake concerning the mass flow rate passing over the clean fuselage design. The baseline simulation pointed out this comparison: no target in mass flow rate has been set to define the initial MFR(~ 0.85), resulting in a mass flow rate at the outlet of the duct of a lower value of the 85% of that characterizing the clean fuselage.

Secondly, in the 1st simulation, the mass flow rate was forced to achieve the same value of that one of the clean fuselage resulting in a higher MFR=0.87. Both the cases show the same Mach number at the throat that reached the sonic condition causing the duct to choke. A further tentative to increase the mass flow rate (1st simulation) failed because the mass flow rate that led to the choking was the maximum achievable within the duct.

For this reason, the outcomes are mainly the same as the baseline, and besides, an insurgence of higher velocities within the duct can be highlighted. The development of the Mach number in the proximity of the throat can be seen in Figure 5.2, where the baseline simulation and the 1st give the same result.

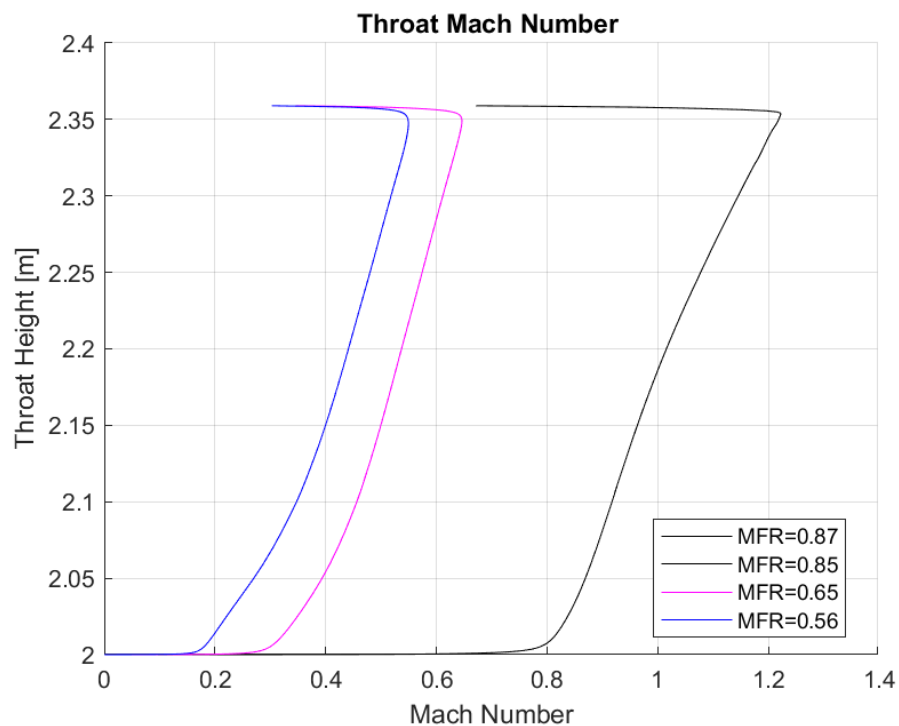


FIGURE 5.2: Mach numbers at the throat of the duct (Design A)

Then, the goal was to decrease the MFR to study the pre-diffusion upstream of the intake and make a comparison in terms of the pressure recovery within the duct. The 2nd (MFR=0.56) and the 3rd (MFR=0.65) simulations deal with a lower target in mass flow rate to be accounted for.

Diminishing the MFRs resulted in a decrease in velocity even upstream of the intake, where an adverse pressure gradient characterized the flow. The pre-diffusion in these cases is more significant than to higher MFRs because the presence of a more divergent stream tube that decelerates the upstream flow. Analyzing the comparison between the different boundary layer thicknesses, this concept can be furthermore strengthened.

As expected from theory, a thinner thickness of the boundary layer is visible for all the cases in the proximity of the leading edge, where accounting for the internal solution of the boundary layer, the Reynolds number is supposed to be lower (laminar flow). (Reference to Section 2.2.2)

The theory fails after the point of divergence from where the presence of the nacelle strongly affects the shape of the approaching stream tube, depending on the different mass flow ratios accounted. For high MFRs, the flow is more flattened to the surface, and the stream tube takes almost the shape of a cylindrical tube that decreases the impact the nacelle has on the flow. This means finding a point of divergence closer to the inlet, and leads to a lower pre-diffusion in front of the intake.

The things change by assuming a lower MFR since a more divergent stream tube upstream of the intake occurs, the more the MFR decreases. In these cases, the existence of the nacelle influences more powerfully the thickness of the boundary layer pushing the point of divergence further back and raising the curve to a higher position. The difference of 1.5% in static pressure occurs earlier along the fuselage, and the pre-diffusion becomes more relevant.

Figure 5.3 displays the difference of boundary layer profiles that become evident after the point of divergence for each simulation.

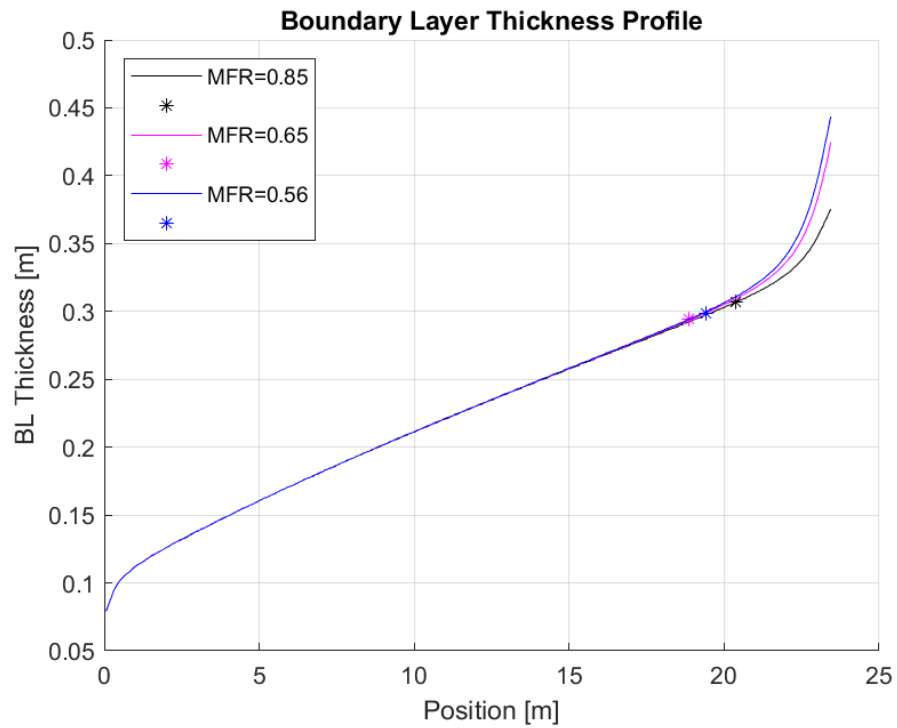


FIGURE 5.3: Boundary layer thickness profiles (Design A)

Relative to the point of divergence \bar{x} , the following Figure 5.4 shows the development of the static pressure along the fuselage for different MFRs highlighting the growth of the static pressure due to the adverse pressure gradient that occurs upstream of the intake. Both the Figures 5.3 and 5.4 point out the presence of a pre-diffusion which becomes larger for lower MFRs. The contours of static pressure in Figure 5.5 and 5.6 help displaying this great difference of flow behaviour in front of the intake and then inside the duct, through the comparison between MFR=0.85 and MFR=0.56.

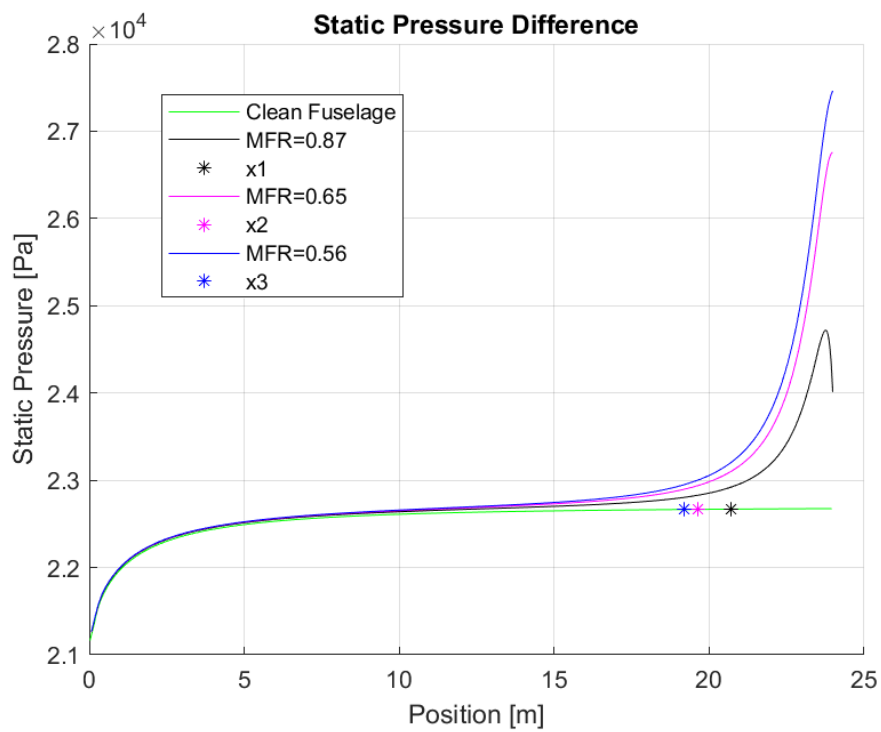
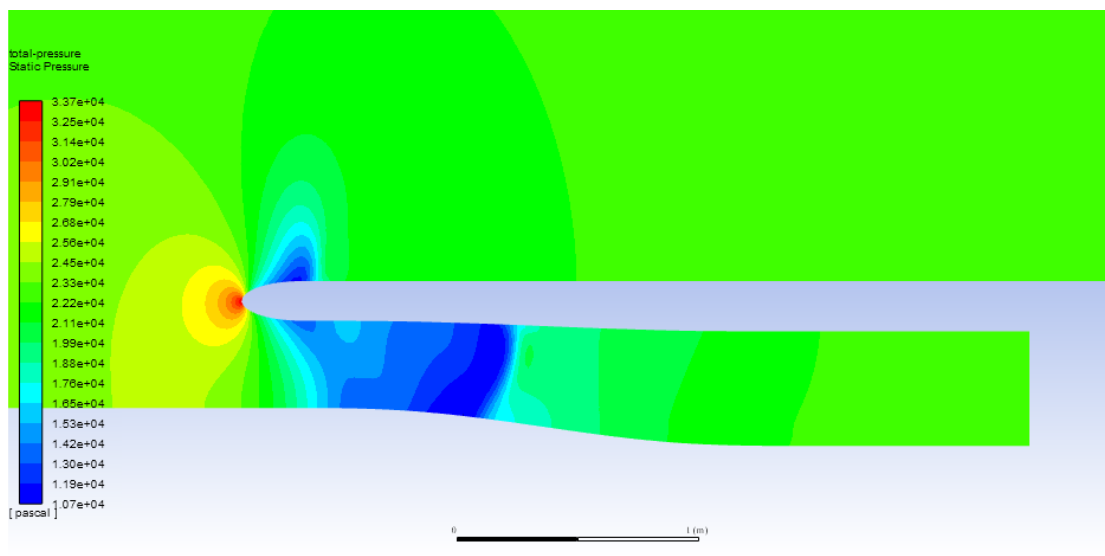


FIGURE 5.4: Static Pressure along the fuselage (Design A)

FIGURE 5.5: Static Pressure Contour (Design A, AR=3, CR=1.25, M=0.78, $H_{throat}=0.3590$ m, MFR=0.85)

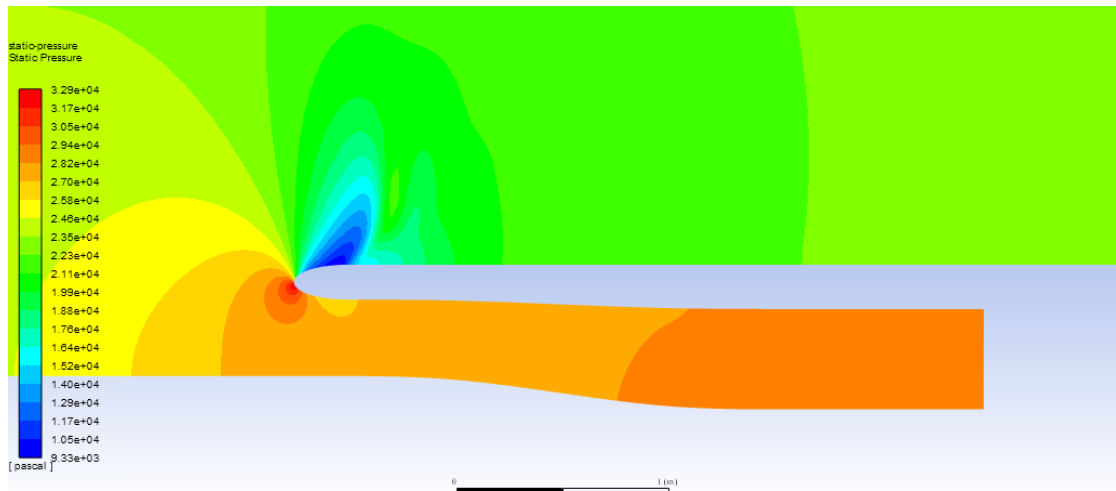


FIGURE 5.6: Static Pressure Contour (Design A, AR=3, CR=1.25, M=0.78, $H_{throat}=0.3590$ m, MFR=0.56)

Another parameter that must be taken into account is the Mach number calculated at the outlet of the duct. From results, an increase in Mach number can be progressively seen concerning the MFRs.

Decreasing the velocity for lower MFRs means a lower Mach number at the outlet of the duct. The S-duct design prevented from reaching Mach number higher than the far-field value (M=0.78); in fact, remembering that the outlet area is equal to the highlight area, the Mach numbers were expected to be always less or even equal to 0.78.

This condition is not respected in the 1st simulation for MFR=0.87, where a spread supersonic condition is verified due to the forcing in mass flow rate. The analysis showed that the flow choked as the flow accelerated to a $M \simeq 1.0$, resulting in a heavily unstable flow at the AIP.

For MFR=0.85 instead, a supersonic flow is reached, but then recovered right after the throat up to a preferable AIP Mach number of ($M \sim 0.7$). However, the rapid and sudden diffusion after the high velocities involved at the throat led to slight flow separation, especially at the first bend of the duct. This condition negatively affected the stability and the uniformity of the flow and locally developed high-pressure loss. This phenomenon can be visualized through the axial velocity vectors, drawn in this critical region, in Figure 5.8.

A lower but still acceptable AIP Mach number came out from the 3rd simulation for a MFR=0.65 ($M \sim 0.5$). In this case, the lower MFR ensured a bigger pre-diffusion and avoided reaching supersonic conditions inside the duct, and keeping the AIP Mach number higher enough to prevent flow from separation.

The following Figure 5.7 displays the different Mach numbers at AIP for different MFRs, and focusing on the cases of MFR=0.85 and MFR=0.56, the two contours of the development of Mach number in the whole duct can be visualized in Figures 5.8 and 5.9, respectively.

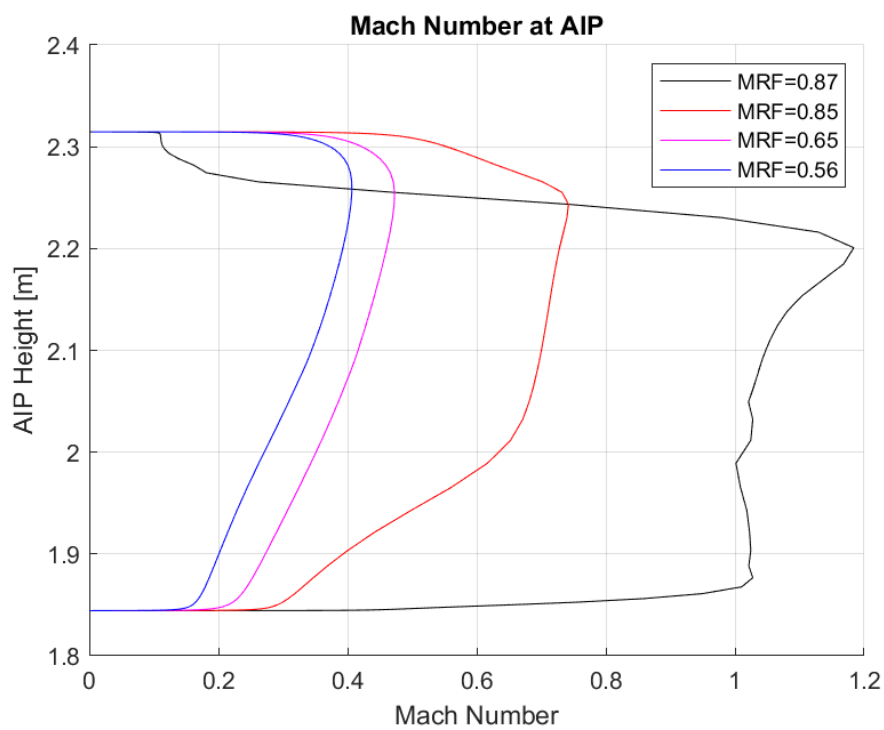


FIGURE 5.7: Comparison of Mach Number at the AIP (Design A)

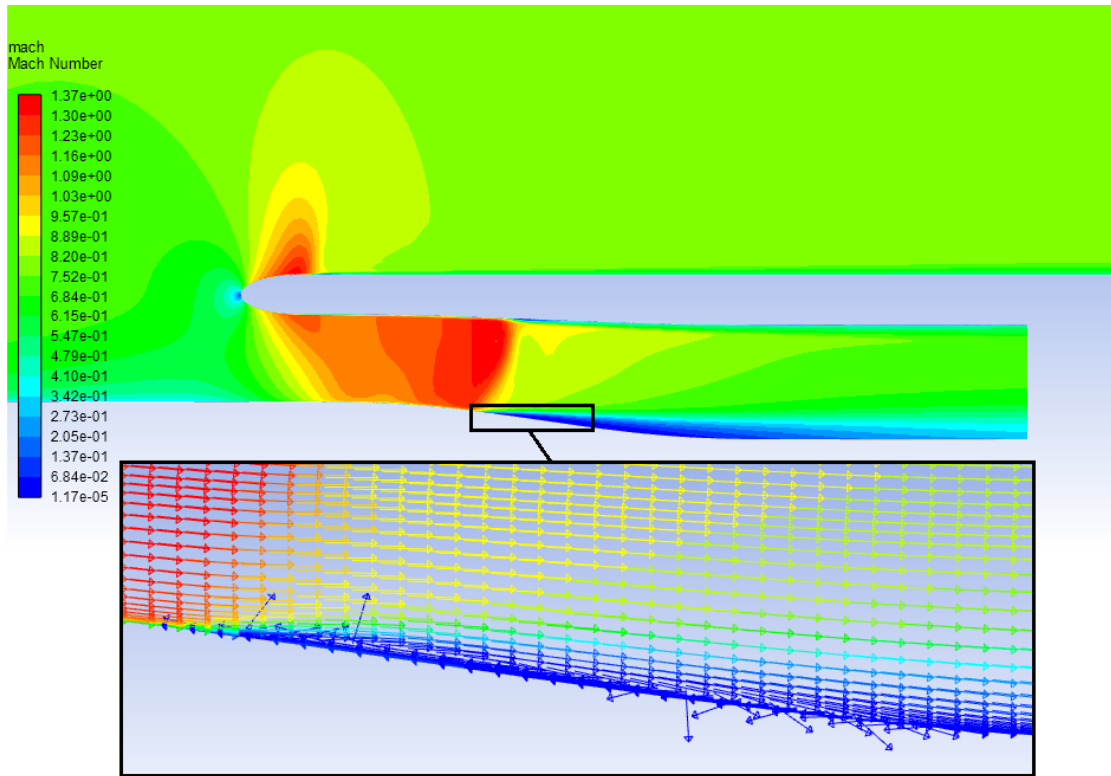


FIGURE 5.8: Mach Number Contour (Design A, AR=3, CR=1.25, M=0.78, $H_{throat}=0.3590$ m, MFR=0.85)

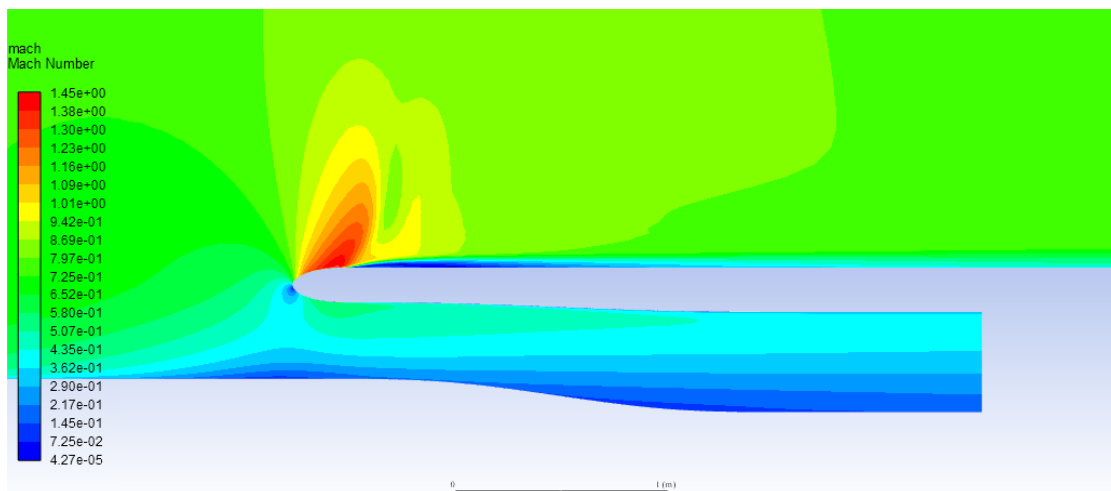


FIGURE 5.9: Mach Number Contour (Design A, AR=3, CR=1.25, M=0.78, $H_{throat}=0.3590$ m, MFR=0.56)

As can be deduced, the mass flow ratio controls a lot of important parameters assessed in the analysis. Its variation had a very strong influence also in the determination of the percentage of flow ingested.

According to what explained in section 2.6.4, at high MFR ~ 1 the stream tube in the pre-diffusion region assumes almost a cylindrical shape, all the flow is ingested, and a very low quantity of spillage occurs. In this case, all the thickness of the boundary layer is ingested (100%) and, in addition, 25% of the free stream because the streamline height is higher than the thickness of the boundary layer.

On the other hand, $MFR \ll 1$ characterizes a divergent stream tube upstream of the intake, spillage increases and the δ_{BL} reaches heights bigger than the stream tube, resulting in partial ingestion of the boundary layer. However, for $MFR=0.65$, the percentage of boundary layer ingested is $\sim 96\%$, thus almost the total thickness while ensuring the uniformity of the flow at the AIP.

The following Figure 5.10 illustrates the percentage of boundary layer ingested respect to the variation of mass flow ratio.

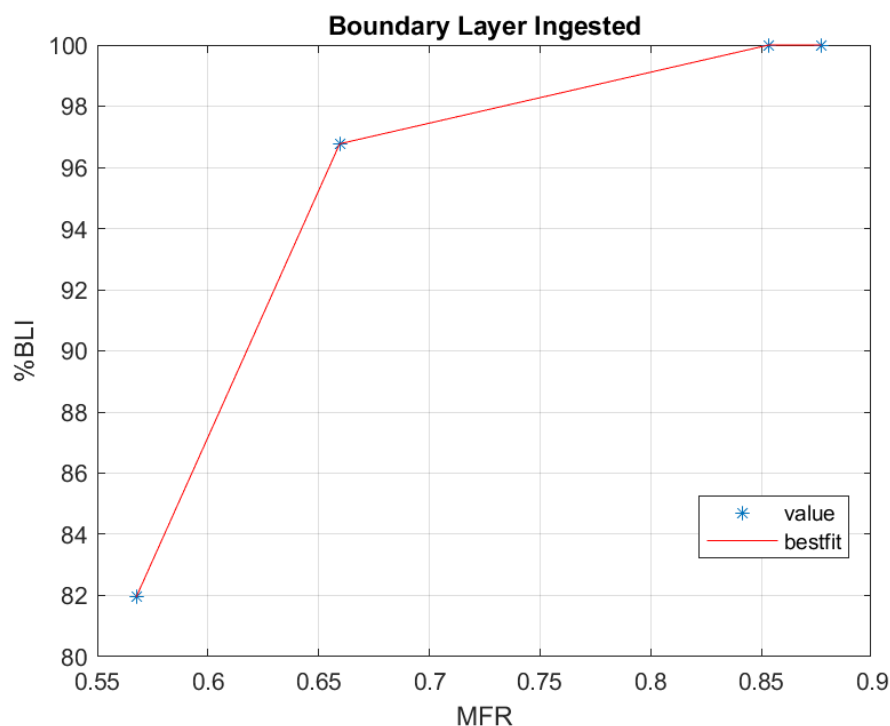


FIGURE 5.10: Percentage of boundary layer ingested respect to the variation of MFR (Design A)

5.2 Results of the Naca Cowl and $\frac{1}{4}$ Ellipse Lip (Design B)

The same approach has been taken for the second design assessed in this project. The following Table 5.2 summarized all the results derived from 4 simulations and the below Figure 5.11 displays a schematic representation of the reference geometry with the main parameters involved in the analysis.

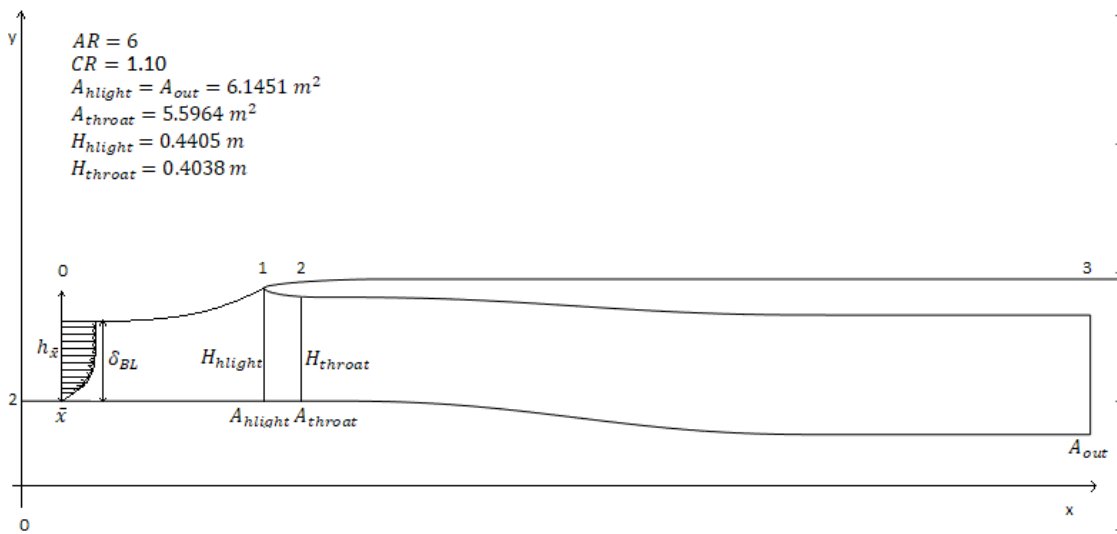


FIGURE 5.11: Schematic representation of Design B

Parameters	MFR=0.98	MFR=0.97	MFR=0.67	MFR=0.56
\bar{x}	22.7022 m	22.4821 m	20.1701 m	19.5095 m
\dot{m}_{target}	470.2904 kg/s	None	300 kg/s	250 kg/s
\dot{m}_{out}	460.4307 kg/s	456.0927 kg/s	299.579 kg/s	250.0025 kg/s
$h_{\bar{x}}$	0.4341 m	0.4313 m	0.337 m	0.2604 m
$A_{h\bar{x}}$	$6.0471 m^2$	$6.0043 m^2$	$4.1061 m^2$	$3.4853 m^2$
δ_{BL}	0.3359 m	0.3341 m	0.3143 m	0.3084 m
$\dot{m}_{\delta_{BL}}$	338.3643 kg/s	336.6448 kg/s	316.018 kg/s	308.532 kg/s
$ratio_{outcleanfus}$	0.979	0.969	0.637	0.5316
%BLI	1	1	0.951	0.8103
M_{aveout}	~ 1	~ 0.77	~ 0.5	~ 0.4

TABLE 5.2: Main results Design B

Like the previous analysis, no target in mass flow rate has been set in the baseline simulation, and the initial MFR (~ 0.97) resulted in a mass flow rate at the outlet of the duct of a value lower of the 3% of that one characterizing the clean fuselage. In the 1st simulation (MFR=0.98), forcing the mass flow rate at the outlet of the duct to reach the same value of that one of the clean fuselage resulted in a higher MFR almost achieving the target. Similarly to Design A, the duct is choked at the throat, but in addition a supersonic flow is then reached and kept till the AIP. The 1st simulation mainly gave back similar outcomes with respect to the baseline, while a tremendous increase in velocity characterized the whole duct. Later, decreasing the MFRs almost the same behaviour of the flow found with Design A occurred.

Accounting for a thinner lip of the intake, the presence of the nacelle less influenced the upstream flow in comparison with the rounded lip of Design A. This, especially for the baseline simulation, led to a MFR very close to the unity (MFR=0.97) and thus a very flattened flow to the surface appeared. The low impact of the nacelle on the approaching flow pushed the point of divergence very forward and closer to the inlet. Here, the annulus area is almost equal to the highlight area, shaping an almost cylindrical stream tube which consequently limited the spillage air and ensured the complete ingestion of the boundary layer.

Differently, by lowering the MFR, the pre-diffusion becomes more relevant and the point of divergence is moved further back, at a distance, however, closer to the inlet respect to the rounded lip case.

A representation of the different boundary layer thicknesses is given in Figure 5.12, where the highest curve represents the case of the lowest MFR, while the lowest curve relates to the highest MFR.

The development of the static pressure along the fuselage for different MFRs is also visible in Figure 5.13 highlighting the growth of the static pressure due to the adverse pressure gradient that occurs upstream of the intake that is larger for lower MFRs.

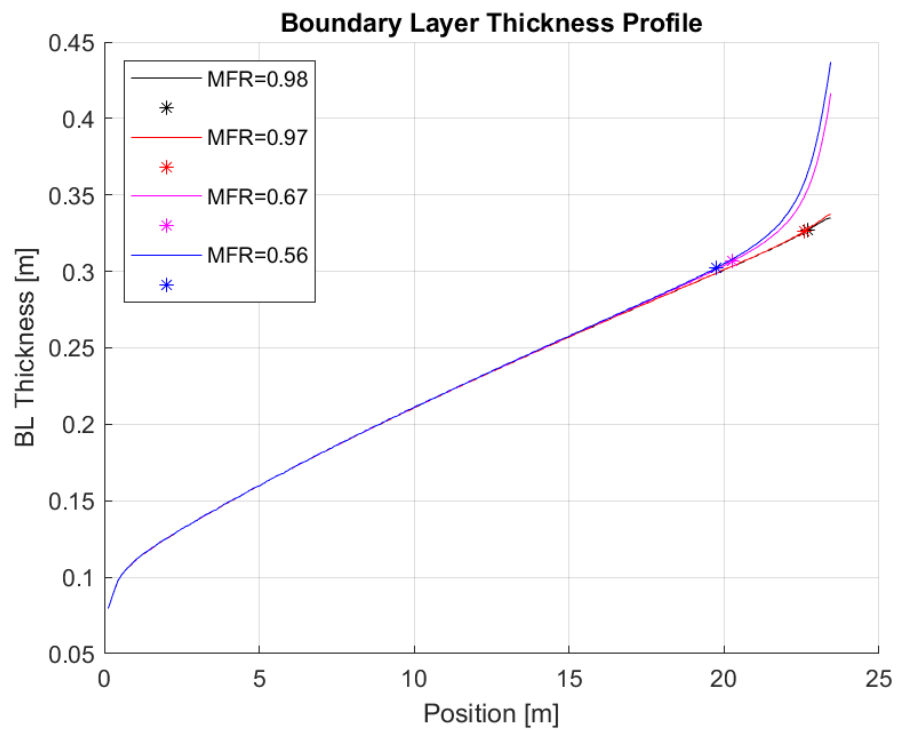


FIGURE 5.12: Boundary layer thickness profiles (Design B)

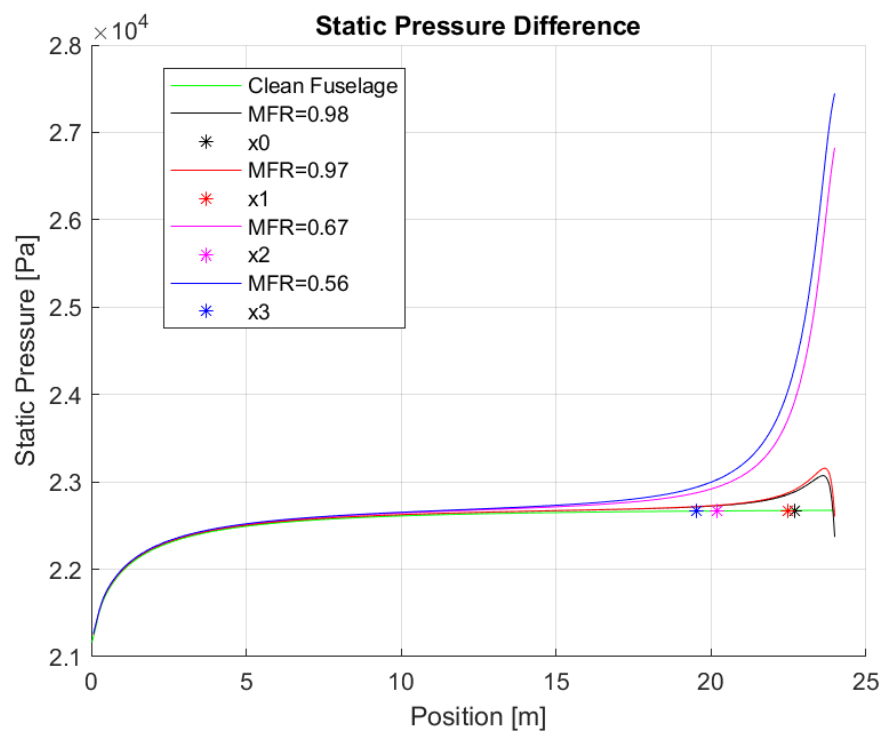


FIGURE 5.13: Static Pressure along the fuselage (Design B)

The contours of static pressure in Figures 5.14 and 5.15 help displaying the strong difference of flow behaviour for $MFR=0.97$ and $MFR=0.56$ in front of the intake and then inside the duct.

For $MFR=0.97$, the static pressure at the throat doesn't drop to the point that induces the flow to become supersonic. This can be due to the fact that, in this configuration, the throat height is bigger, making the lip duct less convergent than the Design A, where the rounded lip induces the flow to accelerate more.

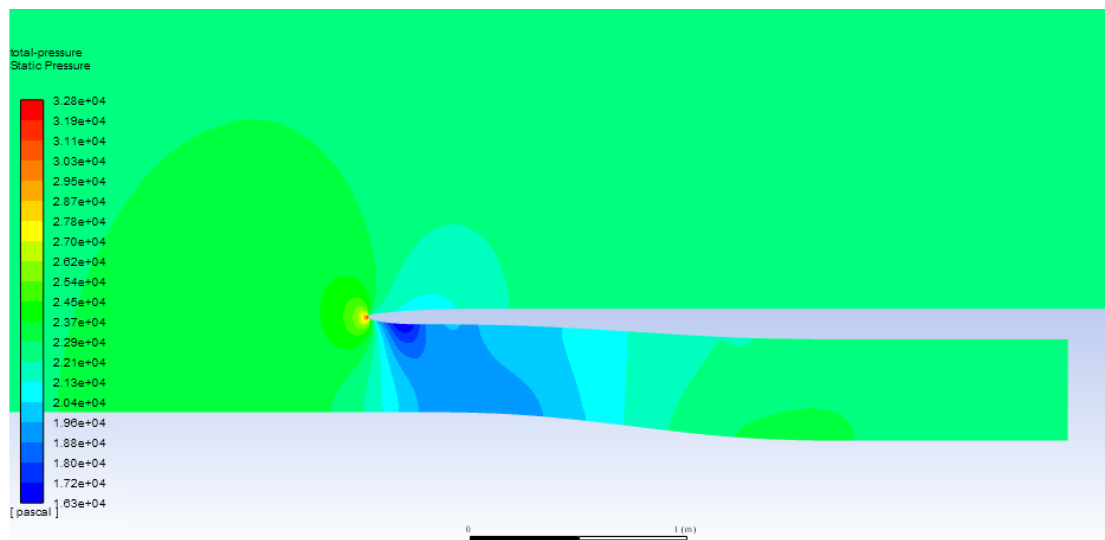


FIGURE 5.14: Static Pressure Contour (Design B, $AR=6$, $CR=1.10$, $M=0.78$, $H_{throat}=0.4038$ m, $MFR=0.97$)

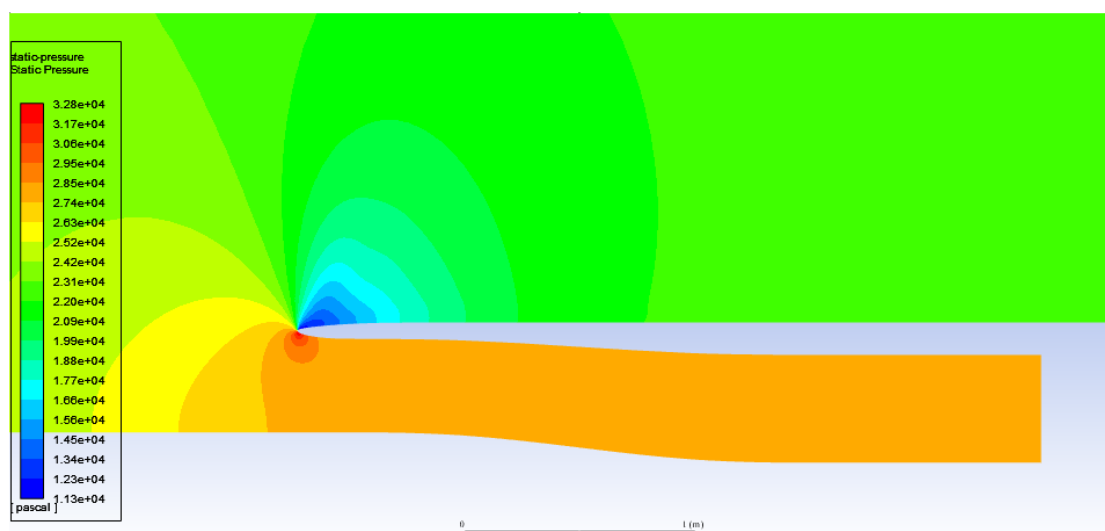


FIGURE 5.15: Static Pressure Contour (Design B, $AR=6$, $CR=1.10$, $M=0.78$, $H_{throat}=0.4038$ m, $MFR=0.56$)

Accounting for the Mach number at AIP, an increase of this important parameter can be progressively seen with respect to the MFRs.

Similarly to the previous case, the S-duct design prevents from reaching Mach number higher than the far-field value ($M=0.78$) apart from the 1st simulation where the target mass flow rate is forced to a higher value. In this case, supersonic values of the flow are achieved at the outlet, while at the throat a sonic bubble is generated due to the strong acceleration of the flow for $MFR=0.97$.

On the other hand, lower MFRs avoid the insurgence of the supersonic condition and the flow at the outlet remains highly subsonic. The development of the Mach number inside the S-duct is displayed in Figure 4.15 and 4.17 and described in section 4.6-1, considering $MFR=0.97$ and $MFR=0.56$. The following Figures 5.16 and 5.17 display the different Mach numbers at the AIP and at the throat for different MFRs, respectively.

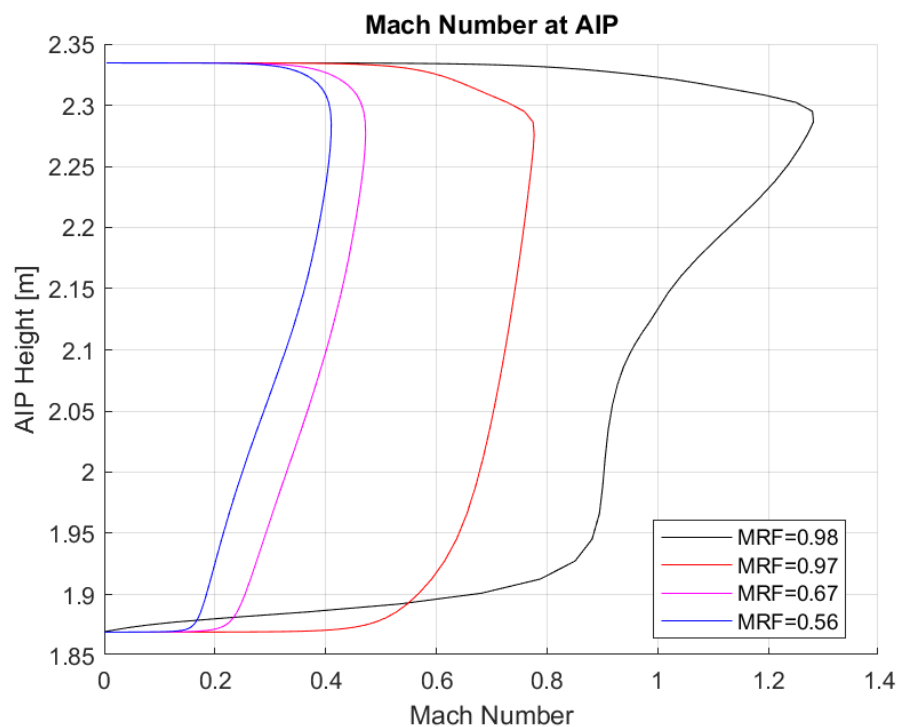


FIGURE 5.16: Comparison of Mach Number at the AIP (Design B)

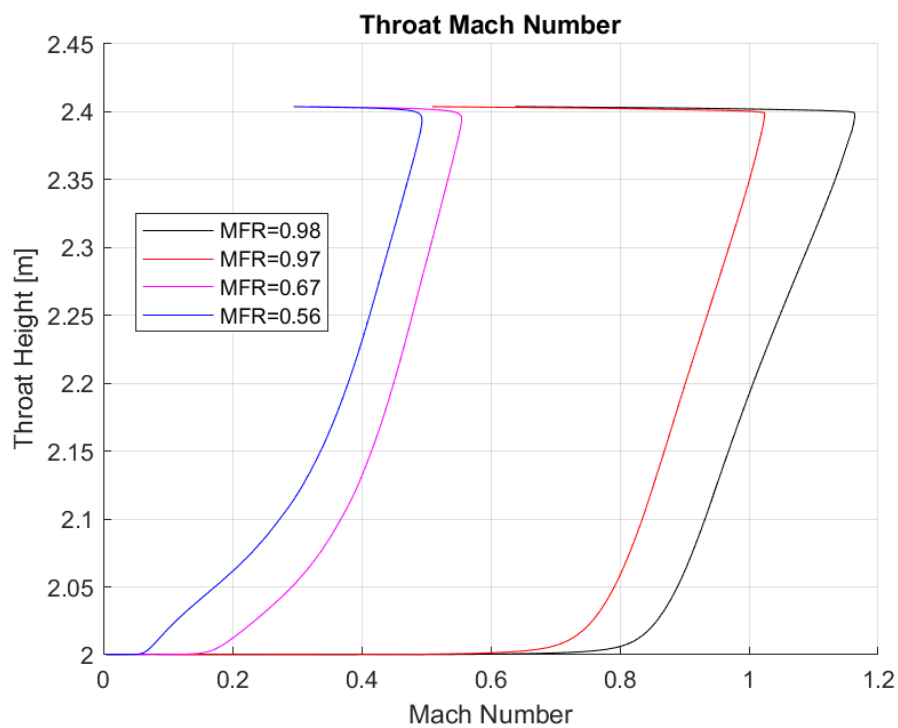


FIGURE 5.17: Mach Numbers at the throat of the duct (Design B)

As mentioned in the previous part, at high $MFR \sim 1$ the total thickness of the boundary layer is ingested (100%) and, in addition, 35% of the free stream. Generally, the amount of flow ingested by this intake is more than what obtained from the Design A. This because the thinner shape of the lip allows ingesting more flow respect to the availability of the rounded lip.

On the other hand, $MFR \ll 1$ characterizes spillage air, and the δ_{BL} reaches heights bigger than the stream tube resulting in partial ingestion of the boundary layer $\sim (90\%)$. The following Figure 5.18 illustrates the percentage of boundary layer ingested respect to the variation of mass flow ratio.

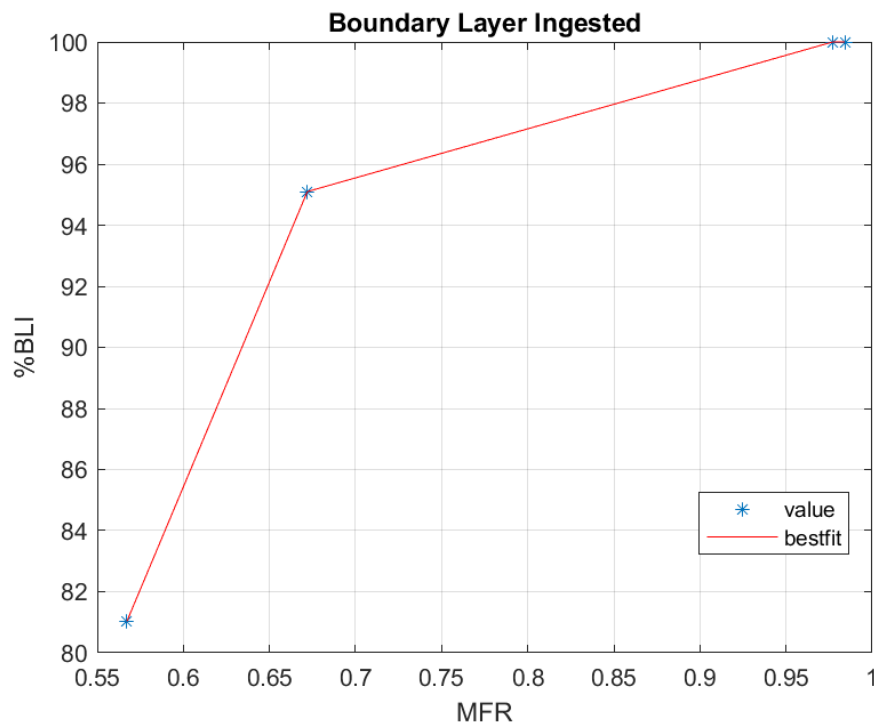


FIGURE 5.18: Percentage of boundary layer ingested respect to the variation of MFR (Design B)

Generally, results show that forcing the amount of mass flow rate through the duct increases the velocity even up to supersonic conditions as reported for both the 1st simulations resulting from being the worst cases independently from the design choice of the lip. The similarity that resembles the outcomes is that the increase in MFRs increases the velocity at the throat as more suction is produced. The stream tube is more cylindrical, and less spillage occurs. A significant pre-diffusion is instead noticeable by diminishing the MFRs, allowing the flow to slow down upstream of the intake and preventing supersonic conditions inside the duct.

The presence of the nacelle with the rounded elliptical lip influences more the behaviour of the flow rather than with the sharp lip due to the difference in aspect ratio and CR, allowing the thinner profile to less disturb the approaching flow and better behaves for high MFRs. However, it presents a poor characteristic for the lip pressure loss as the mass flow ratio decreases below the unity. On the other hand for low-speed of the incoming flow, the elliptical lip prevents lip separation, for its robustness and bigger thickness.

Figures 5.19 and 5.20 show the behaviour of the flow approaching the different lip designs through the axial velocity vectors. As can be seen, for the low MFR=0.56, the elliptical lip allows the flow to be more attached and reduce the high instability of the flow that, instead, occurs accounting for the sharp lip, especially in the outer part of the lip.

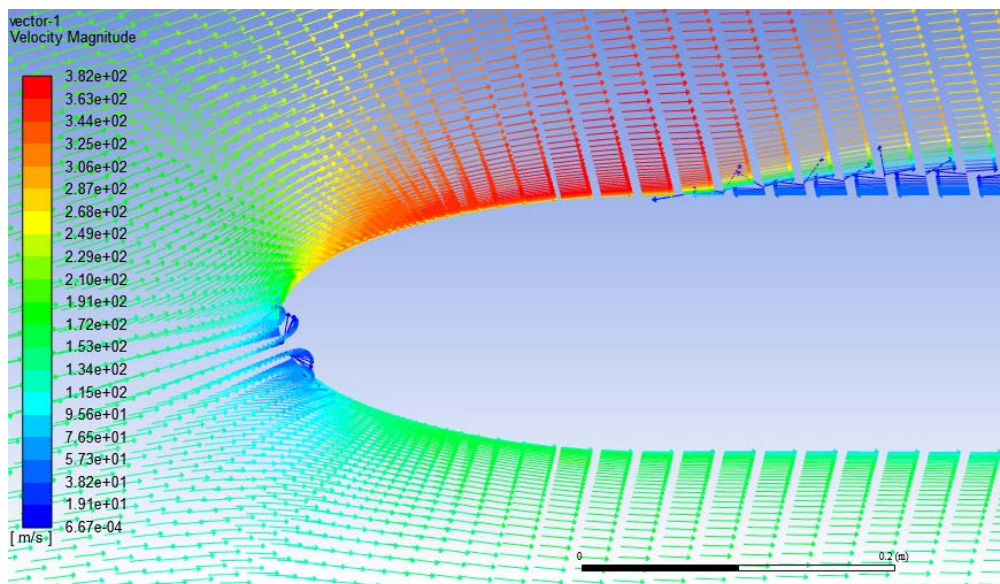


FIGURE 5.19: Lip separation Design A, MFR=0.56

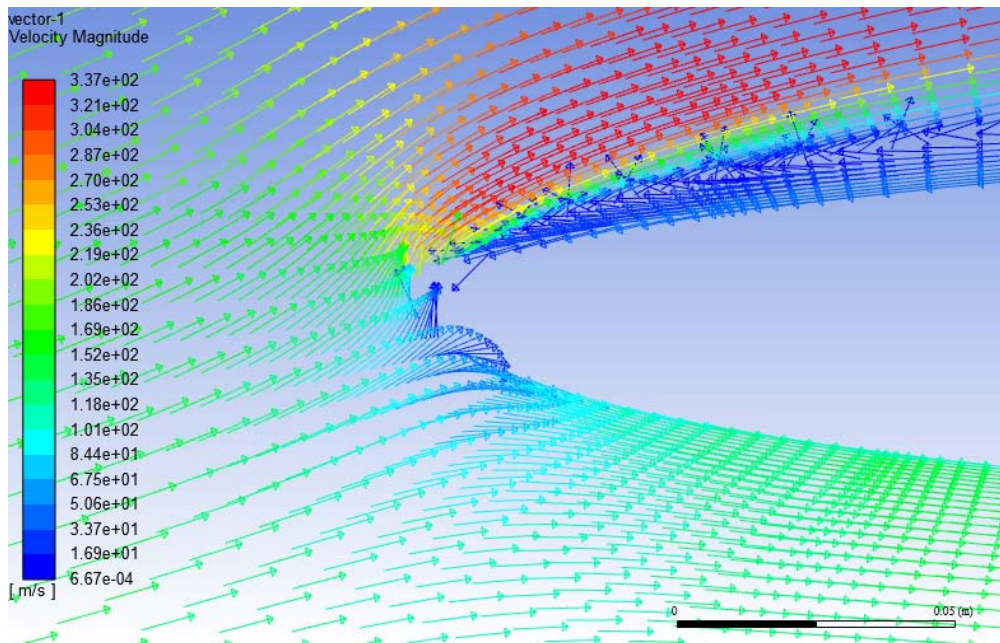


FIGURE 5.20: Lip separation Design B, MFR=0.56

5.3 Pressure Recovery Analysis

How the total pressure develops inside the duct is another essential property of the flow that can be highlighted because it is directly linked to the principal source of loss. A fluid that flows inside a duct is affected by pressure losses, namely a drop of the pressure due to the insurgence of turbulent mixing flow, flow separation and the skin friction present inside the duct. An increase, as well as a restriction of the duct, represents a source of pressure loss. In the case of this study, the duct is designed to avoid diffusion, so that the inlet and the outlet area are kept the same.

Higher MFRs mean an almost cylindrical stream tube and high axial velocities of the flow entering the intake. This leads to a weak pre-diffusion and low losses upstream of the intake, but high velocities inside the duct.

For example, the pressure drop can be seen at the first bend of the S-duct and in the lower elbow at the AIP. This because the rapid flow hasn't enough time to gradually slow down and follow the S-shaped geometry. Besides, because of the skin friction the flow loses its uniformity and non-axial flow velocities occurs, leading to flow separation (also visible in Figure 5.8). The initial pressure and mach outlet condition represents a limit to the distribution of the pressure of the moving flow inside the duct, leading to the generation of losses. The high pressure loss involved in these locations can be visualized in the following Figure 5.21 related to the ellipse lip design.

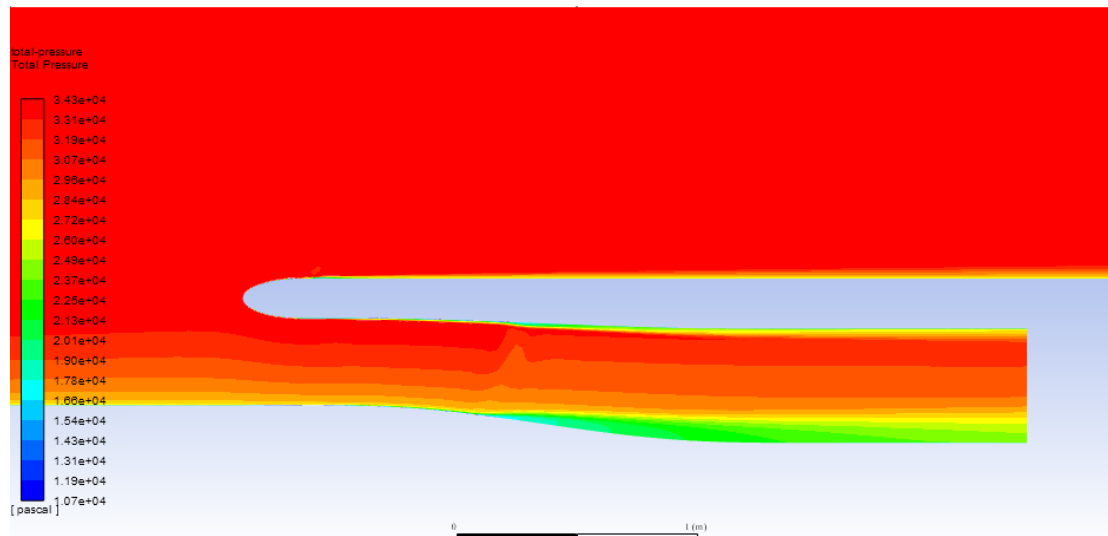


FIGURE 5.21: Total Pressure loss (Design A, AR=3, CR=1.25 M=0.78, $H_{throat}=0.3590$ m, MFR=0.85)

Differently, the divergent stream tube in front of the intake produced by decreasing the mass flow ratio allowed the flow to decelerate enough even inside the duct and thus allowing a uniform diffusion, which is stronger even upstream of the intake. No critical pressure drop occurs inside the duct because no separated flow arises. However, low velocities of the flow mean loss of energy and thus, the overall total pressure is reduced. A visible spillage drag also interests the external part of the lip. An example is given through Figure 5.22, in which, for a low MFR, the distribution of the total pressure results low but more uniform respect to the previous case studied.

Lastly, Figures 5.23 and 5.24 display the behaviour of the total pressure at the AIP related to Design A and Design B, highlighting the fact that the pressure dropping causes more losses for the highest MFR close to the wall.

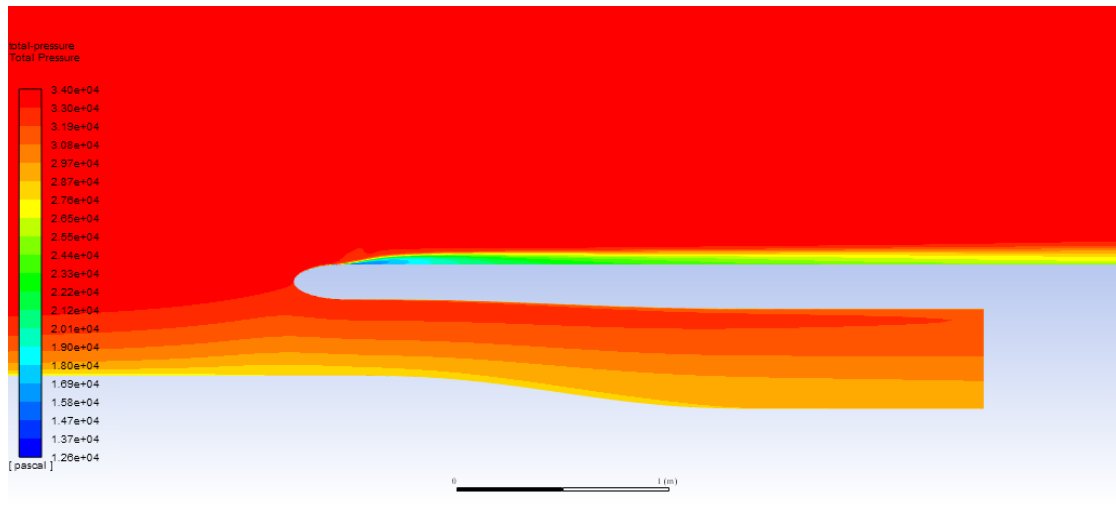


FIGURE 5.22: Total Pressure loss (Design A, AR=3, CR=1.25 M=0.78, $H_{throat}=0.3590$ m, MFR=0.56)

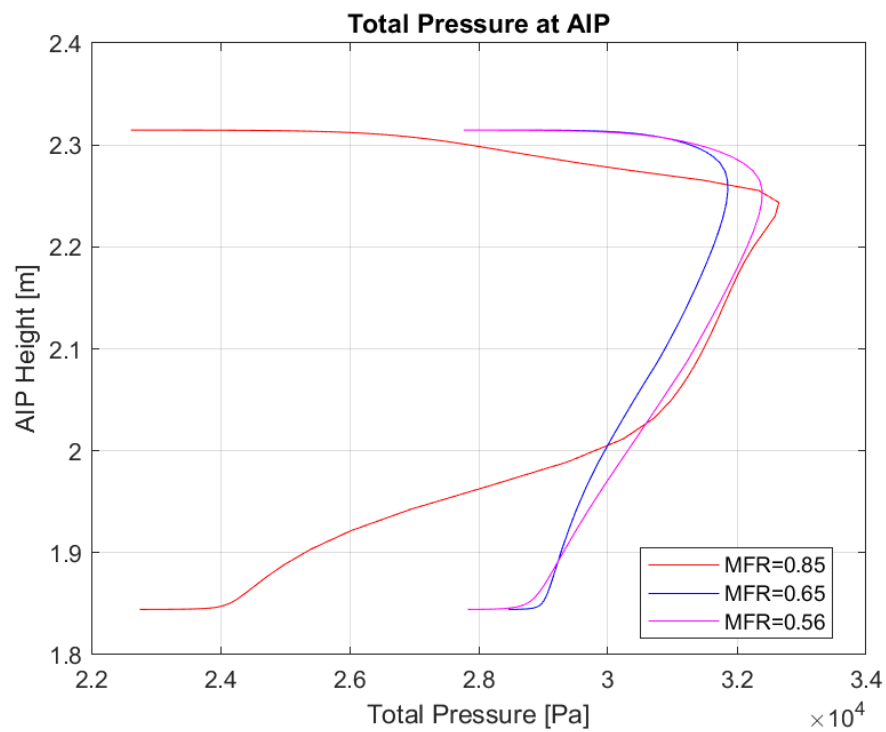


FIGURE 5.23: Total Pressure distribution at the AIP (Design A)

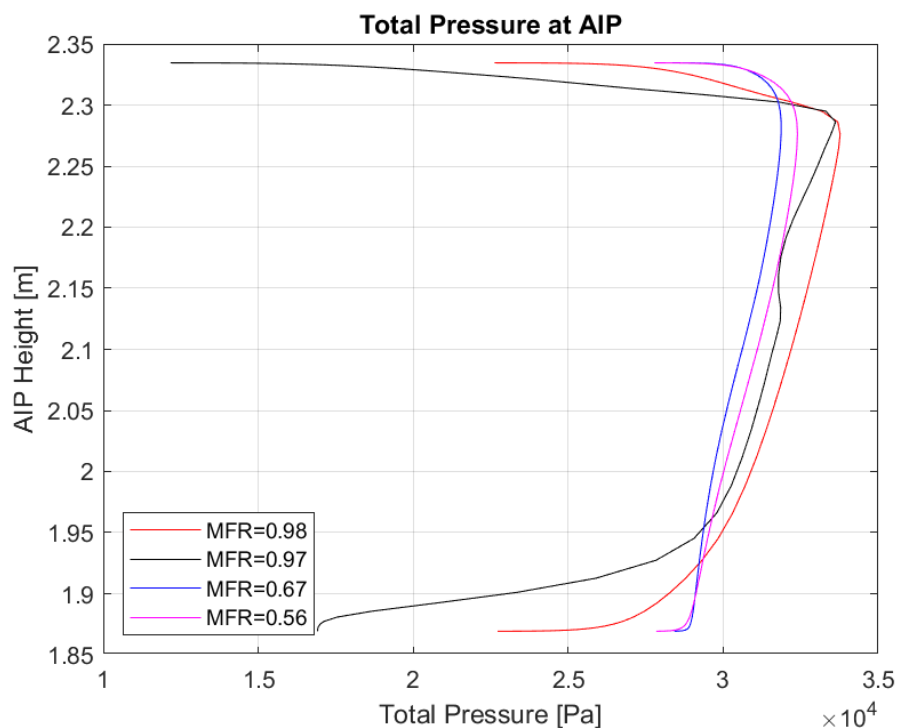


FIGURE 5.24: Total Pressure distribution at the AIP (Design B)

An assessment can also be done regarding the pressure coefficient calculated along the fuselage for each simulation.

Figures 5.25 and 5.26 give a representation of this important parameter that shows how the pressure develops from the nose of the fuselage to the inlet of the intake, accounting for both Design A and B.

As expected, an increment of static pressure can be observed in the proximity of the nacelle where the velocity begins to decelerate, then a decrease of pressure is visible where the flow starts to accelerate again in the proximity of the throat of the duct until the last increase inside the duct, where the flow turns to slow down again.

This trend is strongly evident for the baseline and for the 1st simulation, where the MFRs accounted for are the highest. In these cases, the static pressure drops considerably, and the pre-diffusion appears significantly weaker respect to the other cases.

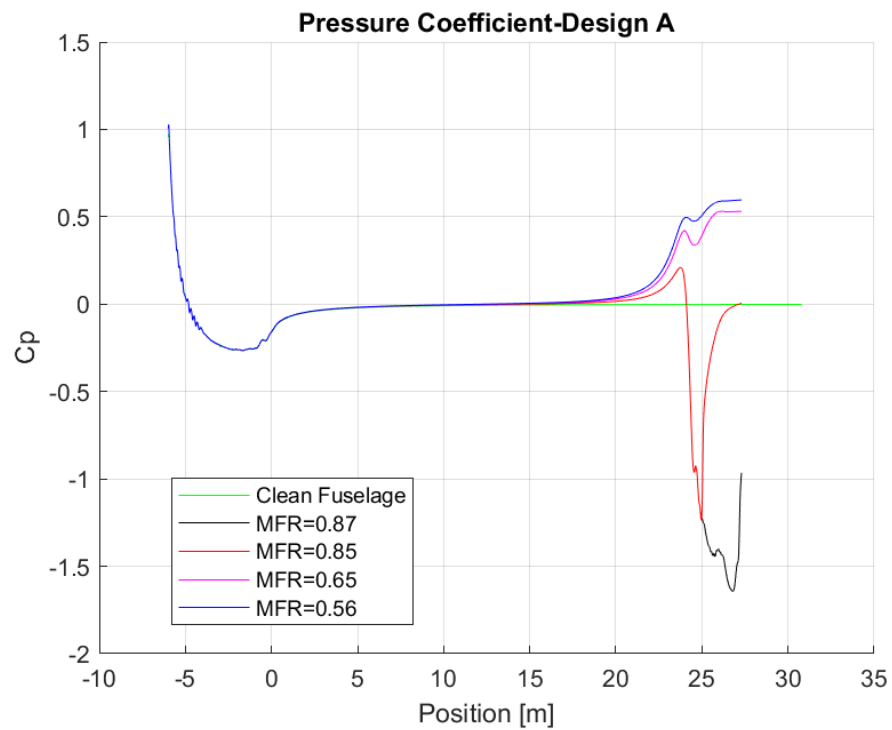


FIGURE 5.25: Pressure coefficient distribution along the fuselage (Design A)

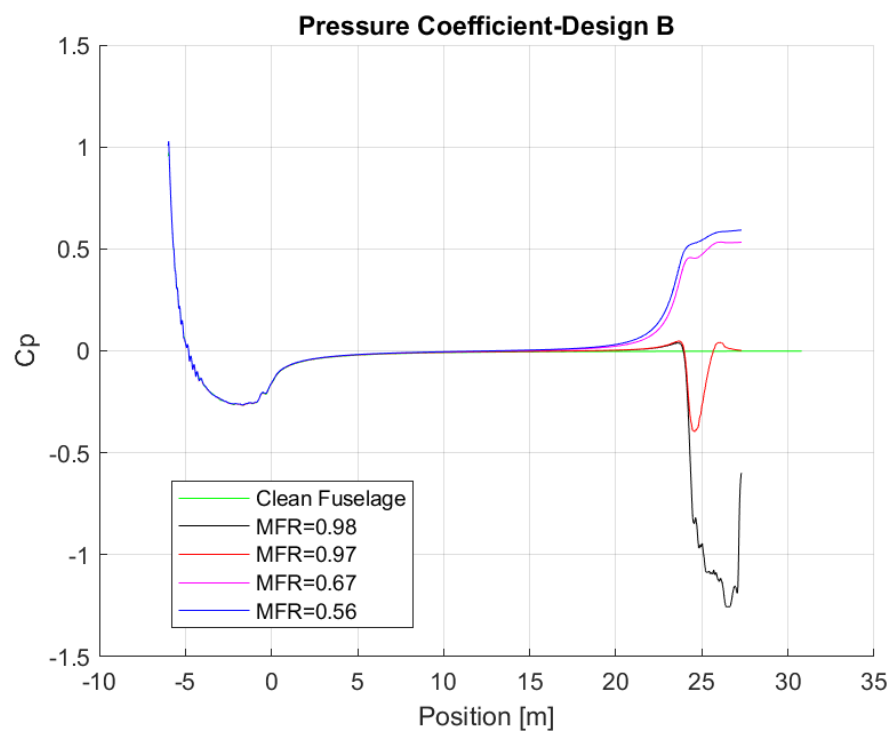


FIGURE 5.26: Pressure coefficient distribution along the fuselage (Design B)

5.3.1 Pressure Recovery and MFR

The pressure recovery was calculated for all the designs, and the results were compared for different MFRs. It has been assessed relative to four crucial sections of the intake that are the position of the point of divergence(0), the highlight(1), the throat(2) and the outlet of the duct(3). All the pressure ratios have been calculated through the evaluation of the mass-weighted averaged approach, present in the solver Fluent, for the calculation of the total pressure in each section.

This allowed comparing the results properly accounting for the different mass flow rate passing through each cross-sectional area. The two following figures display the values of pressure recovery assessed on different points. The ratio from the AIP to the point of divergence is represented by pink points; the red ones deal with the pressure recovery inside the duct from the AIP to the throat; the black and the blue points represent the evaluation of the pressure recovery in the pre-diffusion region upstream of the intake from the throat to the point of divergence and from the highlight to the point of divergence, respectively.

Figure 5.27 shows that the best results for all the MFRs accounted are given before the flow enters the intake (blue stars), and this can be related to the fact that in the pre-diffusion zone, even though the flow is slowing down losing its energy, the wetted area characterized by skin friction is very little and consequently the losses.

It can be seen that the higher MFR assumed, the higher pressure recovery is noticeable because the stream tube tends to be cylindrical, the spillage of air reduces and the pressure loss due to the diffusion of the flow is limited. The best results can be noticed for MFR=0.85 with PR=0.996% in respect with PR=0.992% for the lowest MFR.

Almost the same positive trend is visible by accounting for the throat in the calculation of the pressure ratio. However, the pressure recovery is lower, since losses occur because of the increment of the skin friction and the restriction of the duct.

Things change inside the duct (red points), especially relative to high MFRs. The pressure recovery passes from the value of 0.991 for the lowest mass flow ratio, through 0.95 for MFR=0.85, up to 0.945 for the highest MFR. The presence of separated flow, due to the rapid diffusion after the supersonic conditions achieved, increases considerably the pressure loss close to the wall of the first bend and in the proximity of the AIP.

The overall evaluation (pink points) highlights the whole distribution pointing out the bad behaviour relative to the high mass flow ratios inside the duct ($\sim 0.93-0.94$) compared to the low MFRs (~ 0.98).

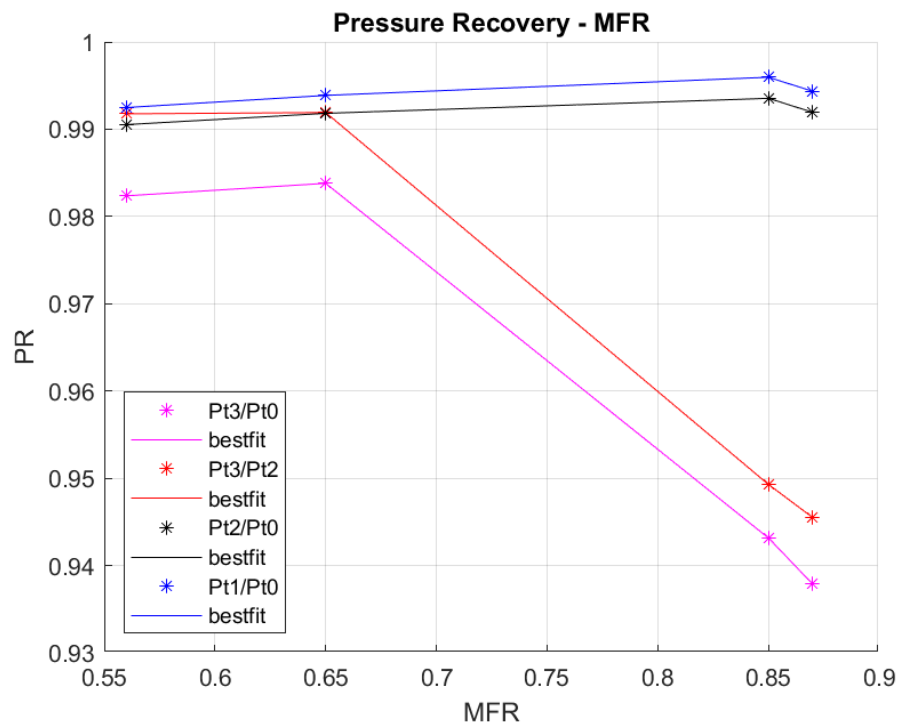


FIGURE 5.27: Pressure recovery (Design A): from the AIP to the divergence point (PINK POINTS); from the outlet to the throat (RED POINTS); from the throat to the divergence point (BLACK POINTS); from the highlight to the divergence point (BLUE POINTS)

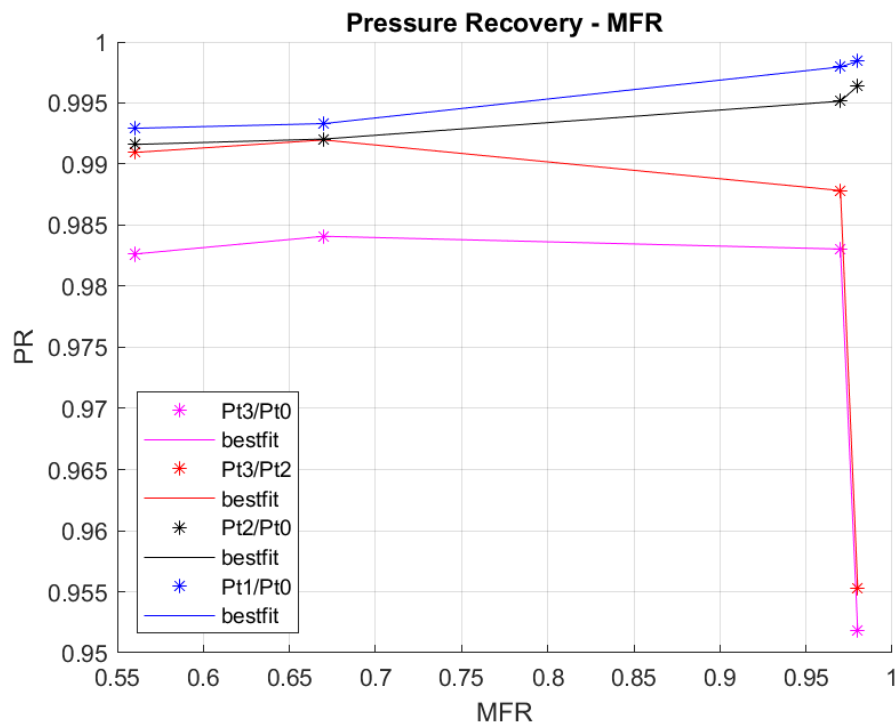


FIGURE 5.28: Pressure recovery (Design B): from the outlet to the divergence point (PINK POINTS); from the outlet to the throat (RED POINTS); from the throat to the divergence point (BLACK POINTS); from the highlight to the divergence point (BLUE POINTS)

Almost the same analysis can be done relative to the Design B (Figure 5.28): the pressure recovery inside the duct gets worse as the MFR increases ($PR \sim 0.96$). These losses have an impact also on the overall trend that compared to the ones of the pre-diffusion region returns lower values.

Similarly to Design A, the low MFRs provide a $PR \sim 0.98$, while the highest $MFR = 0.98$, derived from forcing the mass flow rate, returns very low $PR \sim 0.95$. The results for the thinner lip are better particularly upstream of the intake since the MFRs are higher than Design A, the thickness of the lip is smaller, and the throat height is higher: optimal condition of the stream tube, less deviation of the streamlines of the flow entering the intake and larger area that leads to a higher amount of mass flow ingested.

Besides, the convergent duct generated by the thickness of the lip at the throat, that disturbs the uniformity of the flow, is less pronounced. The total pressure recovery for the bigger $H_{throat}=0.4038$ is ~ 0.983 and for the smaller $H_{throat}=0.3590$ is ~ 0.943 , both accounted for the initial MFRs derived from each configuration.

Finally, a general trend of pressure recovery can be observed. The increase in MFR causes pressure recovery to drop inside the duct. However, at the same time, the increase in MFR ensures better pressure recovery upstream of the intake. Between the two designs, the effect of lip shapes on the pre-diffusion pressure recovery is not huge as only a difference of $\sim 0.4\%$ can be observed, in particular relative to the lower MFRs. A general difference of 4% can be, instead, observed between Design A and B at the initial MFR.

A preferable AIP Mach number ($M\sim 0.7$) was achieved when $MFR=0.85$ for Design A, and for $MFR=0.97$ for Design B, however, in both cases, the behaviour of the flow is characterized by very high velocities inside the duct, which can make the intake poorly performing.

An overall pressure recovery at the AIP of each conducted intake designs for all the MFRs is presented in Figure 5.29.

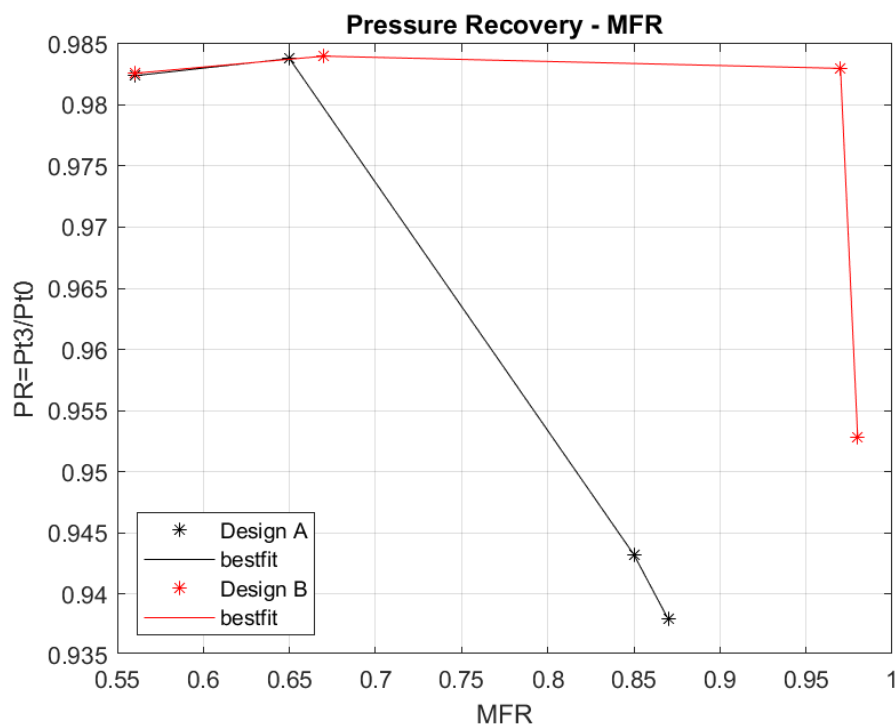


FIGURE 5.29: Comparison of overall pressure recovery for different MFRs

In conclusion, to design an optimized intake for BLI from the conducted study, a thinner lip configuration with an aspect ratio of 6 and a choice of a reasonable CR would be beneficial for the intake performance in terms of the upstream pressure recovery and for high-speed flow. However, once the mass flow ratio drops to values below the unity, the sharpness of the lip profile induces lip pressure loss and even reversed flow in the external cowl. Differently, the elliptic lip allows more attached flow thanks to its robustness and bigger thickness resulting in a better lip performance relative to low-speed.

In an overall perspective, the difference in pressure recovery between the two designs is small since the design choices of the throat height and CR have heavily affected the position of the captured flow for each simulation, but not the overall behaviour of the ingesting flow.

Indeed, despite the presence of the nacelle disturbing the approaching flow, no substantial differences in the diffusion before the inlet have been highlighted since the intake has been placed at the same height for both the designs and a little difference in the throat heights have been considered.

The part of the geometry that would have influenced the most the intake performance is the S-duct.

However, in this study, it has been designed in order to prevent from diffusion and to ensure as far as possible a uniform flow at the AIP. ($M < 0.78$)

These design assumptions and the time restrictions may have limited the collection of data and thus the accuracy of the results. Some geometrical modifications and some precautions would have helped with the analysis of other aspects and improved the assessment of the intake performance. Many improvements can be taken into account regarding several aspects of the project, and some of them are suggested in Chapter 8 of further works.

This section completes the main analysis of this thesis. The next chapter introduces a preliminary analysis conducted on the power saving coefficient and the analytical approach adopted to quantify the efficiency of a BLI-configuration in terms of the power required to the engine.

Chapter 6

Power Saving Coefficient

To assess the efficiency of the boundary layer ingestion, a power-saving coefficient (PSC) defined with Equation in 2.3.3 is used. As explained in section 2.3.3, the PSC parameter is used to evaluate the impact that a BLI configuration has on the performance of the system as a whole. It describes the difference in necessary propulsive power for a propulsor without boundary layer ingestion compared to one with ingestion that provides the same amount of thrust.

The BLI systems are inherently integrated and exposed to the same investing airflow at the same cruise flight condition of all the other structural components (podded engines, wings, tail, fuselage) of the aircraft. In this perspective, the assessment of such a performance parameter must include aspects of the aircraft configuration relying on knowledge of a control volume that encompasses the whole aircraft in order to sufficiently represent the real performance in terms of installed thrust, aircraft drag and overall losses.

Especially in integrated architectures such as the BLI, because of the intrinsic interaction between the propulsion system and the airframe (Reference in Section 2.3.1), it becomes more difficult to define the net thrust produced by a propulsion system.

CFD methods are useful for the analysis of the combined aircraft and propulsion system accounting for all the components involved in the generation of drag: the portion of the airframe profile drag that enters the propulsion system inlet, that is accounted for in the propulsion system (internal flow), as well as all the other sources of loss that interest the aircraft as a whole.

In this study, the CFD analysis dealt only with the intake performance of a BLI engine, providing with the initial conditions at the AIP of a hypothetical combined fan. Because of time restriction, however, no CFD analysis has been conducted for the isolated fan chosen for the PSC study.

Therefore, the power saving coefficient has not been assessed through taking into account all the critical considerations previously explained, and thus, limiting the investigation to a bound control volume. Several assumptions that have been made relative to the approach adopted required to be highlighted:

- Calculation of the ram drag for the BLI engine considering an internal force control volume: the inlet velocity concerns only the stream tube ingested by the intake (internal flow), not the free stream velocity that invests the whole aircraft.
- Development of an analytical study for modelling the isolated fan ideally located in the same position of the BLI engine: the domain encompasses only the internal flow neglecting the external drag and limiting the calculation of thrust to an uninstalled thrust.
- Hypothesis of a given range of uninstalled thrust.
- Comparison of the two configurations in terms of the same amount of thrust.

At this preliminary and approximated design stage, the methodology adopted began with the further distinction which concerns the inlet velocities involved: a mass-weighted average axial velocity extracted from the flow investing the intake (Desing B, MFR=0.97) at the point of divergence for the BLI configuration; the free stream velocity at cruise condition for the isolated fan.

As can be seen in Figure 6.1, the necessary propulsive power is reduced by decreasing inlet velocities, and since the propulsive power is representative of the fuel consumption, a reduction means lower fuel burn and, therefore, a more efficient engine. The next section will present the procedure involved in the assessment of the propulsive power for both the engines and, thus, the calculation of the PSC.

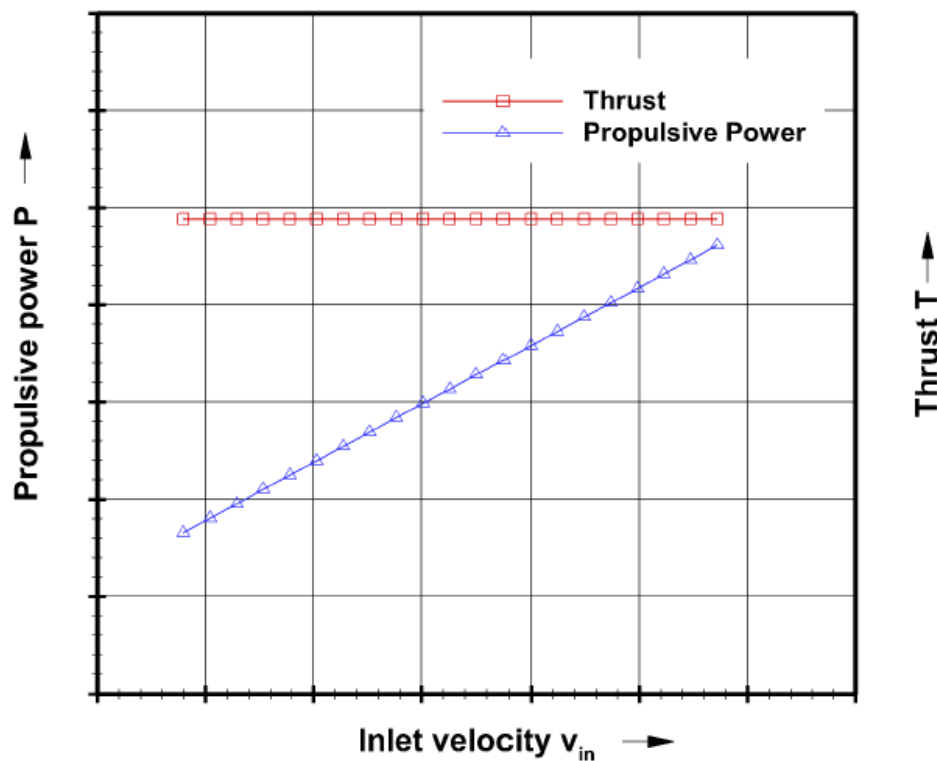


FIGURE 6.1: Necessary power for a constant thrust at varying inlet velocities [51]

6.1 Method of Analysis

The implementation of the method of analysis has been realized with Matlab code giving in input some initial parameters assumed to be reasonable based on previous works.

To model the BLI fan, the inlet condition has been derived from the CFD simulation accounting for the mass-weighted average total temperature and pressure at the AIP (cross-sectional area 3 in Figure 5.11). For simplicity, the inlet of the fan will correspond to a new section 1 and the outlet of the fan to a new section 2. For a MFR=0.97 the mass flow rate at the AIP has been also extracted.

On the other hand, the total far-field temperature has been considered as the temperature of the flow that invests the isolated fan ideally located in the same position of the BLI engine. No change in total temperature has been considered from the intake to the fan because the intake has been supposed to be adiabatic. Different was the approach with the total far-field pressure that has been multiplied by a loss intake coefficient resulting in lower total pressure at the inlet of the fan. To calculate the mass flow rate passing through this fan, the far-field density and velocity have been considered, and a frontal area equal to the $A_{highlight}$ of the intake for BLI has been assumed.

The following Table 6.1 illustrates the main inlet conditions for the BLI and the isolated fan.

Inlet Parameters	BLI Fan	non-BLI Fan
T_{01}	243.17 K	243.19 K
P_{01}	31752.89 Pa	$0.98 * 33927.18 = 33248.63$ Pa
\dot{m}	456.0927 kg/s	505.7478 kg/s
ν_0	213.0095 m/s	230.21 m/s

TABLE 6.1: Inlet conditions for BLI engine and isolated fan

In order to define and calculate the propulsive power, the specific work done by the fan needs to be calculated. Thus the calculation of the fan pressure ratio (FPR) was essential.

The chosen approach, to compute the downstream conditions of the fan, dealt with an inverse analysis of the thermodynamic cycle of the engine.

Therefore, starting from the nozzle, supposed to be ideally expanded in this study, the exhaust flow velocity v_j has been obtained by giving in input a range of uninstalled values of thrust.

The range of thrust considered was from 20000 to 100000 kN and the equation used to calculate the exit velocity came from the simple definition of uninstalled thrust for an adapted nozzle:

$$v_j = \frac{T}{\dot{m}} + v_0 \quad (6.1)$$

where the v_0 is the inlet velocity involved. Recalling the premise done, v_0 is different for the two propulsion systems accounted due to the choice of an internal control volume. The referring values can be found in the Table 6.2.

Then, considering an isentropic nozzle efficiency of $\eta_{nozzle}=0.98$, the FPR has been calculated iteratively from this equation:

$$v_j = \sqrt{2 * \eta_{nozzle} * \frac{k * R}{k - 1} * (T_{01} * FPR) * [1 - (\frac{P_0}{P_{01} * FPR})^{\frac{k-1}{k}}]} \quad (6.2)$$

where $k=1.4$ for air and $R=287$ J/kgK as the constant of gas. Once derived the FPR, the condition at the outlet of the fan can be obtained for each configurations as function of:

$$T_{02} = f(T_{01}, FPR) \quad (6.3)$$

$$P_{02} = f(P_{01}, FPR) \quad (6.4)$$

The procedure ends with the computation of the propulsive power following the equation:

$$P = \dot{m} * C_p * \Delta T \quad (6.5)$$

where $C_p=1004.5$ J/kgK and $\Delta T=T_{02}-T_{01}$. With different inlet conditions, the two configurations resulted in different FPR and thus different propulsive powers required to the engine for the same amount of thrust.

Recalling the equation (2.27), the PSC has been calculated and displayed in Figure 6.2. Moreover, a comparison between the propulsive powers generated can be visualized in Figure 6.3.

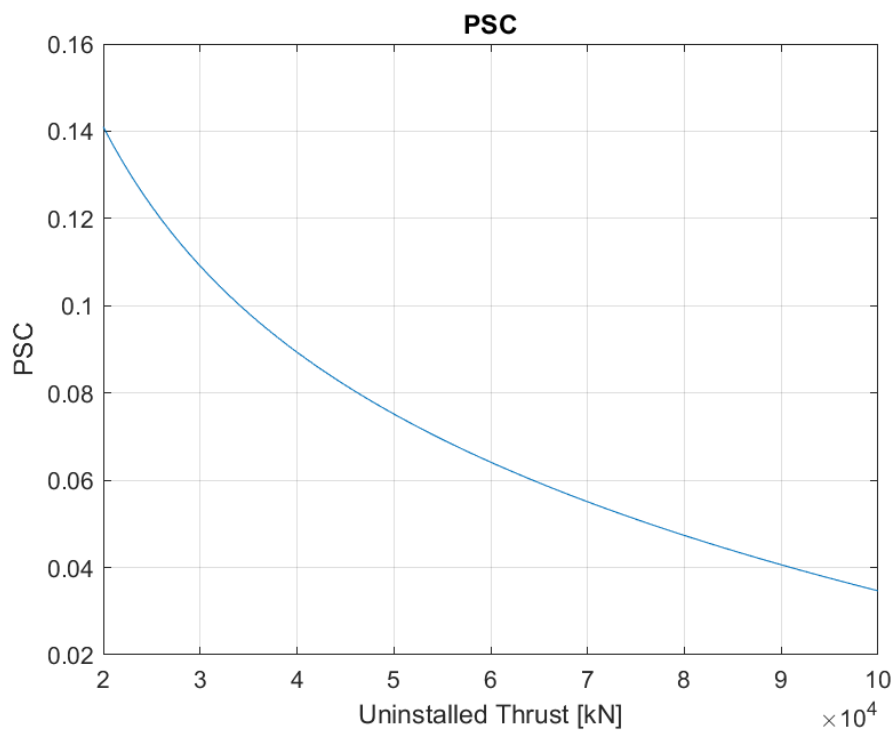


FIGURE 6.2: PSC results

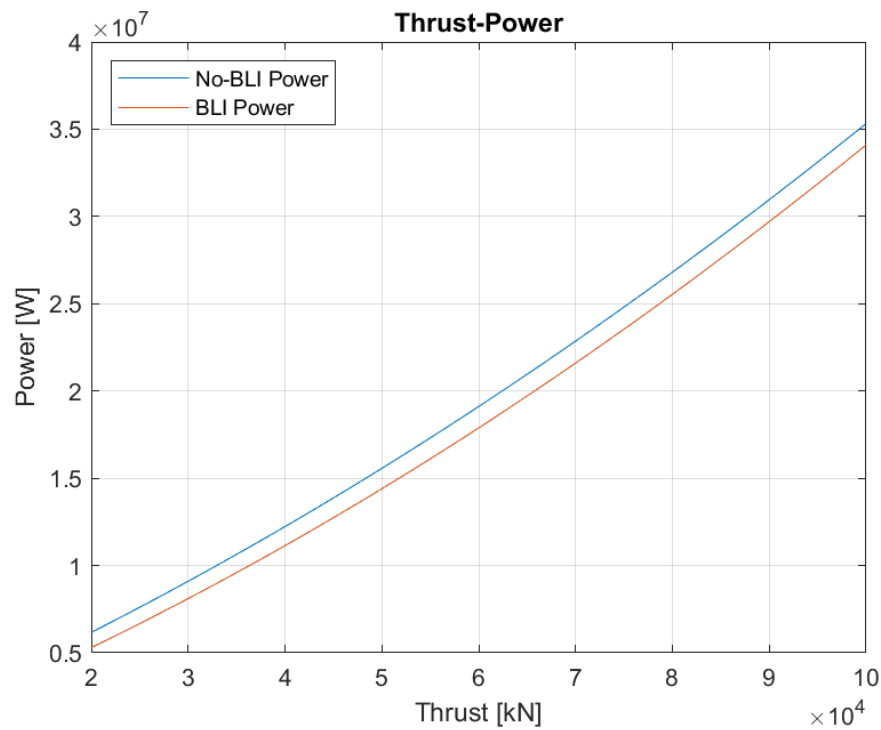


FIGURE 6.3: Comparison of propulsive power for BLI and no-BLI engine

Results showed something predictable from the several assumptions made: the propulsive power required to the engine for a BLI configuration is smaller than that for a non-BLI configuration because the ram drag used is limited to the value of the slow down flow ingested by the intake. This proves the fact that a BLI engine is more efficient than an isolated fan because it ingests a lower flow velocity. The range of the calculated PSC resulted in being reasonable between 2% and 14%; however, these results can be discussed due to the approximations made.

This chapter completes the investigation of this thesis. The next chapter will highlight the important conclusions and summarize the main results obtained.

Chapter 7

Conclusion

This final chapter aims to provide a summary and to highlight the relevant findings from the conducted investigation.

This project investigated the performance of an intake for a boundary layer ingestion body through a parametric study conducted with the *Computational Fluid Dynamics* analysis.

The primary model studied in this thesis was generated using Matlab code based on an entirely new geometry that consisted of a fuselage, without wing and tail for simplicity and an integrated engine composed by an S-duct intake.

For the first part of the analysis, the boundary layer profile developed on a baseline geometry was explored. It consisted of a two-dimensional clean fuselage without the BLI engine to learn about the behaviour of the airflow and the development of the boundary layer over a conventional aircraft. The simulation was conducted at the flight condition (11000 m and $M=0.78$). The results showed that the boundary layer has fully developed and, at the distance of 24 m, its thickness has been calculated as 99% of the free stream velocity. With this information, the geometry of the intake for BLI was set out. In this position, the all-around tubular fuselage installation allowed to ingest the thickest boundary layer possible. Two-dimensional intakes were designed for BLI analysis. The designs were created to carry out a study that helped to analyze the parameters that affected the performance.

Altogether two intakes were designed to investigate the effect of the lip shape (sharp and ellipse), the effect of CR, the effect of throat height on intake performance at different mass flow ratios, while the structure of the S-shaped duct was built up to ensure a uniform flow at the AIP.

Using CFD tools, the mesh was then generated through ICEM. A multi-block grid was used for all the cases investigated. A high grid quality was achieved and converted to an unstructured mesh. Verification and validation were performed on a series of mesh densities to obtain the most optimum mesh.

In the end, medium mesh with almost 115 thousand elements was chosen and then opened with Ansys Fluent. A pressure-based solver with a $k-\omega$ SST turbulence model was used as it was the most suitable for the study. Most of the results presented have fully converged indicated by the residuals in the order of 10^{-6} .

The amount of boundary layer ingested depended on the mass flow ratio assumed and evaluated respect to the AIP and a suitable interface point ahead of the intake, where the difference in static pressure respect to the clean fuselage was relevant due to the presence of the nacelle. The results were quite similar for both the designs showing that for low MFRs the captured flow by the intake was smaller than the actual thickness of the boundary layer assessed at the interface point ingesting between 80% and 90%. On the other hand, higher MFRs led to a smaller divergent stream tube upstream and less spillage, allowing the intake to ingest the total thickness of the boundary layer (100%). However, for low MFR=0.67, the nacelle with the thinner lip allowed to ingest up to 96% of the boundary layer without making the flow reaching supersonic conditions, allowing, instead, to decelerate enough before the AIP. ($M \sim 0.5$)

It was clear that the simulations for MFR of 0.85 for the elliptic lip and of 0.97 for the sharp lip showed the best Mach number at the AIP ($M \sim 0.7$), but it must be considered that, inside the duct, the flow choked as the flow accelerated to a Mach number $\simeq 1.0$, resulting in a heavily unstable flow approaching the AIP. For both designs with the lowest MFR of 0.56 the flow fully decelerated up to $M \sim 0.4$ at AIP, allowing the flow to keep its uniformity, but producing more spillage upstream of the intake.

Intake performance was assessed with the total pressure recovery. For all the intake designs, the pressure recovery was analyzed among different sections as the ratio of the mass-weighted averaged total pressures.

A comparison between different lip designs showed that the sharp shape achieved the best pressure recovery of 0.983, accounting for the whole stream tube and the initial MFR. A considerably lower value of 0.943 was found by increasing the CR up to 1.25, (Design A). The throat height had a substantial effect on pressure recovery. Increasing the throat height increased the pressure recovery by 4%. Therefore, the results for the thinner lip showed a better pressure recovery, in particular, upstream of the intake since the MFRs were higher than Design A, the thickness of the lip was smaller, and the throat height was higher. All these characteristics led to an optimal condition of the stream tube, a less deviation of the streamlines of the flow entering the intake and a larger area that consequently led to a higher amount of mass flow ingested. However, from the analysis of lip performance, the elliptical lip provided better conditions to the incoming flow for low MFR by preventing lip separation.

Generally, a global trend of pressure recovery could be observed. The increase in MFR caused pressure recovery to drop inside the duct especially in-wall because of a higher impact of the skin friction on the high velocities involved. However, at the same time, the increase in MFR ensured better pressure recovery upstream of the intake due to the weak pre-diffusion, which prevented the flow from losing too much energy. A comparison between the pressure coefficients over the fuselage helped to visualize this trend in terms of static pressure, velocities and energy involved.

Results from the power saving coefficient showed something predictable from the several assumptions and approximations made during the analysis. The propulsive power required to the engine for a BLI configuration was smaller than that for a non-BLI configuration because of the choice of the ram drag. This proves the fact that a BLI engine is more efficient than an isolated fan, resulting in a range of the calculated PSC between 2% and 14%.

This analysis is a preliminary assessment for an intake performance study. The results can be discussed because some assumptions have been made during the project by highlighting some limitations on the accuracy of the results. The boundary layer profile has been extracted from a two-dimensional simulation and extrapolated neglecting the complex flow field of a 3D domain that heavily affects the intake performance. Furthermore, a comparison between just two designs has been investigated because of the time available to do the project and the complexity of the geometry. For a more in-depth analysis, other flight regimes should have also been investigated.

Some more careful design choices would improve the analysis of more aspects and the assessment of the intake performance. The next chapter gives an idea of some recommended further work.

Chapter 8

Further Works

As future work, there are some parts of the design process that should be revisited, starting from considering the limitation involved in a two-dimensional study. The intricate 3D flow field strongly affects the intake performance in a way that a 2D investigation could not capture. For a more rigorous study, a complete 3D analysis could be executed. This would help to assess the real effects.

However, a two-dimensional study still provides a good approximation of BLI problems; therefore, it could be adopted accounting for more cruise flight conditions.

Further work on the parametric study could be related to the realization of more designs of the lip and more MFRs also varying the inlet location height. The effect of the S-duct curvature length and of the curvature degree could also be taken into account along with the effect of an angle of attack to study the lip separation. The future projects should generate a higher mesh density with a near-wall model to get a better accuracy of the results.

The extrapolation of the boundary layer could be improved by using a 3D model, the Power Law and considering the effect of the shape factor on the flow separation.

Using other performance parameters such as the distortion coefficient and the power saving coefficient could help to evaluate the severity of distortion and estimate the benefits of a boundary layer ingesting body, respectively.

Modification and optimization of nacelle parameters could be performed to evaluate the sensitivity to flow distortion and the magnitude of losses.

Rather than modelling a BLI with an internal control volume, an external control volume could be used in order to make valid considerations on the thrust-drag accounting and on the efficiency of the BLI system as a whole. The evaluation of the PSC could be furthermore improved by conducting a CFD analysis on an isolated fan located in the same position of the BLI.

In this way, a more realistic investigation could be conducted to compare the benefits derived from a podded and a BLI engine.

Bibliography

- [1] Farokhi. *Aircraft Propulsion*. John Wiley & Sons, second edition, kindle edition edition, 2014.
- [2] E. Moss C. Law and N. Tully. *Boundary Layer Flows*. in Fluid Mechanics I, Johannesburg: University of the Witwatersrand.
- [3] Jr. University of Maryland John D. Anderson. *Fundamentals of Aerodynamics*. McGraw-Hill Companies, Inc., fifth edition edition, 2011.
- [4] H. Schlichting. *Boundary Layer theory*. McGraw-Hill Book Company, seventh edition edition, 1979.
- [5] D.H Mudimeli. *Boundary Layer Separation from a Circular Cylinder*. School of Mechanical Industrial & Aeronautical Engineering.
- [6] Frank M. White. *Fluid Mechanics*. McGraw-Hill Companies, Inc, seventh edition edition, 2011.
- [7] Bio-mimicry. *Bio-mimetic Drag Reduction - Part 2: Aerodynamics and Hydrodynamics*. Aerodynamics, Aerospace Engineering Blog, available at: <http://aerospaceengineeringblog.com/bio-mimetic-drag-reduction-2/>, seventh edition edition, 2012.
- [8] D.Apsley. *Integral Analysis of the Boundary Layer*. Turbulent Boundary layers, 2009.
- [9] A. Plas. Performance of a boundary layer ingesting propulsion system. Master's thesis, Massachusetts Institute of Technology, Department of Aeronautics and Astronautics, 2006.

- [10] <https://www.nasa.gov/aero/reduce-fuel-burn-with-a-dose-of-bli>.
- [11] K. Geiselhart-R. Campbell M. Maughmer S. Schmitz B. Blumenthal, A. Elmiligui. *Computational Investigation of a Boundary Layer Ingesting Propulsion System for the Common Research Model*. 46th AIAA Fluid Dynamics Conference, AIAA Aviation, AIAA 2016-3812, 2016.
- [12] D. MacManus C. Goldberg, D. Nalianda, UK P. Pilidis, Cranfield University, and J. Felder. Installed performance assessment of a boundary layer ingesting distributed propulsion system at design point. *52nd AIAA/SAE/ASEE Joint Propulsion Conference, Propulsion and Energy Forum*, 2016.
- [13] Mark Drela. Power balance in aerodynamic flows. *AIAA journal*, 47, 2009.
- [14] Olivier Atinault Aurelien Arntz and Alain Merlen. Exergy-based formulation for aircraft aero-propulsive performance assessment: Theoretical development. *AIAA journal*, 53, 2014 .
- [15] 197 AGARD 237. *Guide to In-Flight Thrust Measurement of Turbojets and Fan Engines*. MIDAP Study Group, 1979.
- [16] Darrell Williams. *Application of boundary layer theory to BLI simulation*. 2015.
- [17] Andrew Rolt and John Whurr. *Andrew Rolt and John Whurr. Optimizing Propulsive Efficiency in Aircraft with Boundary Layer Ingesting Distributed Propulsion*. 22nd International Symposium on Air Breathing Engines, Phoenix, AZ, USA, 2015.
- [18] Leroy H. Smith. *Wake ingestion propulsion benefit*. *Journal of Propulsion and Power*. 9(1):7482, 1993. ISSN 0748-4658. doi: 10.2514/3.11487.
- [19] D. K. Hall. *Boundary Layer Ingestion Propulsion - Benefit, Challenges, and Opportunities*. in 5th UTIAS International Workshop on Aviation and Climate Change, Toronto, 2016.

- [20] O. C. Pendergraft D. M. Friedman L. Serrano R. L. Cambell, M. B. Carter. Design and testing of a blended wing body with boundary layer ingestion nacelle at high reynolds number. *AIAA 2005-0459*, 2005.
- [21] Sandesh Badgami. 2d cfd analyis of boundary layer ingesting intake. Master's thesis, Cranfield University, 2015.
- [22] A. M. O. Smith and H. E. Roberts. *The jet airplane utilizing boundary layer air for propulsion*. Vol. 14, No. 2, pp. 97–109 .
- [23] V. M. LUGO. Effects of boundary layer ingestion and thrust vectoring in distributed propulsion. Master's thesis, Cranfield University, 2010.
- [24] Joaquim R. R. A. *Coupled Aeropropulsive Design Optimization of a Boundary Layer Ingestion Propulsor*. Justin S. Gray Aerospace Engineer PSA Branch, NASA Glenn Research Center.
- [25] J. Welstead and J. L Felder. *Conceptual Design of a Single-Aisle Turboelectric Commercial Transport with Fuselage Boundary Layer Ingestion*. 2016.
- [26] M. K. Bradley and C. K. Droney. *Subsonic Ultra Green Aircraft Research: Phase II. N+4 Advanced Concept Development*. Nasa/Cr-2012-217556, (April 2011), p. 207, 2012.
- [27] M. K. Bradley and C. K. Droney. *Subsonic Ultra Green Aircraft Research: Phase II – Volume II – Hybrid Electric Design Exploration*. Nasa/Cr–2015-218704, II, p. 207, 2015.
- [28] K. B. Marty and K. D. Christopher. *Subsonic Ultra Green Aircraft Research: Phase I Final Report*. NASA/CR-2011-216847, Huntington Beach, California, 2011.
- [29] Bijewitz J. Kaiser S. Seitz, A. and G. Wortmann. Conceptual investigation of a propulsive fuselage aircraft layout. *86(6)*, pp. 464–472. doi: 10.1108/AEAT-06-2014-0079, 2014.

-
- [30] A. Seitz and C. Gologan. Parametric design studies for propulsive fuselage aircraft concepts. *CEAS Aeronautical Journal* 6(1), pp. 69–82. doi: 10.1007/s13272-014-0130-3, 2014.
- [31] Seitz A. Wieczorek K. Plötner K. O. Isikveren A. T. Steiner, H.-J. and M. Hornung. Multi-disciplinary design and feasibility study of distributed propulsion systems.
- [32] J. Bijewitz. The dispursal project: Investigation of propulsive fuselage and distributed propulsion aircraft concepts. 2015.
- [33] A. Bijewitz, J. Seitz and M. Hornung. Multi-disciplinary design investigation of propulsive fuselage aircraft concepts. 2016.
- [34] DisPURSAL. Distributed propulsion and ultra-high by-pass rotor study at aircraft level. 2013.
- [35] [https://wordlesstech.com/nasas-double bubble/](https://wordlesstech.com/nasas-double-bubble/).
- [36] Bonnefoy P. a. Blanco E. D. L. R. Dorbian C. S. Drela M. Hall D. K. Hansman R. J. Hileman J. I. Liebeck R. H. Lovegren J. Mody P. Pertuze J. a. Sato S. Spakovszky Z. S. Tan C. S. Hollman J. S. Greitzer, E. M. and K. D. N+3 aircraft concept designs and trade studies, final report volume 1.
- [37] Titchener N. Courtin C. Lieu M. Wirsing L. Tylko J. Jeffrey C. T. Roberts T. W. Yutko, B. M. and Church. Conceptual design of a d8 commercial aircraft. *17th AIAA Aviation Technology, Integration, and Operations Conference, (June)*, pp. 1–35, 2017.
- [38] C. Lannou. A-17 advanced technology low drag airliner aft fuselage propulsor design. Master’s thesis, Cranfield University, 2018.
- [39] Group Design Project Executive Summary. A-17 zephyr advanced technology low drag airliner. Master’s thesis, Cranfield University, 2018.
- [40] Nalianda D. Laskaridis P. Valencia, E. A. and R Singh. Methodology to assess the performance of an aircraft concept with distributed propulsion and

- boundary layer ingestion using a parametric approach. *Proceedings of the Institution of Mechanical Engineers, Part G: Journal of Aerospace Engineering*, 229(4), pp. 682–693, 2015.
- [41] A. K. Kundu. *Aircraft Design*. John Wiley & Sons, Cambridge University Press, first edition, pp. 338-342 edition, 2010.
- [42] S. A. Gorton L. R. Owens, B. G. Allan. Boundary layer ingesting inlet flow control. *44th AIAA Aerospace Science Meeting and Exhibit, Journal of Aircraft*, Vol. 45, No. 4, 2006.
- [43] E. L. Goldsmith. Subsonic air intake. 1988.
- [44] A. C. Rabe. Effectiveness of a serpentine inlet duct flow control scheme at design and off-design simulated flight conditions, dissertation. Master’s thesis, Virginia Polytechnic Institute and State University, 2003.
- [45] J. Seddon and E. L. Goldsmith. *Intake Aerodynamics*. Collins Professional and Technical Books, second edition edition, 1985.
- [46] ANSYS FLUENT 12.0 User’s guide.
- [47] J. A. Teixeira. Computational fluid dynamics. Master’s thesis, Cranfield University, 2015.
- [48] E. N. Tinoco M. Mani O. P. Brodersen B. Einfeld R. A. Wahls J. H. Morrison T. Ziskuhr D. Levy M. Murayama D. Mavriplis, J. C. Vassberg. Grid quality and resolution issues from the drag prediction workshop series. *46th AIAA Aerospace Sciences Meeting and Exhibit, AIAA 2008-930*, 2008.
- [49] <https://ntrs.nasa.gov/search.jsp?R=19970010380>.
- [50] <https://ntrs.nasa.gov/archive/nasa/casi.ntrs.nasa.gov/19880012661.pdf>.
- [51] Nils Budziszewski and Jens Friedrichs. Modelling of a boundary layer ingesting propulsor.